

Signal Detection for Overloaded Receivers

Michael Krause

A thesis presented for the degree of
Doctor of Philosophy
in
Electrical and Computer Engineering
at the
University of Canterbury,
Christchurch, New Zealand.

2 October 2009

ABSTRACT

Michael Krause, *Signal Detection for Overloaded Receivers*, 2009

In this work wireless communication systems with multiple co-channel signals present at the receiver are considered. One of the major challenges in the development of such systems is the computational complexity required for the detection of the transmitted signals. This thesis addresses this problem and develops reduced complexity algorithms for the detection of multiple co-channel signals in receivers with multiple antennas. The signals are transmitted from either a single user employing multiple transmit antennas, from multiple users or in the most general case by a mixture of the two. The receiver is assumed to be overloaded in that the number of transmitted signals exceeds the number of receive antennas. Joint Maximum Likelihood (JML) is the optimum detection algorithm which has exponential complexity in the number of signals. As a result, detection of the signals of interest at the receiver is challenging and infeasible in most practical systems.

The thesis presents a framework for the detection of multiple co-channel signals in overloaded receivers. It proposes receiver structures and two list-based signal detection algorithms that allow for complexity reduction compared to the optimum detector while being able to maintain near optimum performance. Complexity savings are achieved by first employing a linear preprocessor at the receiver to reduce the effect of Co-Channel Interference (CCI) and second, by using a detection algorithm that searches only over a subspace of the transmitted symbols. Both algorithms use iterative processing to extract ordered lists of the most likely transmit symbols. Soft information can be obtained from the detector output list and can then be used by error control decoders.

The first algorithm named Parallel Detection with Interference Estimation (PD-IE) considers the Additive White Gaussian Noise (AWGN) channel. It relies on a spatially reduced search over subsets of the transmitted symbols in combination with CCI estimation. Computational complexity under overload is lower than that of JML. Performance results show that PD-IE achieves near optimum performance in receivers with Uniform Circular Array (UCA) and Uniform Linear Array (ULA) antenna geometries.

The second algorithm is referred to as List Group Search (LGS) detection. It is applied to overloaded receivers that operate in frequency-flat multipath fading channels. The LGS detection algorithm forms multiple groups of the transmitted symbols over which an exhaustive search is performed. Simulation results show that LGS detection provides good complexity-performance tradeoffs under overload.

A union bound for group-wise and list-based group-wise symbol detectors is also derived. It provides an approximation to the error performance of such detectors without the need for simulation. Moreover, the bound can be used to determine some detection parameters and tradeoffs. Results show that the bound is tight in the high Signal to Interference and Noise Ratio (SINR) region.

Keywords: Multiuser detection, joint maximum likelihood, list detection, antenna arrays, AWGN channel, Rayleigh fading channel

Michael Krause, Communications Research Group, Department of Electrical and Computer Engineering, University of Canterbury, Private Bag 4800, Christchurch 8140, New Zealand

© Michael Krause 2009

CONTENTS

Abstract	iii
Contents	v
List of Figures	ix
List of Tables	xv
Acknowledgements	xvii
Abbreviations and Acronyms	xix
Notation and Symbols	xxiii
CHAPTER 1 MULTIPLE SIGNAL COMMUNICATION	1
1.1 Multiple Access	2
1.2 Multiple Antenna Systems	5
1.2.1 Channel Model	6
1.2.2 Antenna Arrays	11
1.2.3 Diversity	13
1.2.4 Diversity Combining	14
1.2.5 Beamforming	16
1.2.6 Signal Detection	17
1.3 Outline and Thesis Contributions	21
CHAPTER 2 SIGNAL DETECTION FUNDAMENTALS	23
2.1 Classification of Detection Techniques	23
2.2 Optimum Detection	24
2.2.1 Joint Maximum A Posteriori Detection	25
2.2.2 Joint Maximum Likelihood Detection	26
2.2.3 Integer Least-Squares Problem	27
2.3 Linear Detectors	28
2.3.1 Zero-Forcing	28
2.3.2 Minimum Mean Square Error	29
2.4 Nonlinear Detectors	30

2.4.1	Successive Interference Cancellation	30
2.4.2	Parallel Interference Cancellation	32
2.4.3	Spatially Reduced Search Joint Detection	32
2.4.4	Iterative Multiuser Detection	37
2.5	Conclusions	40
CHAPTER 3	DETECTOR FOR THE AWGN CHANNEL	45
3.1	System Model and Receiver Structure	46
3.2	Preprocessor	48
3.2.1	Spatial Filtering	49
3.2.2	Diversity Combining	51
3.2.3	Spatial Filtering vs. Diversity Combining	52
3.2.4	Sparsity Pattern	53
3.3	Parallel Detection with Interference Estimation (PD-IE)	58
3.3.1	Branch Ordering	60
3.3.2	Symbol Estimation	61
3.3.3	List Combining	67
3.4	Performance	69
3.4.1	Perfect Channel State Information	70
3.4.2	Imperfect Channel State Information	75
3.5	Complexity	78
3.6	Conclusions	81
CHAPTER 4	DETECTOR FOR THE MULTIPATH FADING CHANNEL	83
4.1	System Model and Receiver Structure	84
4.2	Preprocessor	85
4.2.1	Maximum Ratio Diversity Combining	85
4.2.2	Sparsity Matrix	87
4.3	List Group Search Detection	88
4.3.1	Branch List Estimation	90
4.3.2	Global List Optimizer	92
4.4	Performance	94
4.4.1	Perfect Channel State Information	94
4.4.2	Imperfect Channel State Information	98
4.5	Complexity	99
4.6	Conclusions	101
CHAPTER 5	PERFORMANCE BOUNDS	103
5.1	Joint Maximum Likelihood Bound	103
5.2	Performance Bound for Group-wise Symbol Detectors	108
5.2.1	Mapping and Grouping	108
5.2.2	Bound Equation	109

5.2.3	Extension to List-based Group-wise Symbol Detectors	112
5.2.4	Bound Computation based on Mean SINR and Soft Information	113
5.3	Results	116
5.4	Conclusions	119
CHAPTER 6	CONCLUSIONS AND FUTURE WORK	121
6.1	Conclusions	121
6.2	Future Work	122
6.2.1	Further Optimizations	123
6.2.2	Frequency-Selective Fading Channels	124
6.2.3	Joint Channel Estimation and Symbol Detection	124
6.2.4	Error Control Coding	125
6.2.5	Multiuser MIMO Systems	125
6.2.6	Space-Time Coding	125
6.2.7	Performance Bounds	126
	Bibliography	127

LIST OF FIGURES

1.1	Example of a wireless communication system with multiple transmitters and receive node.	2
1.2	The concept of (a) SISO, (b) SIMO, (c) MISO and (d) MIMO wireless links.	5
1.3	Baseband model of a SISO wireless communication channel.	6
1.4	Examples of constellation mappings for a) BPSK ($\mathcal{C} = 2$), b) QPSK ($\mathcal{C} = 4$) and c) 16-QAM ($\mathcal{C} = 16$).	7
1.5	Configuration of a MIMO channel.	9
1.6	Model of a UCA and ULA with $M = 4$ receive antennas and $D > M$ transmitters.	11
1.7	Block diagram of selection and switched combining methods.	14
1.8	Block diagram of maximum ratio and equal gain combining methods.	15
1.9	Block diagram of receive beamforming.	17
1.10	Example of the array pattern of a receive beamformer in an underloaded receiver.	19
1.11	Example of the array pattern of a receive beamformer in an overloaded receiver.	20
2.1	Overview of signal detection techniques.	24
2.2	Geometrical interpretation of the integer least-squares problem.	27
2.3	Block diagram of successive interference cancellation.	30

2.4	MMSE-SIC single stage.	31
2.5	System model of an overloaded receiver employing Spatially Reduced Search Joint Detection (SRSJD).	33
2.6	(a) Spectral square root $(\mathbf{H}^H \mathbf{H})^{(1/2)}$ of \mathbf{H} and (b) sparsity matrix \mathbf{P} for a $M = 5$ element UCA with $D = 6$ transmit signals have equal energy and are uniformly spaced in AOA. A DEIR threshold of 0.1 is used to distinguish the “ <i>high</i> ” and “ <i>low</i> ” energy elements $h_{du} \in \mathbf{H}$ in \mathbf{P} .	34
2.7	Spatial trellis constructed from the sparsity matrix \mathbf{P} in Fig. 2.6(b) for the detection of BSPK symbols.	35
2.8	Performance/ complexity tradeoff of signal detection algorithms under moderate to severe overload.	42
3.1	Overall block diagram of the proposed reduced complexity receiver.	46
3.2	Receiver structure for the PD-IE detector.	47
3.3	(a) Spectral square root $(\mathbf{H}^H \mathbf{H})^{(1/2)}$ of \mathbf{H} and (b) sparsity matrix \mathbf{P} for a 5-element UCA. The transmitted signals are uniformly spaced in AOA. (c) Spectral square root $(\mathbf{H}^H \mathbf{H})^{(1/2)}$ of \mathbf{H} and (d) sparsity matrix \mathbf{P} for a 5-element ULA. The received signal AOAs are uniform within $\theta_{max} = \pm 60^\circ$. There are $D = 6$ equal energy signals present at the receive antennas. Elements with ‘1’ in \mathbf{P} are obtained by using the SEAIR and SSSER criteria (defined later) with thresholds $T_1 = 2$ and $T_2 = 0.1$, respectively.	50
3.4	Graphical illustration of the (a) SSSER and (b) SEAIR criteria which are computed for the d th row $\mathbf{h}[d] \in \mathbf{H}$.	55
3.5	Spectral square root $(\mathbf{H}^H \mathbf{H})^{(1/2)}$ of \mathbf{H} and corresponding sparsity matrix \mathbf{P} for a $M = 5$ antenna ULA with $D = 6$, $D = 10$ and $D = 12$ transmitters using the SSSER and SEAIR criteria with thresholds $T_1 = 2$ and $T_2 = 0.1$. The impinging signals have equal energy and their AOAs are uniform within $\theta_{max} = \pm 60^\circ$.	57

3.6	Block diagram of the PD-IE symbol detector.	59
3.7	The d th symbol estimator in the PD-IE in Fig. 3.6 using (a) explicit CCI estimation and (b) joint detection.	62
3.8	ITB-DDFSE trellis for explicit CCI estimation in symbol estimator #1 in Fig. 3.7(a). The trellis is shown for the UCA example in Figs. 3.3(a) and 3.3(b) using BPSK signals. It corresponds to matrix row $d = 1$.	64
3.9	SER of the signal with worst performance versus the number of co-channel signals at SNR, $\Gamma = 10dB$ for a $M = 5$ -element UCA using JML, SRSJD and PD-IE algorithms. Iteration parameters for PD-IE are shown in Table 3.4.	71
3.10	SER of the signal with worst performance versus SNR for PD-IE with list sizes $L = D$ and $2D$ using a $M = 5$ -element UCA with (a) $D = 8$, (b) $D = 10$ and (c) $D = 12$ signals. The iteration parameters are set to give comparable complexity for PD-IE with explicit CCI estimation and PD-IE with joint detection as shown in Table 3.4.	73
3.11	SER of the signal with worst performance versus SNR for PD-IE using an $M = 6$ -element ULA with element spacing $B = 3\lambda$. There are $D = 9$ and 12 co-channel signals. The size of the global list \mathcal{S} is $L = 2D$.	75
3.12	SER of the signal with worst performance versus number of co-channel signals at SNR, $\Gamma = 10dB$ with perfect and imperfect CSI. The power correlation coefficient is set to $\eta = 0.98, 0.995$ and 1 (perfect CSI). The receiver setup and detection parameters are the same as in Fig. 3.9.	77
3.13	SER of the signal with worst performance versus the SNR with perfect and imperfect CSI. The power correlation coefficient is set to $\eta = 0.98, 0.995$ and 1 (perfect CSI). The receiver setup and detection parameters are the same as in Fig. 3.9. Results are shown for $D = 6$ and 10 signals.	78
4.1	Receiver structure for the LGS detector.	84

4.2	(a) Example of the energy of the preprocessor output matrix \mathbf{H} , $(\mathbf{H}^H \mathbf{H})^{(1/2)}$, for a receiver with $M = 6$ antennas and $D = 9$ signals in a frequency-flat Rayleigh fading channel, (b) Sparsity matrix \mathbf{P} derived from \mathbf{H} using the selection algorithm of Table 3.1.	88
4.3	Block diagram of the LGS detector.	90
4.4	SER versus the number of co-channel signals for a $M = 4$ antenna receiver at SNR, $\Gamma = 10dB$.	95
4.5	SER versus SNR for a $M = 6$ antenna receiver with (a) $D = 9$ and (b) $D = 12$ co-channel signals.	97
4.6	SER versus number of co-channel signals at SNR, $\Gamma = 10dB$ with perfect and imperfect CSI. The power correlation coefficient is set to $\eta = 0.98$, 0.995 and 1 (perfect CSI).	99
4.7	SER versus the SNR with perfect and imperfect CSI. The power correlation coefficient is set to $\eta = 0.98$, 0.995 and 1 (perfect CSI). Results are shown for $D = 6$ and 8 signals.	100
5.1	Example of mapping the QPSK vector \mathbf{s} with $D = 9$ symbols into the new vector $\dot{\mathbf{s}}$. It contains a permutation of the symbols in \mathbf{s} and is further divided into the group vectors $\dot{\mathbf{s}}_g$ and $\dot{\mathbf{s}}_{\bar{g}}$.	109
5.2	Search space of a group-wise symbol detector.	110
5.3	Search space of a list-based group-wise symbol detector.	112
5.4	Example of a list-based group-wise symbol detector using a list \mathcal{W} with $L = 6$ elements $\hat{\mathbf{s}}_w^{(l)} \in \mathcal{W}$. Each symbol vector $\dot{\mathbf{s}}$ has $D = 9$ symbols and is further split into the two group vectors $\dot{\mathbf{s}}_g$ and $\dot{\mathbf{s}}_{\bar{g}}$. Estimates of $\dot{\mathbf{s}}_{\bar{g}}$ are represented by the list members $\hat{\mathbf{s}}_w^{(l)} \in \mathcal{W}$.	113
5.5	SER of a group-wise symbol detector versus the number of co-channel signals D for a $M = 2$ antenna receiver and various SIR. The SNR is set to $\Gamma = 20dB$. Union bounds are shown by a solid line and simulation by a dashed line.	116

- 5.6 SER versus SNR for an $M = 4$ antenna receiver with $D = 6$ co-channel signals and various SIR values. Solid lines indicate bounds and dashed lines show simulation results. 117
- 5.7 SER of the LGS detector versus SNR for an $M = 4$ antenna receiver with $D = 6$ co-channel signals. Union bounds are shown by a solid line and LGS simulation results by a dashed line. 120

LIST OF TABLES

2.1	Summary of ITB-DDFSE symbol detection	37
2.2	Summary of Iterative Multiuser Detection (IMUD)	39
3.1	Construction of the sparsity matrix \mathbf{P}	56
3.2	Summary of the ITB-DDFSE algorithm of [22]	66
3.3	Iterative list combining algorithm	68
3.4	Iteration parameters and computational complexity for PD-IE simulations in Fig. 3.9 and Fig. 3.10 using an $M = 5$ -element UCA.	71
3.5	Comparison of computational complexity for a receiver with $M = 8$ -element UCA front-end	80
4.1	Iterative group-wise branch list estimation algorithm	92
4.2	Iterative group-wise global list optimization algorithm	94
4.3	Simulation parameters for LGS detection in Fig. 4.4.	95
4.4	Simulation parameters for LGS detection in Fig. 4.5.	96
4.5	Simulation parameters for LGS detection in Figs. 4.6 and 4.7.	98
4.6	Comparison of computational complexity for the $M = 6$ antenna receiver in Fig. 4.5.	101
5.1	Simulation parameters for the group-wise LGS detector in Fig. 5.7.	118
5.2	Simulation parameters for the list-based group-wise LGS detector in Fig. 5.7.	118

5.3	Measured SINR values of the group-wise LGS detector of Table 5.1 (list size $L = 1$) and the list-based group-wise LGS detector of Table 5.2 (list sizes $L = 24$ and $L = 64$).	119
-----	--	-----

*It is through science that we prove,
but through intuition that we discover.*

- Henri Poincare

ACKNOWLEDGEMENTS

I wish to express my gratitude to everyone who has contributed to this thesis.

I owe special thanks to Professor Desmond P. Taylor and Dr. Philippa A. Martin for supervising my research and their encouragement and valuable discussions over the time this thesis was produced.

I am very grateful to Dr. Peter Green for his continuous support, patience and the many helpful coffee and lunch breaks.

I would like to thank Gayathri Kongara for the many fruitful discussions and the graduate students of the Communications Research Group for their help in my daily work.

Very special thanks go to my family in Germany and to my partner Magda for their encouragement and support during the long days of work. I wish to further thank Ann, Laura and Simon Green for the time they shared with me.

Finally, I am grateful to the University of Canterbury and the Department of Electrical and Computer Engineering for funding my studies through their doctoral and departmental scholarships.

ACRONYMS

3G	Third Generation
4G	Fourth Generation
AOA	Angle of Arrival
AWGN	Additive White Gaussian Noise
APP	A Posteriori Probability
BER	Bit Error Rate
BLE	Branch List Estimator
BPSK	Binary Phase Shift Keying
CCI	Co-Channel Interference
CDMA	Code Division Multiple Access
CSI	Channel State Information
DDFSE	Delayed Decision Feedback Sequence Estimation
DEIR	Desired Energy to Interference Ratio
EGC	Equal Gain Combining
FDMA	Frequency Division Multiple Access
FIR	Finite Impulse Response

ACRONYMS

GLO	Global List Optimizer
GSM	Global System for Mobile Communication
i.i.d.	independent and identically distributed
IMUD	Iterative Multiuser Detection
ISI	Inter-Symbol Interference
ITB-DDFSE	Iterative Tail Biting-Delayed Decision Feedback Sequence Estimation
JMAP	Joint Maximum A Posteriori
JML	Joint Maximum Likelihood
LGS	List Group Search
LLR	Log-Likelihood Ratio
LOS	Line-Of-Sight
MAP	Maximum A Posteriori
MGF	Moment Generating Function
MIMO	Multiple-Input Multiple-Output
MISO	Multiple-Input Single-Output
ML	Maximum Likelihood
MMSE	Minimum Mean Square Error
MRC	Maximal Ratio Combining
pdf	probability density function
PD-IE	Parallel Detection with Interference Estimation
PEP	Pairwise Error Probability

PIC	Parallel Interference Cancellation
QAM	Quadrature Amplitude Modulation
QPSK	Quadrature Phase Shift Keying
RSS	Received Signal Strength
SDMA	Space Division Multiple Access
SEAIR	Signal Energy to Average Interference Ratio
SER	Symbol Error Rate
SEIR	Strongest Energy to Interference Ratio
SIC	Successive Interference Cancellation
SIMO	Single-Input Multiple-Output
SINR	Signal to Interference and Noise Ratio
SIR	Signal to Interference Ratio
SISO	Single-Input Single-Output
SNR	Signal to Noise Ratio
SRSJD	Spatially Reduced Search Joint Detection
SSSER	Signal to Strongest Signal Energy Ratio
TDMA	Time Division Multiple Access
UCA	Uniform Circular Array
ULA	Uniform Linear Array
VA	Viterbi Algorithm
WLAN	Wireless Local Area Network

ACRONYMS

WPAN Wireless Personal Area Network

ZF Zero Forcing

NOTATION AND SYMBOLS

Scalar variables in this thesis are written as plain letters, vectors as bold face lower-case letters, matrices as bold face upper-case letters and lists as upper-case calligraphic letters. Further symbols and notations used include the following:

$\mathbf{A}, \mathbf{A}_{(m \times n)}$	The matrix \mathbf{A} with dimension $m \times n$.
$a_{ij}, \mathbf{a}[i], \mathbf{a}(j)$	The ij -th element, the i -th row and the j -th column vector of the matrix \mathbf{A} , respectively.
$\hat{a}, \hat{\mathbf{a}}, \hat{\mathbf{A}}$	The estimate of the scalar a , the vector \mathbf{a} and the matrix \mathbf{A} , respectively.
$\mathbf{A}^H, \mathbf{A}^T$	Complex conjugate (Hermitian transpose) and transpose of \mathbf{A} .
$x_i, x[i]$	The i th element of a vector \mathbf{x} .
\mathbf{I}	The identity matrix and \mathbf{I}_m for the $m \times m$ identity matrix.
$\mathbf{0}$	The zero vector and the zero matrix.
$\dot{\mathbf{x}}$	Permutation of a vector \mathbf{x} .
$\ \mathbf{x}\ $	L2-norm of a vector \mathbf{x} .
$\min_{\mathcal{S}} (V(\mathcal{S}))$	The minimum value of the function $V(\cdot)$ in the set \mathcal{S} .
$\arg \min_{\mathcal{S}} (V(\mathcal{S}))$	The minimizing argument of the function $V(\cdot)$ over the set \mathcal{S} .

NOTATION AND SYMBOLS

The following is the list of commonly used symbols:

\mathcal{A}	Symbol alphabet
\mathbf{A}	Response matrix of an antenna array
D	Number of transmitted signals
d	Signal index (also detector branch index), $1 \leq d \leq D$
E_s	Received signal energy
$f(D, M)$	Receiver load factor
\mathbf{H}	Channel matrix (also channel gain matrix)
L	List size
M	Number of antennas at receive array
\mathbf{m}	Antenna element index, $1 \leq m \leq M$
N_0	Noise power spectral density
\mathbf{n}	Noise vector
\mathbf{x}	Received signal vector
\mathcal{S}	Symbol (sub-)space, e.g. a list of L symbol vectors
\mathbf{s}	Transmitted symbol vector
U_e	Enumeration set
Γ	Signal to Noise Ratio (SNR)
Ψ	Signal to Interference and Noise Ratio (SINR)
λ	Signal wave length
Φ_{nn}	Autocorrelation of the noise
σ_n^2	Variance of \mathbf{n}

Chapter 1

MULTIPLE SIGNAL COMMUNICATION

WIRELESS communication systems are under constant pressure to increase capacity and spectral efficiency while ensuring reliability of data transfer. Technological progress and new wireless communication standards have created many new applications. Commercially available systems range from global coverage low bit rate satellite systems over medium bit rate continental cellular networks with mobile users to high bit rate personal and local area networks with only a few meters range. Dozens of different communication standards have evolved. Some examples are the Global System for Mobile Communication (GSM), Third Generation (3G) and Fourth Generation (4G) cellular telecommunication systems, Wireless Local Area Network (WLAN) and Wireless Personal Area Network (WPAN) standards such as Bluetooth and Zigbee. The coexistence of different systems results in a crowded frequency spectrum where many users are required to share limited frequency resources. Spectral efficiency is therefore of extreme importance.

Research has indicated that significant increases in spectral efficiency and reliability of wireless data transfer can be achieved by using multiple antennas. One of the major challenges of such systems is the detection of multiple co-channel signals impinging on a receive antenna array. Co-channel signals are signals sharing the same frequency, time and space. The main theme of this thesis is the efficient detection of multiple co-channel signals in an overloaded receiver. A receiver is said to be overloaded if the number of signals exceeds the number of receive antennas. Under overload, the signal detection problem becomes very challenging because the complexity of optimum

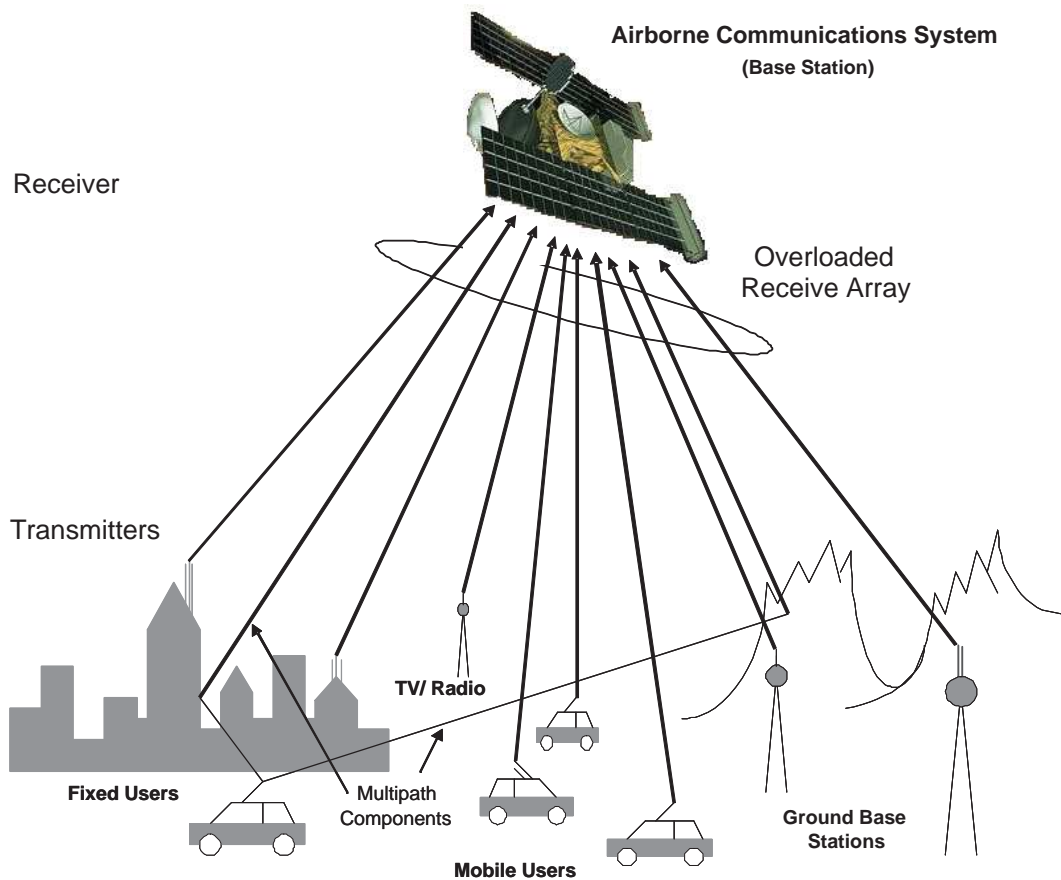


Figure 1.1 Example of a wireless communication system with multiple transmitters and receive node.

detectors prohibits their use in most practical systems and lower complexity linear detectors perform very poorly.

Before outlining the main theme of this thesis and its contributions in more detail the basic concepts of multiple signal and multiple antenna communication systems are introduced.

1.1 MULTIPLE ACCESS

Most communication systems have several transmit and/ or receive nodes. In practical systems these communication nodes are often referred to as either user or base station nodes. Fig. 1.1 shows an example of a communication system with multiple transmit and receive nodes. The capacity and spectral efficiency of such systems can be sig-

nificantly improved by using multiple access techniques. Multiple access refers to the simultaneous transmission by numerous transmitters sharing the same scarce resource, i.e. the base station. The sharing can take place in four domains:

Frequency: In Frequency Division Multiple Access (FDMA) the frequency spectrum is divided into different segments and each transmitter is assigned a unique segment to effectively avoid CCI.

Time: The Time Division Multiple Access (TDMA) technique allows each transmitter to use the entire transmission resource for a brief period of time. To avoid simultaneous transmission each transmitter is allocated a specified time slot in each successive frame. Again, this tends to avoid CCI.

Code: In Code Division Multiple Access (CDMA) the transmit signals are modulated using spread spectrum modulation (i.e. modulation over a wide frequency range). Each transmit signal is modulated with a unique code that identifies the sender. The receiver uses the appropriate code to detect the transmitted signals. CDMA exhibits CCI due to simultaneous transmission in the same frequency range.

Space: Space Division Multiple Access (SDMA) is a widely used multiple access technique. A simple form of SDMA divides the geographical area into different cells. The same carrier frequency can then be reused in different cells as long as the spatial distance between the cells is sufficient to reduce the amount of CCI. More sophisticated forms of SDMA make use of adaptive antenna arrays. Even though significant amounts of CCI may be present, such systems are able to provide service to many independent transmitters within the same cell.

Currently, significant research effort is being concentrated on increasing capacity and spectral efficiency through the use of SDMA techniques. To this end, advanced signal processing strategies are used at both the transmitter and receiver. It is well known that the use of an antenna array at one or both ends of a wireless link can improve the performance of the wireless connection. The main arguments for the use

of antenna arrays are:

Antenna array gain: Multiple antennas offer increased antenna gain and therefore provide better coverage and range than a single antenna. This is due to the antenna array's ability to focus the transmit and/ or received energy.

Antenna diversity: This is also known as *space diversity*. Antenna diversity can be employed on the transmit, receive or both ends of a wireless link. At the receiver, multiple antennas collect correlated or uncorrelated replicas of the transmitted signals providing redundancy in the spatial domain. The replicas are combined using signal processing to increase the overall Signal to Noise Ratio (SNR) and to mitigate the effects of multipath fading. The probability that all signals are in a deep fade simultaneously is small which increases the robustness of the wireless link. Antenna diversity at the transmitter allows the transmitted data to be split and then spread across multiple antennas. The multiple antennas must be spaced at sufficient distance to minimize correlation. In practice, this is achieved if the spacing significantly exceeds $1/2$ of the carrier frequency wave length. An important aspect of antenna diversity is that it does not induce any loss in bandwidth efficiency.

Interference mitigation: Signal processing applied to the multiple receive antennas can create adaptive beam patterns that make the system less susceptible to interference and increase the system capacity. In contrast to antenna diversity, in this case the antennas are required to be closely spaced, usually at less than $1/2$ the wave length of the carrier frequency.

The primary focus of this thesis is on designing advanced signal processing algorithms for a receiver node employing an antenna array. A typical example is the uplink mode of a cellular telecommunication system where the transmit nodes are individual users and the receive node is a base station with an antenna array. In a sophisticated system, each user may also employ multiple antennas. This means that multiple signal streams can originate from the same transmit node. To keep the description general,

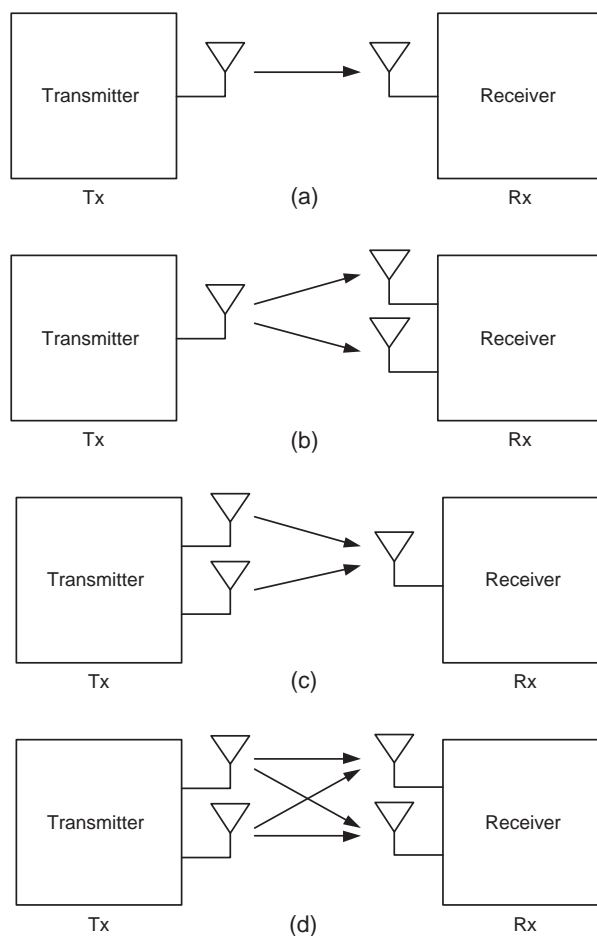


Figure 1.2 The concept of (a) SISO, (b) SIMO, (c) MISO and (d) MIMO wireless links.

the thesis refers to multiple signals rather than multiple user communication. The multiuser scenario is included.

1.2 MULTIPLE ANTENNA SYSTEMS

Wireless links between a transmit and receive node are often characterized by the number of inputs and outputs. The different types of links are referred to as either Single-Input Single-Output (SISO), Multiple-Input Single-Output (MISO), Single-Input Multiple-Output (SIMO) or Multiple-Input Multiple-Output (MIMO) links. Fig. 1.2 provides an overview. The SISO link is the simplest configuration requiring only one transmit and one receive antenna. All other types have multiple channel inputs and/ or outputs which can be achieved by either multiple antennas, polarization or

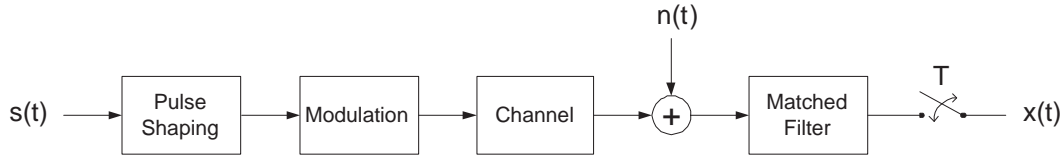


Figure 1.3 Baseband model of a SISO wireless communication channel.

antenna modes.

1.2.1 Channel Model

Wireless channel models describe the propagation of signals from the transmitter to the receiver. In order to find the electromagnetic field impinging on a receive antenna one must solve the electromagnetic field equations governing the channel in conjunction with the transmitted signal. This is impractical as it requires taking into account all obstructions in the propagation path that affect the electromagnetic field at the receiver, i.e. buildings, cars etc. Instead, the channel is often simplified and modelled by a stochastic process. This assumes that different channel behaviors appear with different probabilities, and that they change over time (with specific statistical properties).

SISO channel

Fig. 1.3 depicts the baseband model of a wireless SISO channel. The channel inputs, the output and the channel itself are *time variant* as indicated by the time index t . The symbols $s(t)$ represent the transmitted baseband data. It is first *pulse shaped*, for example using a raised cosine pulse shape. The resulting signal is then modulated onto a carrier signal with frequency f_c . Depending on the modulation type the transmit symbols $s(t)$ are either real (e.g. Binary Phase Shift Keying (BPSK)) or complex (e.g. Quadrature Phase Shift Keying (QPSK) or Quadrature Amplitude Modulation (QAM)) valued. Symbol values for $s(t)$ are drawn from an alphabet \mathcal{A} . For example $\mathcal{A} = \{-1, 1\}$ for BPSK and $\mathcal{A} = \{(-1, -1), (-1, 1), (1, -1), (1, 1)\}$ for QPSK. Fig. 1.4 depicts examples of different constellation mappings. The *constellation size*¹ \mathcal{C} is given

¹The constellation size is often referred to as alphabet size.

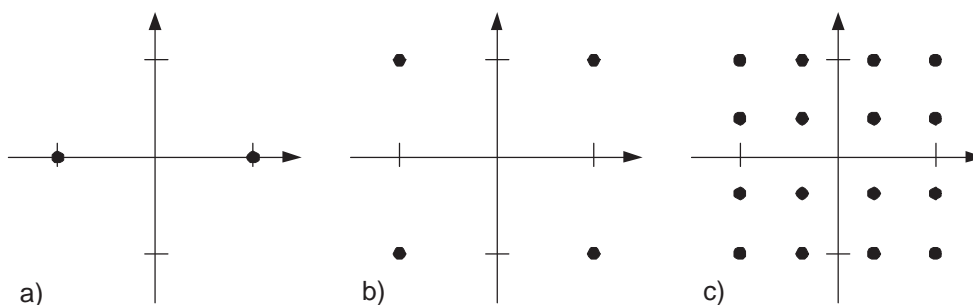


Figure 1.4 Examples of constellation mappings for a) BPSK ($\mathcal{C} = 2$), b) QPSK ($\mathcal{C} = 4$) and c) 16-QAM ($\mathcal{C} = 16$).

by

$$\mathcal{C} = |\mathcal{A}|. \quad (1.1)$$

The modulated signal is propagated through the channel to the receiver. The wave length $\lambda(f_c)$ of electromagnetic radiation at a given carrier frequency f_c is

$$\lambda(f_c) = \frac{c}{f_c}, \quad (1.2)$$

where $c = 3 \times 10^8$ m/s is the velocity of light in a vacuum. At the receiver, thermal noise² is represented by the term $n(t)$ which is added prior to the matched filtering and sampling stages. The matched filtering is usually with respect to the transmitted pulse shape and the signal is sampled with symbol period T . The resulting received signal is denoted $x(t)$. The baseband received signal for a frequency non-selective fading³ SISO link is given by

$$x(t) = h(t)s(t) + n(t), \quad (1.3)$$

where $h(t)$ represents the channel response. The channel coefficient $h(t)$ and the received signal $x(t)$ are typically complex valued variables with in-phase (real) and quadrature (imaginary) components.

If the channel includes *multipath propagation* the signal is spread in time and spatial dimensions meaning the signal arrives from different directions and with different

²Although noise is added at several stages in the transmit/ receive process the noise term $n(t)$ is modelled by adding it prior to the filtering and sampling stages of the receiver. It represents thermal and other noises.

³This is also known as frequency-flat fading.

time delays. This results in the phenomenon known as *Inter-Symbol Interference (ISI)*. Assuming a channel impulse response $h(t)$ longer than the symbol period T , the transmit symbols pass through the wireless channel which is usually modelled as an Finite Impulse Response (FIR) filter. The received signal for the SISO link in Fig. 1.2 then becomes

$$x(t) = \sum_k h(t - kT)s_k + n(t), \quad (1.4)$$

where $(t - kT)$ describes the discrete time delay and s_k is the symbol transmitted at time kT . For simplicity, this thesis only considers symbol-synchronous signals⁴ with no ISI present at the receiver as described by (1.3). This is referred to as the frequency-flat fading case. Although frequency-selective fading is not within the scope of this thesis, the extension can be done at the cost of additional complexity (e.g. by applying the Viterbi algorithm in the time domain or by using other channel equalization structures).

SIMO channel

If a wireless communication system has one transmitter and M antennas at the receiver (SIMO link) then the transmit signal impinges on each antenna and the received signal $x(t)$ becomes the column vector $\mathbf{x}(t) \in \mathbb{C}^M$ with $\mathbf{x}(t) = [x_1(t) \ x_2(t) \ \dots \ x_M(t)]^T$. The received signal is then modelled as

$$\mathbf{x}(t) = \mathbf{h}(t)s(t) + \mathbf{n}(t) \quad (1.5)$$

where the complex channel and noise vectors $\mathbf{h}(t) \in \mathbb{C}^M$ and $\mathbf{n}(t) \in \mathbb{C}^M$ are denoted $\mathbf{h}(t) = [h_1(t) \ h_2(t) \ \dots \ h_M(t)]^T$ and $\mathbf{n}(t) = [n_1(t) \ n_2(t) \ \dots \ n_M(t)]^T$, respectively.

MISO channel

Similarly, for the MISO case with D transmitters and a single receive antenna, (1.3) becomes

$$x(t) = \mathbf{h}(t)\mathbf{s}(t) + n(t) \quad (1.6)$$

⁴The extension to the non-synchronous signal case requires a synchronization process.

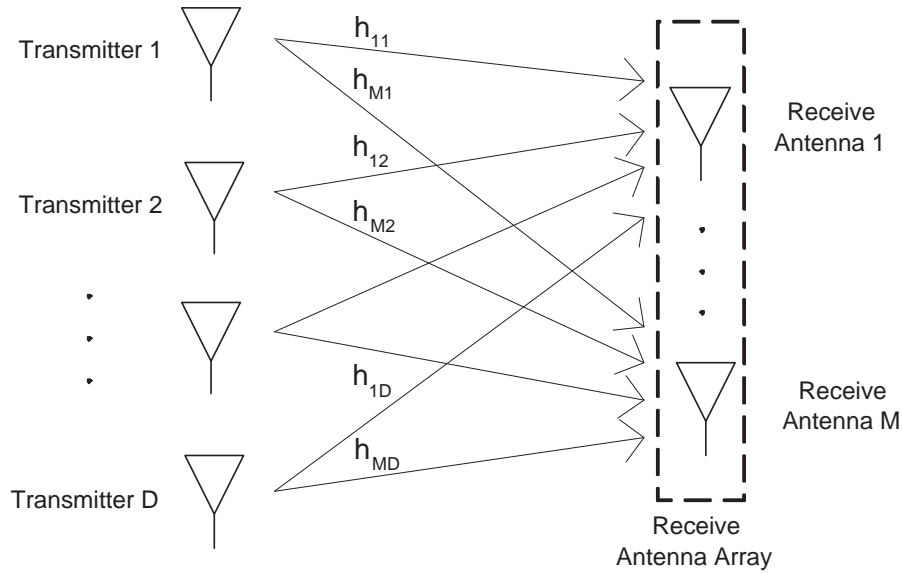


Figure 1.5 Configuration of a MIMO channel.

where $\mathbf{h}(t) \in \mathbb{C}^D$ denotes the channel vector $\mathbf{h}(t) = [h_1(t) \ h_2(t) \ \dots \ h_D(t)]$ and $\mathbf{s}(t) \in \mathcal{A}^D$ is the symbol vector with $\mathbf{s}(t) = [s_1(t) \ s_2(t) \ \dots \ s_D(t)]^T$. Values for $\mathbf{s}(t)$ are drawn from a D -dimensional alphabet \mathcal{A}^D .

MIMO channel

The MIMO link is the most general case because it includes SISO, SIMO and MISO channels as special cases. Fig. 1.5 shows a typical MIMO configuration. The system has a total of D transmitters and M receive antennas. The channel is defined by the

$$\text{matrix } \mathbf{H}(t) \in \mathbb{C}^{M \times D}, \text{ which is written as } \mathbf{H}(t) = \begin{bmatrix} h_{11}(t) & h_{12}(t) & \dots & h_{1D}(t) \\ h_{21}(t) & h_{22}(t) & \dots & h_{2D}(t) \\ \vdots & \vdots & \ddots & \vdots \\ h_{M1}(t) & h_{M2}(t) & \dots & h_{MD}(t) \end{bmatrix}.$$

The matrix element $h_{md}(t) \in \mathbf{H}(t)$ describes signal propagation from the d th transmitter to the m th receive antenna. This is often referred to as the *channel gain*. The D transmit symbols $\mathbf{s}(t) \in \mathcal{A}^D$ are given as the vector $\mathbf{s}(t) = [s_1(t) \ s_2(t) \ \dots \ s_D(t)]^T$. The received signals and the noise at the M -antenna receive array are described by the column vectors $\mathbf{x}(t) \in \mathbb{C}^M$ and $\mathbf{n}(t) \in \mathbb{C}^M$, respectively. These are denoted

$\mathbf{x}(t) = [x_1(t) \ x_2(t) \ \dots \ x_M(t)]^T$ and $\mathbf{n}(t) = [n_1(t) \ n_2(t) \ \dots \ n_M(t)]^T$. The received signal vector for the flat non-dispersive fading MIMO channel is then given by

$$\mathbf{x}(t) = \mathbf{H}(t)\mathbf{s}(t) + \mathbf{n}(t). \quad (1.7)$$

The term MIMO often refers to a wireless link where a single transmit node produces multiple channel inputs and sends data to a receiver with multiple channel outputs. On the other hand, the transmitters in Fig. 1.5 can also be seen as individual users with one or more antennas. If the receiver has an antenna array, each user then transmits data through either a SIMO or MIMO link. Thus both the single user MIMO and the multiple user SIMO/ MIMO scenarios are described by the channel model in (1.7).

Signal detection in a communication system with multiple users is referred to as *multiuser detection*. The main differences between a single user MIMO system and a multiple user system are

- the spatial separation between the transmit antennas,
- the power constraints on the system and
- whether a single or multiple users transmit⁵ data.

When designing a single user MIMO system, the assumption is often made that the transmit antennas are separated by several wave lengths to avoid antenna correlation. A special coding technique known as *space-time coding*⁶ is often used. The overall transmit power of a single user MIMO system is usually assumed to be fixed. As a result, increasing the number of transmit antennas reduces the transmit power of each individual antenna so that the sum remains constant.

In contrast, in a multiple user system, two or more transmit nodes⁷ can either

⁵This would impact the space-time and error control coding, which are not the main focus of this work. As a result, coding differences between single and multiple users are not considered in this thesis.

⁶Space-time coding introduces joint correlation in both space and time domains to improve the capacity and spectral efficiency.

⁷These include multiple antenna transmitters as in a multiuser MIMO system.

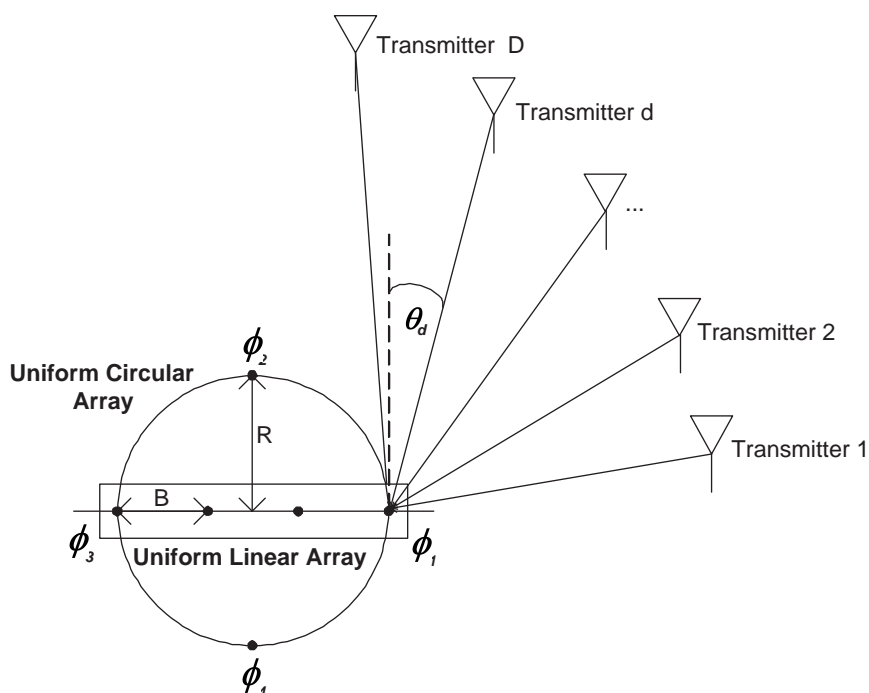


Figure 1.6 Model of a UCA and ULA with $M = 4$ receive antennas and $D > M$ transmitters.

be closely spaced (i.e. two or more users share the same spatial location) or spread widely from each other (e.g. the users are located in quite different directions from the receiver). The first introduces correlation whereas the latter can benefit from SDMA techniques such as *receive beamforming* and *diversity combining*. The overall transmit power of a multiple user system normally increases with the addition of more users.

The focus of this thesis is on the detection of multiple co-channel signals at the receiver. Note that the term *multiple signals*⁸ is used to keep the description general.

1.2.2 Antenna Arrays

If the transmission includes Line-Of-Sight (LOS) links between the transmit and receive antennas the physical properties of the antenna array at the receiver must be incorporated into the channel model in (1.7). Fig. 1.6 shows the special case of multiple signals transmitted via LOS links and impinging on a receiver with multiple antennas arranged in UCA and ULA geometries. This channel is known as the AWGN channel

⁸The multiple signals can be from a single user employing several transmit antennas (single user MIMO) or from multiple users.

and the received signal vector $\mathbf{x}(t) \in \mathbb{C}^M$ is given by

$$\mathbf{x}(t) = \mathbf{A}\mathbf{s}(t) + \mathbf{n}(t), \quad (1.8)$$

where $\mathbf{A} \in \mathbb{C}^{M \times D}$ is the composite array response matrix. If \mathbf{A} is written in column vector notation, $\mathbf{A} = [\mathbf{a}(1) \mathbf{a}(2) \dots \mathbf{a}(D)]$, the vector $\mathbf{a}(d) \in \mathbb{C}^M$ is then the array steering vector for the d th signal.

Uniform Circular Array

The UCA has isotropic antenna elements equi-spaced on a circle with radius R as shown in Fig. 1.6. Following [1], the array steering vector for each of the D signals is denoted $\mathbf{a}(d) = [a_1 \ a_2 \ \dots \ a_M]^T$ with components given by

$$a_m = \exp\left(-j\frac{2\pi R}{\lambda} \cos\left(\frac{\pi}{2} - \theta_d - \phi_m\right) \sin \epsilon_d\right), \quad d = 1, 2, \dots, D \quad (1.9)$$

where

$$\begin{aligned} \theta_d & \quad \text{azimuthal angle of arrival (AOA) from the } d\text{th transmitter} \\ \epsilon_d & \quad \text{elevation (or depression) angle} \\ \lambda & \quad \text{wavelength at the carrier frequency} \\ \phi_m & = \frac{2\pi(m-1)}{M}, \text{ angle of the } m\text{th element in azimuth [2].} \end{aligned}$$

For simplicity⁹, often only azimuth is considered ($\epsilon_d = 90^\circ$). However, the results can easily be extended to three dimensions.

Uniform Linear Array

In the ULA configuration, isotropic antenna elements are located in a straight line with equal spacing B between the elements [4]. This is illustrated in Fig. 1.6. The

⁹The assumption is made in this case that the antenna elements have high elevation so that $\sin(\epsilon_d) \approx 1$. In practice, this requires a high altitude receiver as described in [3].

array steering vector for each signal is again denoted $\mathbf{a}(d) = [a_1 \ a_2 \ \dots \ a_M]^T$, but with components given by [1]

$$a_m = \exp\left(-j\frac{2\pi B(m-1)}{\lambda} \sin\theta_d\right), \quad d = 1, 2, \dots, D. \quad (1.10)$$

1.2.3 Diversity

Diversity techniques are often used to improve the reliability of transmission by reducing the effects of multipath fading [5, 6]. Diversity requires replicas of the transmitted signal at the receiver with little or no correlation of the fading statistics of the channels between the transmitter and the receiver. Then, the probability of the received strengths of all signals being below a given threshold is much lower than the probability of any individual signal strength being below that level. The following are the most common diversity domains:

Time: In time diversity, the same information is transmitted in different time slots.

Time diversity results in decoding delays and causes a loss in bandwidth efficiency.

It is often used in fast fading environments [7].

Frequency: When using frequency diversity, different frequencies are used to transmit the same information. It is effective when the coherence bandwidth of the channel is small. The drawback is the loss in bandwidth efficiency [7].

Space: Depending on where the diversity is employed, space diversity is called transmit or receive diversity. In the case of transmit diversity, several antennas transmit the same signal through channels with either no or only few correlation. In receive diversity, multiple antennas receive the transmitted signals and combine them into a single signal. The advantage of space diversity is that diversity is achieved without any loss in bandwidth efficiency.

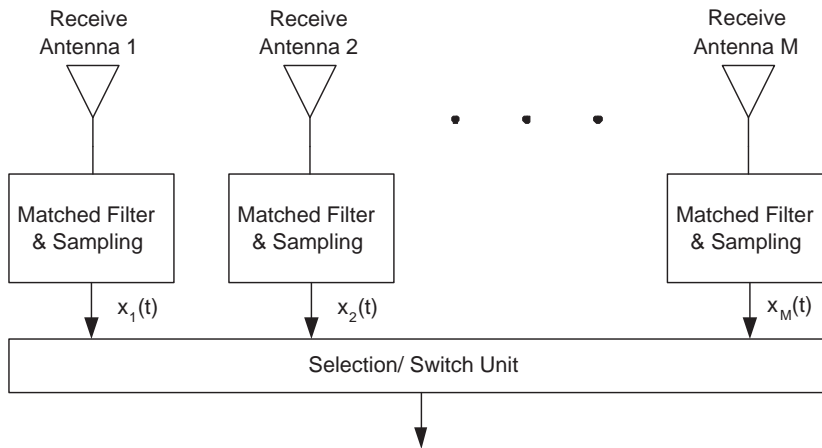


Figure 1.7 Block diagram of selection and switched combining methods.

1.2.4 Diversity Combining

The performance of a communication system in a fading environment depends on how multiple replicas of the same information are combined at the receiver, in order to mitigate deep fades. This is known as *diversity combining*.

Selection Combining

Selection combining is a very simple combining method. A logic selector simply selects the signal with the largest SNR as the output signal. The drawback is that the SNR at all receive antennas needs to be measured continuously. In practice, the Received Signal Strength (RSS) is often used as a measurement.

Switched Combining

Switched combining scans all diversity branches and selects a branch with its SNR above a certain threshold. If the SNR drops below the threshold the receiver starts scanning again. This yields lower complexity than selection combining but the performance is worse. The RSS is often used instead of the SNR. Fig. 1.7 is an illustrative block diagram of selection and switched combining.

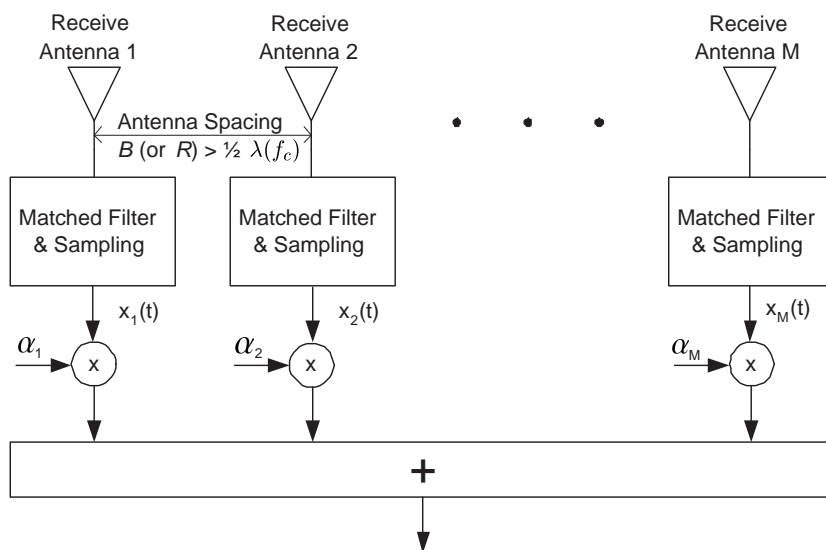


Figure 1.8 Block diagram of maximum ratio and equal gain combining methods.

Maximum Ratio Combining

Maximal Ratio Combining (MRC) is a linear combining method in which all received signals are individually weighted and added to get an output signal. Fig. 1.8 shows a block diagram. The weighting factor α_m for each antenna is chosen to be proportional to its signal amplitude to noise variance ratio. Specifically, α_m is given by

$$\alpha_m = X_m e^{-j\varphi_m} \quad (1.11)$$

where X_m is the received amplitude and φ_m is the phase of the m th received signal $x_m(t)$. MRC is also referred to as optimum combining because it maximizes the output SNR. For best performance, the multiple replicas of the transmitted signals should be uncorrelated. This requires sufficient antenna spacing which, in practice, is achieved for spacings that significantly exceed $1/2$ the carrier frequency wave length $\lambda(f_c)$.

Equal Gain Combining

Equal Gain Combining (EGC) is suboptimum but has lower complexity than MRC. The reason is that EGC does not require an estimate of the signal amplitude X_m so that the weighting factor is chosen as

$$\alpha_m = e^{-j\varphi_m}. \quad (1.12)$$

MRC and EGC require information about the channel which is known as *Channel State Information (CSI)*. Although unrealistic, the assumption of perfect CSI provides a lower performance bound on the achievable error rate. Perfect CSI requires a *genie* that provides the receiver with the correct channel estimates. The more realistic case of imperfect CSI requires a *channel estimation* process¹⁰ that provides the receiver with estimates of the channel matrix.

More sophisticated diversity combining approaches often use an adaptive combination of the previously described fundamental methods. These are referred to as hybrid combining and can provide a better complexity/ performance tradeoff. A comprehensive overview of diversity combining including a performance analysis of the combining approaches in different channel environments is given in [9].

1.2.5 Beamforming

Beamforming is another SDMA technique that can be employed on either transmit, receive or on both ends of a wireless link. Unlike diversity combining, beamforming techniques work best if the multiple replicas of the transmitted signals are sufficiently correlated. This requires closely spaced receive antennas which is achieved for spacings that are less than 1/2 of the carrier frequency wave length $\lambda(f_c)$.

Fig. 1.9 shows the block diagram of an antenna array with beamformer. If used as a receive beamformer, the signal samples x_m are multiplied by their corresponding weights w_m and added. This is similar to the diversity combiner in Fig. 1.8 but requires different weights to exploit the spatial antenna correlation. Note that beamforming requires CSI to obtain optimum weights. More sophisticated beamformers employ adaptive weights to best mitigate CCI and to maximize the resulting SNR.

¹⁰See e.g. [8] for more information on channel estimation.

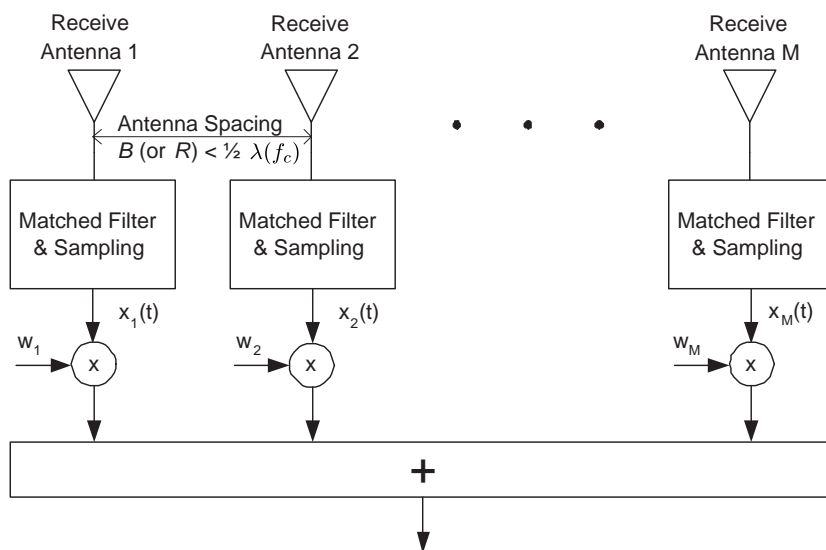


Figure 1.9 Block diagram of receive beamforming.

1.2.6 Signal Detection

Every receiver faces the problem of detecting the signal(s) of interest from the received signal(s). This is known as the *signal detection* problem. A simple definition is given as follows: Signal detection is the ability to discern between signal(s) and noise at the receiver end and to recover the transmitted information from the received waveform.

Observing the noise spectrum and applying a threshold is a simple approach to distinguish between a signal and noise. This implies that in order to detect the correct transmitted symbols with high probability, the received signal energy E_s per symbol must be greater than the noise power spectral density N_0 . The SNR, denoted as Γ , is an important parameter in determining the performance of a signal detector. It is defined here as

$$\Gamma = \frac{E_s}{N_0} = \frac{\sigma_s^2}{\sigma_n^2}, \quad (1.13)$$

where σ_s^2 and σ_n^2 denote the received signal and noise variances¹¹, respectively.

If multiple signals are present at a receive antenna as in multiple access communications, signal detection becomes more difficult because the detector needs to cope with

¹¹A random variable's power equals its mean-squared value. If this variable has zero mean its power is equal to its variance.

both noise and interference. This applies in particular to space-time systems where multiple co-channel signals share the same frequency, time and space. Ideally, a good signal detector is able to detect all co-channel signals.

The use of an antenna array at the receiver plays an important role in the detection of multiple co-channel signals because SDMA techniques such as diversity combining and beamforming can be utilized. Performance of a signal detector is determined by the numbers of co-channel signals and receive antennas. These are important system parameters. Therefore, it is useful to define the receiver *load factor* as

$$f(D, M) = \frac{D}{M} \quad (1.14)$$

where D and M are the numbers of co-channel signals and receive antennas, respectively. Using the load factor, three operational modes of a signal detector can be classified:

1. $f(D, M) < 1$: Underloaded case
2. $f(D, M) = 1$: Critically loaded case
3. $f(D, M) > 1$: Overloaded case.

Underloaded Receiver

If the receiver is underloaded CCI can easily be cancelled using linear SDMA techniques such as MRC or receive beamforming. Fig. 1.10 depicts an example of the array pattern if beamforming is employed at the receiver. Signal 1 is the signal of interest whereas signals 2, 3 and 4 are interfering signals. Due to the beamformer all interfering signals are nulled out and no CCI is present after beamforming at the receiver. This allows the use of linear detection techniques which have low computational complexity. After detecting signal 1 the antenna beams would be adjusted to detect signal 2 until all signals have been detected. In a receiver with an M -antenna array a linear beamformer can null out at most $M - 1$ interfering signals.

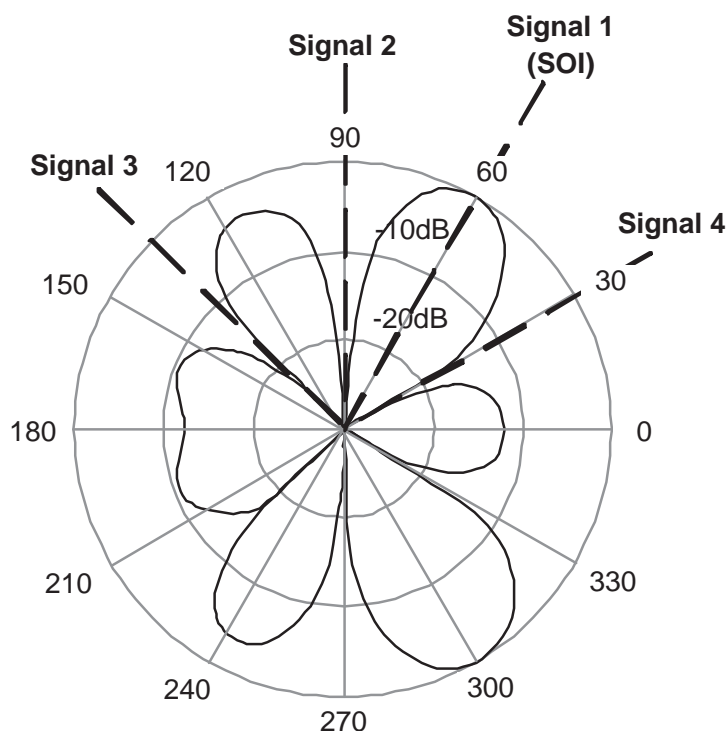


Figure 1.10 Example of the array pattern of a receive beamformer in an underloaded receiver.

Critically Loaded Receiver

If the number of transmitted signals is equal to the number of receive antennas the receiver is said to be critically loaded. This is the critical configuration because linear low complexity detectors lose performance and begin to fail to correctly detect the signals of interest. This is due to the fact that it is extremely difficult to cancel all CCI using linear processing techniques, e.g. by placing a null in the direction of $M - 1$ interfering signals.

Overloaded Receiver

Detection of the signals of interest is most challenging in the overloaded case. This is because linear processing techniques fail to cancel all CCI. Fig. 1.11 provides an example. Signal 1 is the signal of interest and signals 2, 3 are cancelled out. Signals 4, 5 and 6 still contribute to the received signal. These signals cause *residual CCI*. An overloaded signal detector must cope with residual CCI. This requires nonlinear

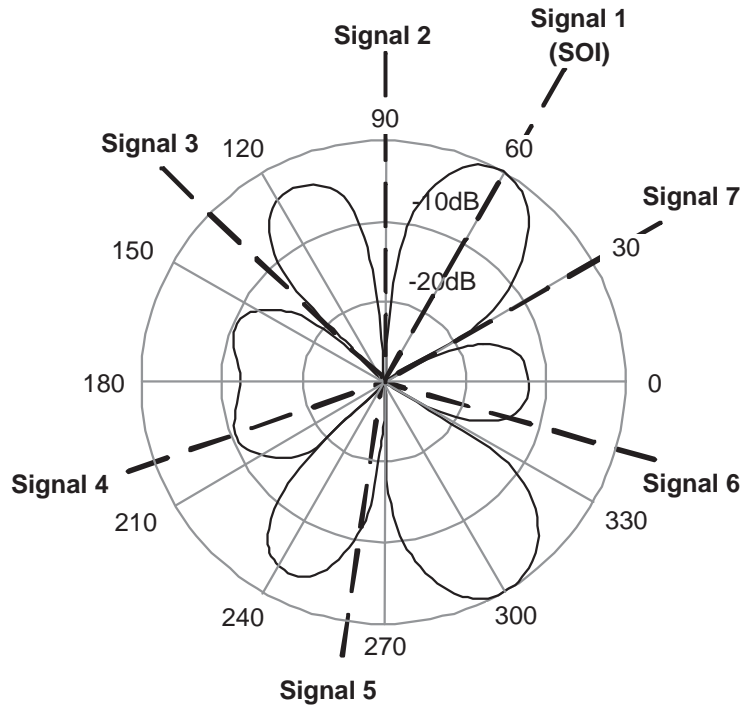


Figure 1.11 Example of the array pattern of a receive beamformer in an overloaded receiver.

signal detection techniques which often have high computational complexity compared to linear techniques. The most important design criteria for a practical signal detector suitable to work under overload are:

Performance: Error performance is usually the most important criteria when designing a signal detector. Ideally, a practical detector would achieve optimum or near optimum error performance. Since under overload, linear techniques cannot cancel all CCI, the signal detector must take into account any residual CCI to achieve good error performance.

Computational complexity: The nature of the detection problem of multiple co-channel signals is nonlinear with exponentially growing complexity with the number of signals. Therefore, nonlinear reduced complexity algorithms are of significant interest.

Adaptivity: In a practical communication system, parameters such as the physical channel and the number of co-channel signals often change with time. The signal

detector should be able to achieve good performance under a wide range of scenarios. It should easily cope with overloaded as well as underloaded and critically loaded operation modes.

1.3 OUTLINE AND THESIS CONTRIBUTIONS

The focus of this thesis is on the detection of multiple co-channel signals in overloaded system scenarios. The outline is as follows: In Chapter 2 a review of detection techniques for multiple co-channel signals is given. Chapter 3 develops a signal detector for overloaded receivers in AWGN channels. The work is extended to the frequency-flat Rayleigh fading channel in Chapter 4. In Chapter 5, a union bound on the error performance of signal detectors with reduced search symbol space is proposed. Examples of these include group-wise and list-based group-wise detectors. Chapter 6 presents conclusions and an outlook of possible future work. Much of the original work in this thesis appears in the following publications:

- M. Krause, D. P. Taylor and P. A. Martin, “On List Detection for Overloaded Receivers,” in *Proc. of the 18th Internat. Symposium on Personal, Indoor and Mobile Radio Communications (PIMRC’07)*, Athens, Greece, Sept. 2007.
- M. Krause, D. P. Taylor and P. A. Martin, “List Detection for Overloaded Receivers with a Uniform Linear Array,” in *Proc. of IEEE Military Communications Conference (MILCOM’07)*, Orlando, FL, USA, October 2007.
- M. Krause, D. P. Taylor and P. A. Martin, “A Unified Approach to List-Based Multiuser Detection in Overloaded Receivers,” *EURASIP Journal on Wireless Communications and Networking*, vol. 2008.
- M. Krause, D. P. Taylor and P. A. Martin, “An Iterative List-Based Multiuser Detector for Overloaded Receivers in a Rayleigh Fading Channel,” *Intern. Conf. on Commun. (ICC’09)*, Dresden, Germany, Jun. 2009.

Chapter 2

SIGNAL DETECTION FUNDAMENTALS

IN THIS chapter, fundamental signal detection concepts are presented. After a brief classification in Section 2.1, optimum Joint Maximum A Posteriori (JMAP) and Joint Maximum Likelihood (JML) detectors are derived in Section 2.2. Thereafter, suboptimum reduced complexity detection schemes are described with an emphasis on their application to overloaded receive scenarios. Section 2.3 presents an overview of linear detection techniques and Section 2.4 introduces nonlinear approaches to the detection problem. The chapter is concluded by Section 2.5 which provides a summary and outlines the research contributions of this thesis.

2.1 CLASSIFICATION OF DETECTION TECHNIQUES

In order to describe fundamental signal detection techniques, it is useful to first classify the different methods. In general, signal detection techniques can be divided into optimum and suboptimum algorithms. Optimum detectors such as JMAP and JML provide the performance bounds for underloaded, critically loaded as well as overloaded receivers. Both algorithms perform an exhaustive search over all possible received symbol combinations, which results in prohibitively high complexity if the number of co-channels or the alphabet size is large. This has motivated the search for suboptimum reduced complexity algorithms. Suboptimum algorithms can further be divided into *linear* and *nonlinear* algorithms¹.

¹JMAP and JML are also nonlinear detection techniques because both perform an exhaustive search over all possible symbol combinations. Most of their nonlinearity is due to a maximization process in conjunction with metric calculations based on the Euclidean distance.

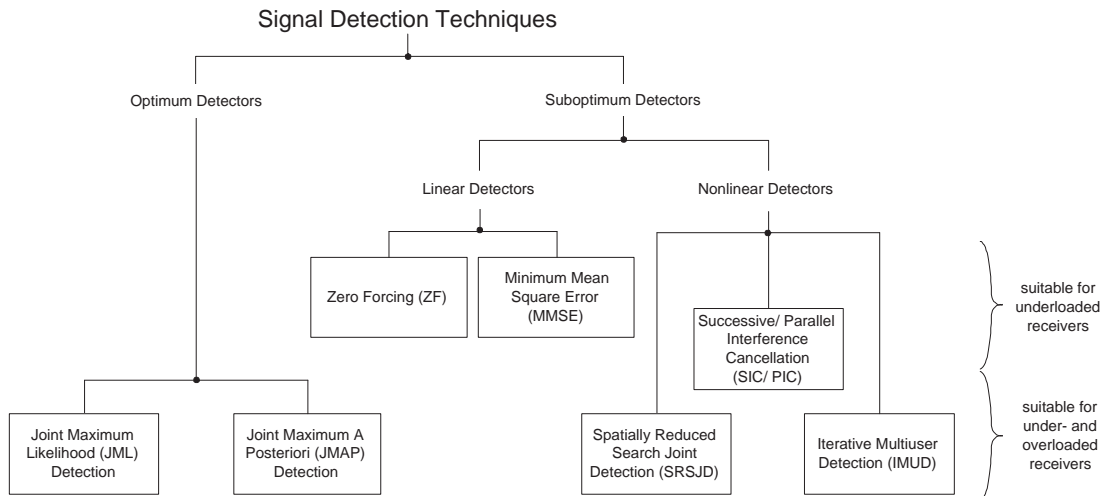


Figure 2.1 Overview of signal detection techniques.

Linear algorithms include Zero Forcing (ZF) and Minimum Mean Square Error (MMSE) detectors. Both have low computational complexity but poor performance under overload. The performance of the second group of nonlinear suboptimum algorithms ranges from relatively poor to near optimum performance in the overloaded case. Better performance comes at the cost of higher computational complexity. A classification chart is provided in Fig. 2.1. The suitability of the algorithms to the overloaded case is indicated on the right hand side of the chart.

2.2 OPTIMUM DETECTION

Optimum signal detectors for the SISO channel have been extensively studied in the literature, see e.g. [10, 11] for Maximum Likelihood (ML) and [12] for Maximum A Posteriori (MAP) detection. Joint detection for overloaded receivers was first proposed in [13]. ML approaches to estimating multiple synchronous co-channel signals impinging on an antenna array were studied in [14, 15]. This work was extended to the overloaded case in [16, 17]. In this section, JMAP and JML detectors for the case of multiple co-channel signals are described.

First, recall the frequency-flat fading channel model for the general case of D transmit signals impinging on a M -antenna receiver. Any time dependance in equations

is dropped for convenience. In this case, (1.7) is written as

$$\mathbf{x} = \mathbf{H}\mathbf{s} + \mathbf{n}, \quad (2.1)$$

where $\mathbf{x} \in \mathbb{C}^M$ and $\mathbf{n} \in \mathbb{C}^M$ are the received signal and white Gaussian noise vectors, respectively, $\mathbf{H} \in \mathbb{C}^{M \times D}$ is the channel matrix and $\mathbf{s} \in \mathcal{A}^D$ is the transmit symbol vector having integer-valued real and imaginary parts. The symbols $s_d \in \mathbf{s}$ are drawn from a finite alphabet \mathcal{A} . Furthermore, it is assumed that the elements $h_{md} \in \mathbf{H}$ are known to the receiver.

2.2.1 Joint Maximum A Posteriori Detection

The JMAP detector minimizes the probability that erroneous signals $\hat{\mathbf{s}} \neq \mathbf{s}$ are detected. The error probability $P_e(\mathbf{s})$ is given by

$$P_e(\mathbf{s}) = P(\hat{\mathbf{s}} \neq \mathbf{s}), \quad (2.2)$$

where the superscript $(\hat{\cdot})$ denotes the estimate. Eqn. (2.2) is equivalent to maximizing the probability of correctly estimating \mathbf{s} . This is denoted $P(\mathbf{s} = \hat{\mathbf{s}}|\mathbf{x}, \mathbf{H})$. Using probability density functions, the *a posteriori probability* that the vector $\hat{\mathbf{s}}$ was transmitted can be written as

$$P(\mathbf{s} = \hat{\mathbf{s}}|\mathbf{x}, \mathbf{H}) = \frac{Pr(\mathbf{s} = \hat{\mathbf{s}})f_{\mathbf{x}|\mathbf{s}, \mathbf{H}}(\mathbf{x}|\mathbf{s} = \hat{\mathbf{s}}, \mathbf{H})}{f_{\mathbf{x}|\mathbf{H}}(\mathbf{x}|\mathbf{H})} \quad (2.3)$$

where $Pr(\mathbf{s} = \hat{\mathbf{s}})$ is the *a priori probability* of $\hat{\mathbf{s}}$ being transmitted and $f_{\mathbf{x}|\mathbf{H}}(\mathbf{x}|\mathbf{H})$, $f_{\mathbf{x}|\mathbf{s}, \mathbf{H}}(\mathbf{x}|\mathbf{s} = \hat{\mathbf{s}}, \mathbf{H})$ are the conditional probability density functions of \mathbf{x} given \mathbf{H} and (\mathbf{s}, \mathbf{H}) , respectively. The term $f_{\mathbf{x}|\mathbf{s}, \mathbf{H}}(\mathbf{x}|\mathbf{s} = \hat{\mathbf{s}}, \mathbf{H})$ is referred to as *likelihood function*. Note that (2.3) is maximized by the symbol vector $\hat{\mathbf{s}}$ that maximizes the numerator $Pr(\mathbf{s} = \hat{\mathbf{s}})f_{\mathbf{x}|\mathbf{s}, \mathbf{H}}(\mathbf{x}|\mathbf{s} = \hat{\mathbf{s}}, \mathbf{H})$. This is known as the JMAP criterion and the JMAP

detector is written as

$$\hat{\mathbf{s}} = \arg \max_{\hat{\mathbf{s}} \in \mathcal{A}^D} \{f_{\mathbf{x}|\mathbf{s},\mathbf{H}}(\mathbf{x}|\mathbf{s} = \hat{\mathbf{s}}, \mathbf{H})Pr(\mathbf{s} = \hat{\mathbf{s}})\}. \quad (2.4)$$

Assuming independent bit values, the a priori probability $Pr(\mathbf{s})$ is given as the product of the individual probabilities $p(b_d^{(k)})$,

$$Pr(\mathbf{s}) = \prod_{d=1}^D \left[\prod_{k=1}^K p(b_d^{(k)}) \right] \quad (2.5)$$

where $b_d^{(k)} \in s_d$ is the k th bit of the d th transmitted symbol with $b_d^{(k)} = \{-1, 1\}$ and $K = \log_2 |\mathcal{A}|$. The a priori and a posteriori probabilities for each bit $b_d^{(k)}$ are often expressed as a log-likelihood ratio value² (L-value) [18].

The JMAP detector in (2.4) can be simplified by applying the channel model in (2.1) to obtain

$$f_{\mathbf{x}|\mathbf{s},\mathbf{H}}(\mathbf{x}|\mathbf{s} = \hat{\mathbf{s}}, \mathbf{H}) = f_{\mathbf{n}}(\mathbf{n}), \quad (2.6)$$

where the probability density function of the white Gaussian noise, \mathbf{n} , is [20]

$$f_{\mathbf{n}}(\mathbf{n}) = \frac{1}{(\pi N_0)^D} e^{-\frac{1}{N_0} \|\mathbf{n}\|^2}, \quad (2.7)$$

and $\|\cdot\|^2$ denotes the $L2$ -norm. Substituting \mathbf{n} in (2.7) with $\hat{\mathbf{n}} = \mathbf{x} - \mathbf{H}\mathbf{s}$ yields the JMAP detector as the nonlinear optimization problem

$$\hat{\mathbf{s}} = \arg \min_{\mathbf{s} \in \mathcal{A}^D} \{ \|\mathbf{x} - \mathbf{H}\mathbf{s}\|^2 - \ln Pr(\mathbf{s}) \}. \quad (2.8)$$

2.2.2 Joint Maximum Likelihood Detection

If all symbols $s_d \in \mathbf{s}$ are equiprobable the a priori probability $Pr(\mathbf{s})$ in (2.5) will be a constant and (2.3) is then maximized by

$$\hat{\mathbf{s}} = \arg \max_{\hat{\mathbf{s}} \in \mathcal{A}^D} f_{\mathbf{x}|\mathbf{s},\mathbf{H}}(\mathbf{x}|\mathbf{s} = \hat{\mathbf{s}}, \mathbf{H}). \quad (2.9)$$

²See e.g. [18, 19] for a detailed description of L-values.

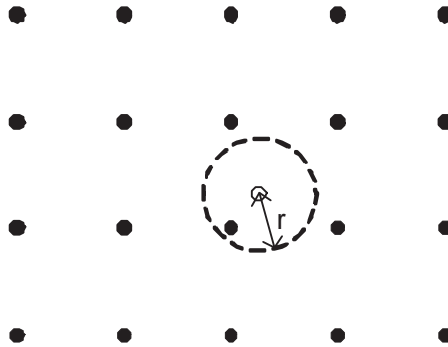


Figure 2.2 Geometrical interpretation of the integer least-squares problem.

This is known as the JML criterion. Inserting (2.6) and (2.7) into (2.9) gives the JML detector as

$$\hat{\mathbf{s}} = \arg \min_{\mathbf{s} \in \mathcal{A}^D} \|\mathbf{x} - \mathbf{H}\mathbf{s}\|^2. \quad (2.10)$$

2.2.3 Integer Least-Squares Problem

The information transmitted over a wireless link is usually mapped to a finite alphabet \mathcal{A} whose elements are integer numbers³. This leads to the definition of the *integer least-squares problem* over a finite lattice [21] as summarized in the following.

Given the vector $\mathbf{x} \in \mathbb{C}^M$, the matrix $\mathbf{H} \in \mathbb{C}^{M \times D}$ and a finite subset \mathcal{A} of an D -dimensional integer lattice \mathcal{Z}^D , find the vector $\mathbf{s} \in \mathcal{A}^D$ that minimizes

$$\min_{\mathbf{s} \in \mathcal{A}^D \subset \mathcal{Z}^D} \|\mathbf{x} - \mathbf{H}\mathbf{s}\|^2. \quad (2.11)$$

The integer least-squares problem in (2.11) has a geometrical interpretation as shown in Fig. 2.2. The matrix \mathbf{H} is also referred to as a *lattice generating* matrix because the vector $\mathbf{H}\mathbf{s}$ spans a D -dimensional lattice \mathcal{Z}^D . The solution to the integer least-squares problem is to find the closest lattice point. This requires a search over a discrete search space as described by the JMAP and JML detectors in (2.8) and (2.10). For a general matrix \mathbf{H} , this search has complexity of order $\mathcal{O} = (M|\mathcal{A}|^D)$ [13, 22]. The exponential complexity in the number of transmit signals D is the limiting

³This includes the common case of an alphabet \mathcal{A} with complex elements whose real and imaginary parts are integer numbers.

property of the optimum JMAP/ JML detectors because it prohibits their use in most practical receivers. Finding the optimum solution to the integer least-squares problem is, in general, NP-hard [23, 24]. Therefore, all practical reduced complexity detectors employ approximation techniques.

2.3 LINEAR DETECTORS

Linear detectors use linear mathematical operations to solve the integer least-squares problem in (2.11). These operations often involve matrix inversion and rounding to the nearest integer. Derivation and discussions of traditional ZF and MMSE linear detectors are widely available in the literature, see e.g. [25, 26]. Those are summarized below.

2.3.1 Zero-Forcing

Zero-forcing minimizes the difference between the estimate $\hat{\mathbf{s}} \in \mathcal{A}^D$ of the true transmitted symbol vector \mathbf{s} such that

$$\mathbf{s} - \hat{\mathbf{s}} = \mathbf{0}. \quad (2.12)$$

To find the solution of (2.12), the zero-forcing detector computes the pseudo-inverse, $\mathbf{H}^\dagger = (\mathbf{H}^H \mathbf{H})^{-1} \mathbf{H}^H$, of the matrix \mathbf{H} . When using the pseudo-inverse, the estimates $\hat{\mathbf{s}}$ will not necessarily be integer values and rounding to the nearest integer, denoted as $[\cdot]_{\mathcal{Z}}$ is required to obtain the solution to the integer least squares problem in (2.11). Hence, the zero-forcing detector is given by

$$\begin{aligned} \hat{\mathbf{s}} &= [\mathbf{H}^\dagger \mathbf{x}]_{\mathcal{Z}} \\ &= [\mathbf{s} + \mathbf{H}^\dagger \mathbf{n}]_{\mathcal{Z}}. \end{aligned} \quad (2.13)$$

The term $\mathbf{H}^\dagger \mathbf{n}$ in (2.13) tends to enhance and color the noise. This can severely degrade performance of the zero-forcing detector. Complexity is determined by the computations required to find the pseudo-inverse \mathbf{H}^\dagger . A stable algorithm for finding \mathbf{H}^\dagger performs the singular value decomposition $\mathbf{H} = \mathbf{U} \mathbf{\Sigma} \mathbf{V}^H$ which has complexity

$2MD^2 + 11D^3$ [27]. The pseudoinverse is then computed as $\mathbf{H}^\dagger = \mathbf{V}\mathbf{\Sigma}^{-1}\mathbf{U}^H$ with complexity $2MD^2$. Hence, the complexity of ZF is of order $\mathcal{O} = (MD^2)$.

2.3.2 Minimum Mean Square Error

The MMSE algorithm minimizes the expected value of the mean square error between the transmitted vector \mathbf{s} and a linear combination of the received vector \mathbf{x} . MMSE defines the error function

$$\begin{aligned}\Delta\hat{\mathbf{s}} &= \mathbf{s} - \hat{\mathbf{s}} \\ &= \mathbf{s} - \mathbf{W}^H\mathbf{x},\end{aligned}\tag{2.14}$$

where $\mathbf{W} \in \mathbb{C}^{M \times D}$ is a matrix of linear combining elements given by [28]

$$\mathbf{W} = [\mathbf{H}^H\mathbf{H} + \sigma^2\mathbf{I}_D]^{-1}\mathbf{H}^H.\tag{2.15}$$

In an underloaded receiver, the weight matrix \mathbf{W} effectively suppresses CCI. The MMSE detector obtains the weights $w_{md} \in \mathbf{W}$ by minimizing the expectation of the squared error cost function

$$\min E [\|\Delta\hat{\mathbf{s}}\|^2] = \min E [\{\mathbf{s} - \mathbf{W}^H\mathbf{x}\}^2].\tag{2.16}$$

The estimate of the d th transmit symbol, $\hat{s}_d \in \hat{\mathbf{s}}$, is then obtained by making the hard decision

$$\hat{s}_d = [\mathbf{w}^H[d]\mathbf{x}]_{\mathcal{Z}},\tag{2.17}$$

where $\mathbf{w}^H[d]$ denotes the d th row vector of \mathbf{W}^H . The MMSE solution to (2.16) is found by computing (2.17) for all $d = 1, 2, \dots, D$ symbols $\hat{s}_d \in \hat{\mathbf{s}}$. The computational complexity of MMSE is in the order $\mathcal{O} (M^2D^2 + 2MD^3 + \frac{15}{4}D^4)$ [29].

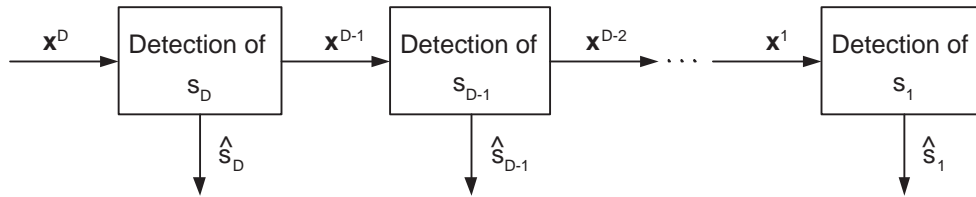


Figure 2.3 Block diagram of successive interference cancellation.

2.4 NONLINEAR DETECTORS

In an overloaded receiver linear detectors achieve poor performance because they fail to sufficiently mitigate the CCI. In contrast, classical nonlinear JMAP and JML detectors achieve optimum performance but have prohibitively high computational complexity. Under overload, nonlinear suboptimum detectors provide a better complexity/ performance tradeoff than linear and optimum detection techniques. The following gives an overview of existing suboptimum nonlinear detection techniques.

2.4.1 Successive Interference Cancellation

Successive Interference Cancellation (SIC) is based on the idea, that once a decision about a transmitted symbol has been made, the corresponding signal can be reconstructed at the receiver and subtracted from the received waveform [28]. The remaining waveform contains one less signal and thus has less CCI. The process is repeated with the next interferer until all signals have been estimated. A block diagram is provided in Fig. 2.3. SIC has several disadvantages over optimum JMAP/ JML detectors. One is that the first signal to be detected suffers from CCI from all $(D - 1)$ other signals. The result is poor performance especially when the received signals have equal power. Another drawback of this method is that the sequential detection process introduces a delay of D computation stages in order to carry out the cancellation process.

The algorithm used in the SIC detection stages is not specified. In the literature the linear MMSE filter has been proposed because of its low computational complexity and ability to suppress CCI, see e.g. [30, 31, 32]. In a joint MMSE-SIC detector, the standard MMSE algorithm is altered. The detector first detects the symbol \hat{s}_D . This is

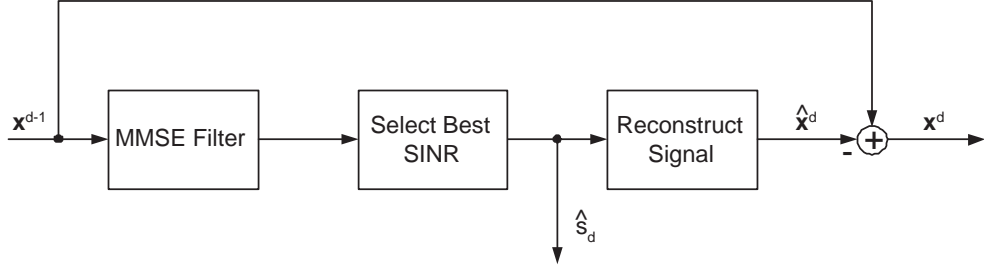


Figure 2.4 MMSE-SIC single stage.

used to reconstruct the received signal in level D , denoted \hat{x}^D . In the next stage, $D-1$, the interference contribution from the hard estimate \hat{s}_D is cancelled by subtracting it from the received signal vector \mathbf{x}^D . Fig. 2.4 illustrates a single stage of the MMSE-SIC architecture. The new signal \mathbf{x}^{D-1} is used instead of \mathbf{x} in (2.17) to estimate \hat{s}_{D-1} . The general expression for the received signal vector for stage d is [30]

$$\mathbf{x}^{d-1} = \mathbf{x}^d - \mathbf{h}(d)\hat{s}_d \quad (2.18)$$

where $\mathbf{h}(d)$ denotes the d th column of \mathbf{H} . Since at each detection stage the interference associated with the symbol \hat{s}_d is removed, an iterative update process for \mathbf{H} is required. The matrix \mathbf{H}^{d-1} is computed by deleting the d th column from the previous matrix \mathbf{H}^d . Hence, \mathbf{H}^{d-1} is given by [30]

$$\mathbf{H}^{d-1} = \begin{pmatrix} h_{11} & h_{12} & \dots & h_{1d-1} \\ h_{21} & h_{22} & \dots & h_{2d-1} \\ \vdots & \vdots & \ddots & \vdots \\ h_{M1} & h_{M2} & \dots & h_{Md-1} \end{pmatrix}, \quad d = 2, 3, \dots, D \quad (2.19)$$

The new matrix \mathbf{H}^{d-1} is used in (2.15) to obtain the optimum MMSE weights. Complexity is dominated by the computations required to detect each individual signal. Compared to MMSE, the MMSE-SIC detector requires more computation due to the multiple MMSE stages and interference cancellation processes. However, it achieves better performance.

2.4.2 Parallel Interference Cancellation

In contrast to SIC, Parallel Interference Cancellation (PIC) requires iterative processing. It avoids the decoding delay of SIC in that it uses the signal estimates from the previous iteration to cancel all interfering co-channel signals [33]. Its main drawback is that convergence cannot be guaranteed [33]. PIC can also be combined with MMSE detection, see e.g. [34, 35, 36]. The simulation of MMSE-PIC in an overloaded detector [36] showed that it is practical for receivers with load factor $f(D, M) < 1.5$ only. MMSE-PIC is not suitable for moderately and heavily overloaded scenarios where $f(D, M) \geq 1.5$.

2.4.3 Spatially Reduced Search Joint Detection

Spatially Reduced Search Joint Detection (SRSJD) [22] considers transmission of multiple co-channel signals through an AWGN channel with LOS links between the multiple transmitters and the receive node. The signals impinge on a multiple antenna receiver with UCA geometry⁴. The channel model is described by (1.8). Neglecting any time dependence, (1.8) is written as

$$\mathbf{x} = \mathbf{A}\mathbf{s} + \mathbf{n}, \quad (2.20)$$

where $\mathbf{A} = [\mathbf{a}(1) \ \mathbf{a}(2) \ \dots \ \mathbf{a}(D)]$ is the $M \times D$ composite array response matrix with $\mathbf{a}(d) = [a_1 \ a_2 \ \dots \ a_M]^T$ denoting the array steering vector for the d th signal. For the UCA geometry, the components $a_m \in \mathbf{a}(d)$ are given by (1.9).

SRSJD is a two stage SDMA algorithm: A preprocessor first mitigates CCI using linear receive beamforming. The main processor employs a spatial version of the Viterbi Algorithm (VA) to search over subsets of the symbol space in order to detect the signals of interest. Fig. 2.5 depicts a system model of the SRSJD receiver.

An alternative form of the JML criterion in (2.10) can be derived which lends itself

⁴SRSJD is restricted to special antenna array geometries and AWGN channels as will become evident later.

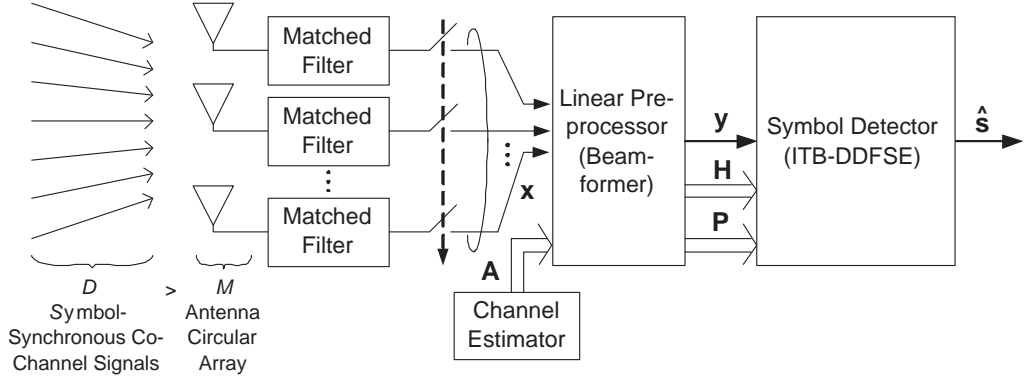


Figure 2.5 System model of an overloaded receiver employing Spatially Reduced Search Joint Detection (SRSJD).

to suboptimal approximation [22]. Eqn. (2.10) can be written as [22]

$$\hat{\mathbf{s}} = \arg \min_{\mathbf{s} \in \mathcal{A}^D} \left[(\mathbf{x} - \mathbf{A}\mathbf{s})^H \mathbf{\Phi}_{nn}^{-1} (\mathbf{x} - \mathbf{A}\mathbf{s}) \right], \quad (2.21)$$

where $\mathbf{\Phi}_{nn} = E[\mathbf{nn}^H]$ is the autocorrelation of the noise vector \mathbf{n} . Eqn. (2.21) is equivalent to

$$\hat{\mathbf{s}} = \arg \min_{\mathbf{s} \in \mathcal{A}^D} \left[\mathbf{s}^H \mathbf{A}^H \mathbf{\Phi}_{nn}^{-1} \mathbf{A} \mathbf{s} - 2\Re \left\{ (\mathbf{\Phi}_{nn}^{-1} \mathbf{A} \mathbf{s})^H \mathbf{x} \right\} \right]. \quad (2.22)$$

Defining the square matrix $\mathbf{H} \in \mathbb{C}^{D \times D}$ and the vector $\mathbf{y} \in \mathbb{C}^D$ such that [22]

$$\mathbf{H}^H \mathbf{H} = \mathbf{A}^H \mathbf{\Phi}_{nn}^{-1} \mathbf{A} \quad (2.23)$$

and

$$\mathbf{H}^H \mathbf{y} = \mathbf{A}^H \mathbf{\Phi}_{nn}^{-1} \mathbf{x} \quad (2.24)$$

yields a trellis-oriented beamformer as [22]

$$\begin{aligned} \mathbf{y} &= \left((\mathbf{H}^H)^\dagger \mathbf{A} \mathbf{\Phi}_{nn}^{-1} \right) \mathbf{x} \\ &= \mathbf{W} \mathbf{x}. \end{aligned} \quad (2.25)$$

Each row of matrix \mathbf{W} performs an implicit beamforming operation. For selected array

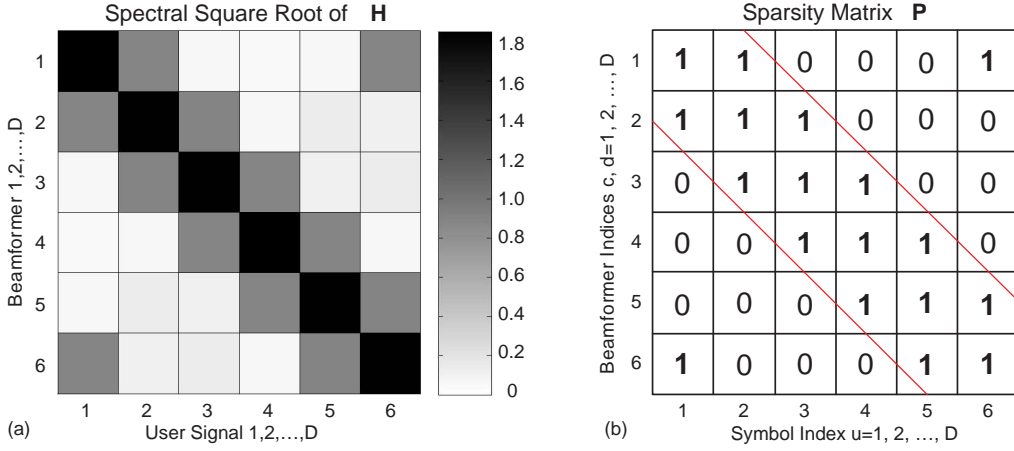


Figure 2.6 (a) Spectral square root $(\mathbf{H}^H \mathbf{H})^{(1/2)}$ of \mathbf{H} and (b) sparsity matrix \mathbf{P} for a $M = 5$ element UCA with $D = 6$ transmit signals have equal energy and are uniformly spaced in AOA. A DEIR threshold of 0.1 is used to distinguish the “high” and “low” energy elements $h_{du} \in \mathbf{H}$ in \mathbf{P} .

geometries, e.g. the UCA, \mathbf{W} focuses the energy of the d th beam to the d th signal so that each signal has “dominant” energy⁵ in at least one beam. As a result, \mathbf{W} acts as an interference rejection filter. Fig. 2.6 (a) illustrates the spectral square root of matrix \mathbf{H} , denoted $(\mathbf{H}^H \mathbf{H})^{(1/2)}$, for a $M = 5$ element UCA. There are $D = 6$ equal energy signals impinging on the antenna array. These are sent by single antenna transmitters uniformly spaced in Angle of Arrival (AOA). It is clear that most of the energy is concentrated along the main diagonal of $(\mathbf{H}^H \mathbf{H})^{(1/2)}$. It can further be seen that the linear beamformer mitigates CCI but cannot completely cancel it in the overloaded case⁶.

The matrix \mathbf{W} acts as a *trellis-oriented* beamformer because a spatial detection trellis can be constructed based on the diagonally-banded structure of \mathbf{H} [22]. At first, the SRSJD receiver distinguishes between matrix elements with “high” and “low” energy. This is done using a selection criterion which is referred to as Desired Energy to Interference Ratio (DEIR). The DEIR for the d th transmitter is defined as [22]

$$DEIR[d] = \frac{E \left[|h_{dd} s_d|^2 \right]}{E \left[\left| \sum_{u \in \bar{U}_e[d]} h_{du} s_u \right|^2 \right]} = \frac{|h_{dd}|^2}{\left| \sum_{u \in \bar{U}_e[d]} h_{du} \right|^2}, \quad (2.26)$$

⁵At this stage, the term “dominant” refers to an intuitive definition of matrix elements with significant energy. The mathematical definition is given later.

⁶Hence the off-diagonal non-zero elements in Fig. 2.6 (a).

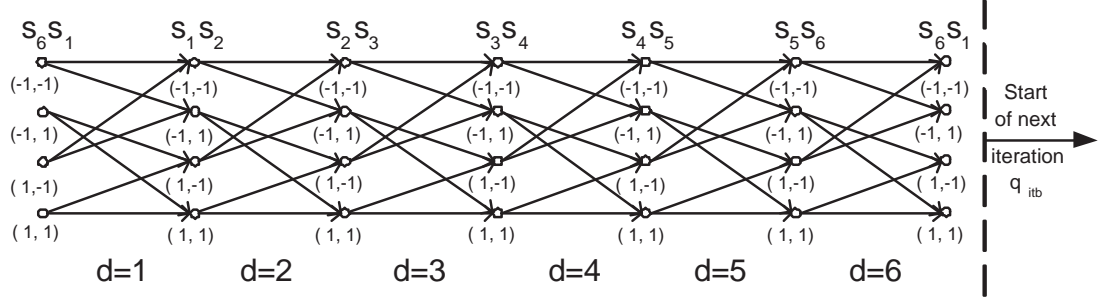


Figure 2.7 Spatial trellis constructed from the sparsity matrix \mathbf{P} in Fig. 2.6(b) for the detection of BSPK symbols.

where the set $U_e[d]$ is referred to as an *enumeration set*⁷. It includes column indices of the elements $h_{du} \in \mathbf{h}[d]$ with “*high*” energy. A predefined threshold is used with the DEIR criterion (2.26) in order to distinguish “*high*” and “*low*” energy elements.

For the example in Fig. 2.6(a), the enumeration sets are $U_e[1] = \{1, 2, 6\}$, $U_e[2] = \{1, 2, 3\}$, $U_e[3] = \{2, 3, 4\}$, $U_e[4] = \{3, 4, 5\}$, $U_e[5] = \{4, 5, 6\}$ and $U_e[6] = \{5, 6, 1\}$. The corresponding sets $\bar{U}_e[d]$ contain all other column indices and are said to be from “*low*” energy elements. If (2.26) is applied to each individual row of \mathbf{H} a corresponding *sparsity matrix* \mathbf{P} can be constructed. The matrix \mathbf{P} is a $(D \times D)$ binary matrix that contains unity entries for elements with “*high*” energy and zeros for elements with “*low*” energy in the corresponding matrix \mathbf{H} .

Symbol detection is performed with the aid of a spatial trellis constructed from the matrix \mathbf{P} . Fig. 2.7 depicts the trellis for the $M = 5$ receive antenna, $D = 6$ signals example of Fig. 2.6. The trellis is shown for BPSK symbols⁸. Each state represents a unique combination of two neighboring symbols and the arrows indicate state transitions. The trellis has a *tail-biting* structure due to the diagonally-banded form of \mathbf{H} . This enables iterative processing. The states at the d th stage of the trellis, $\sigma[d]$, are defined as [22]

$$\sigma[d] = \{s_u | u \in U_e[d-1] \cap U_e[d]\}. \quad (2.27)$$

⁷The name was chosen in [22] because the detection algorithm enumerates over the symbols indexed by $U_e[d]$.

⁸The extension to other signal types is straight forward.

Let $\mu[d] = |\sigma[d]|$ denote the state size at the d th trellis stage. The state sequence in Fig. 2.7 is $\sigma[1] = \{s_6s_1\}$, $\sigma[2] = \{s_1s_2\}$, $\sigma[3] = \{s_2s_3\}$, $\sigma[4] = \{s_3s_4\}$, $\sigma[5] = \{s_4s_5\}$, $\sigma[6] = \{s_5s_6\}$ with constant size $\mu[d] = 2$. The symbol detection algorithm is referred to as Iterative Tail Biting-Delayed Decision Feedback Sequence Estimation (ITB-DDFSE)⁹ [22]. Its purpose is to find the minimum cost path through the trellis. ITB-DDFSE reduces the search complexity by using a partial state estimate¹⁰, $\hat{\nu}[d]$, for all symbols not contained in $\sigma[d]$.

Iterative Tail-Biting Delayed Decision Feedback Sequence Estimation (ITB-DDFSE)

For each transition from a previous state i to a new state j at stage d of the trellis, compute the error metric [22]

$$e_{itb}^{(i,j)}[d] = \left| y[d] - \hat{y}_{itb}^{(i,j)}[d] \right|^2, \quad (2.28)$$

where $y[d]$ is a component of \mathbf{y} and $\hat{y}_{itb}^{(i,j)}[d]$ is the candidate component. It is formed by the sum of an “enumeration component” $\hat{y}_e^{(i,j)}[d]$ and a “feedback component” $\hat{y}_{fb}[d]$ given as [22]

$$\begin{aligned} \hat{y}_{itb}^{(i,j)}[d] &= \hat{y}_e^{(i,j)}[d] + \hat{y}_{fb}[d] \\ \hat{y}_e^{(i,j)}[d] &= \sum_{u \in U_e[d]} h_{du} s_u \\ \hat{y}_{fb}[d] &= \sum_{u \in \bar{U}_e[d]} h_{du} \hat{s}_u. \end{aligned} \quad (2.29)$$

Symbol values for $\hat{y}_e^{(i,j)}[d]$ are drawn from the corresponding $i \rightarrow j$ transition, whereas symbol values for $\hat{y}_{fb}[d]$ are drawn from a partial state estimate $\hat{\nu}[d]$. The partial state estimate $\hat{\nu}[d]$ contains tentative symbols and is updated after computing all transitions at stage d . The algorithm continues with the next stage $d = d + 1$ for all iterations $q_{itb} = 1, 2, \dots, Q_{itb}$ around the trellis. Typically, $Q_{itb} = 2$ or 3 trellis iterations

⁹The algorithm is effectively a spatial version of the original Viterbi algorithm by Forney [10].

¹⁰This is in fact the principle of Delayed Decision Feedback Sequence Estimation (DDFSE) [37].

Table 2.1 Summary of ITB-DDFSE symbol detection

-
1. Define $\mu_{\max} = \max_{1 \leq d \leq D} \{\mu[d]\}$ and allocate an $|\mathcal{A}|^{\mu_{\max}} \times 1$ array of cumulative partial path metrics $\xi^{(i)}[d]$. Initialize $\xi^{(i)}[d=1] = 0, \forall i = 0, 1, \dots, |\mathcal{A}|^{\mu_{\max}} - 1$.
 2. Allocate a list of D arrays of size $|\mathcal{A}|^{\mu[d]} \times 1$ to store surviving transitions into the $\sigma[d+1] = j^{th}$ state at the d^{th} trellis stage, $i_s^{(j)}[d]$.
 3. For each iteration around the trellis, $q_{itb} = 1, 2, \dots, Q_{itb}$, and each value of (next state) $j = 0, 1, \dots, |\mathcal{A}|^{\mu[d+1]} - 1$ of each stage $d = 1, 2, \dots, D$
 - Find the survivor $i_s^{(j)}[d] = \arg \min_{i \in T_j} \left\{ \xi^{(i)}[d] + e_{itb}^{(i,j)}[d] \right\}$, where $i \in T_j$ denotes all valid $i \rightarrow j$ transitions.
 - Update the list of cumulative partial path metrics,

$$\xi^{(j)}[d+1] = \min_{i \in T_j} \left\{ \xi^{(i)}[d] + e_{itb}^{(i,j)}[d] \right\}.$$
 - Update the partial state estimate $\hat{v}[d+1]$ by picking out symbol values from the surviving path.
 4. Choose a trellis state at the final stage with the least cumulative cost.
 5. Trace back and reconstruct the least cost path from the survivor list $i_s^{(j)}[d]$.
 6. Translate the states of the least cost path into a symbol sequence.
-

are used [22]. Table 2.1 summarizes the ITB-DDFSE symbol detection algorithm. The computational complexity of the algorithm is in the order $\mathcal{O} \left(\sum_{d=1}^D |\mathcal{A}|^{\mu[d]} \right)$ [22].

2.4.4 Iterative Multiuser Detection

Iterative Multiuser Detection (IMUD) [38, 39] considers multiple signals that are transmitted over a frequency-flat fading channel. The channel model of such a system is given in (2.1). IMUD uses iterative group-wise detection to reduce the computational complexity compared to the optimum JML/ JMAP detectors. It relies on soft cancellation of already detected symbol groups using A Posteriori Probability (APP) values.

IMUD splits up (2.1) into N_G groups with G signals in each group from which the symbols are detected. For simplicity, only BPSK symbols are considered¹¹ so that each symbol is mapped into one bit. Using group notation, the received signal vector for

¹¹The extension to other signal types is straight forward.

group j can be written as [39]

$$\begin{aligned}\mathbf{x} &= \mathbf{H}_j \mathbf{s}_j + \left(\sum_{i=1, i \neq j}^{N_G} \mathbf{H}_i \mathbf{s}_i + \mathbf{n} \right) \\ &= \mathbf{x}_j + \mathbf{x}_U,\end{aligned}\quad (2.30)$$

where $\mathbf{H}_i, \mathbf{H}_j \in \mathbf{H}$ are the group matrices and $\mathbf{s}_i, \mathbf{s}_j \in \mathbf{s}$ are the group symbol vectors for groups i and j , respectively. Note that $\mathbf{x}_j = \mathbf{H}_j \mathbf{s}_j$ denotes contributions from the current decision group j to the received signal vector \mathbf{x} and $\mathbf{x}_U = \sum_{i=1, i \neq j}^{N_G} \mathbf{H}_i \mathbf{s}_i + \mathbf{n}$ represents the undesired or interference contributions. The detection likelihood function for the j th group is given by [39]

$$f_{\mathbf{x}|\mathbf{H}, \mathbf{s}_j}(\mathbf{x}|\mathbf{H}, \mathbf{s}_j) = \frac{1}{2\pi |\mathbf{R}_U|} e^{-\frac{1}{2}(\mathbf{x} - \mathbf{H}_j \mathbf{s}_j)^\dagger \mathbf{R}_U^{-1} (\mathbf{x} - \mathbf{H}_j \mathbf{s}_j)}, \quad (2.31)$$

where \mathbf{R}_U is the covariance matrix of \mathbf{x} . It is defined as [39]

$$\mathbf{R}_U = \sum_{i=1, i \neq j}^{N_G} \mathbf{H}_i \mathbf{H}_i^\dagger + N_0 \mathbf{I}. \quad (2.32)$$

Following from (2.31), the group symbol vector for the j th group is estimated as [39]

$$\hat{\mathbf{s}}_j = \arg \min_{\mathbf{s}_j} (\mathbf{x} - \mathbf{H}_j \mathbf{s}_j)^\dagger \mathbf{R}_U^{-1} (\mathbf{x} - \mathbf{H}_j \mathbf{s}_j). \quad (2.33)$$

Eqns. (2.31) and (2.33) can be changed into iterative form, which may be denoted as

$$f_{\mathbf{x}^{(j,\gamma)}|\mathbf{H}, \mathbf{s}_j}(\mathbf{x}^{(j,\gamma)}|\mathbf{H}, \mathbf{s}_j) = \frac{1}{2\pi |\mathbf{R}_U^{(j,\gamma)}|} e^{-\frac{1}{2}(\mathbf{x}^{(j,\gamma)} - \mathbf{H}_j \mathbf{s}_j)^\dagger \mathbf{R}_U^{(j,\gamma)-1} (\mathbf{x}^{(j,\gamma)} - \mathbf{H}_j \mathbf{s}_j)} \quad (2.34)$$

and

$$\hat{\mathbf{s}}_j = \arg \min_{\mathbf{s}_j} \left(\mathbf{x}^{(j,\gamma)} - \mathbf{H}_j \mathbf{s}_j \right)^\dagger \mathbf{R}_U^{(j,\gamma)-1} \left(\mathbf{x}^{(j,\gamma)} - \mathbf{H}_j \mathbf{s}_j \right), \quad (2.35)$$

where γ is the iteration index and $\mathbf{x}^{(j,\gamma)}$ is the modified sample vector for the j th group from which the previously estimated symbols have been removed. The APP of the i th

Table 2.2 Summary of Iterative Multiuser Detection (IMUD)

-
1. Initialize the $D \times 1$ vector $\boldsymbol{\mu} = \mathbf{0}$ and the $D \times D$ matrix $\boldsymbol{\Sigma} = \mathbf{I}$.
 2. Set $j = 1$ and $\gamma = 1$.
 3. For each iteration $\gamma = 1$ to γ_{\max} ,
 - For $j = 1$ to N_G ,
 - Selects the members of group j from all undetected signals¹².
 - Find the joint APP values for the signals of group j using (2.34), (2.41) and (2.42).
 - Calculate the APPs ($Pr(s_{ij}|\mathbf{x})$) from group j with (2.36).
 - Compute the means μ_{ij} and variances σ_{ij}^2 for group j with (2.37) and (2.38).
 - Update $\mu_j^{(\gamma)}$ and $\boldsymbol{\Sigma}_j^{(\gamma)}$.
 - Calculate $\mathbf{x}^{(j,\gamma)}$ with (2.41).
 - Randomize the signal order.
 4. Make a hard decision for each signal using the APPs.
-

signal in the j th group is expressed as [39]

$$Pr(s_{ij} = s | \mathbf{x}^{(j,\theta)}) = \frac{p(s_{ij} = s, \mathbf{x}^{(j,\theta)})}{\sum_{s=\pm 1} p(s_{ij} = s, \mathbf{x}^{(j,\theta)})}. \quad (2.36)$$

The IMUD algorithm uses soft interference cancellation between groups. This requires computation of the mean and variance of each signal in the group. The mean μ_{ij} and variance σ_{ij} for signal i in group j are [39]

$$\mu_{ij} = Pr(s_{ij} = 1) - Pr(s_{ij} = -1) \quad (2.37)$$

$$\sigma_{ij}^2 = 1 - \mu_{ij}^2. \quad (2.38)$$

For the γ th iteration and after detecting group j , the group mean and variance are

¹²Different ordering algorithms for group selection are proposed in [38, 39].

given by [39]

$$\boldsymbol{\mu}_j^{(\gamma)} = \begin{pmatrix} \mu_{1j} \\ \mu_{2j} \\ \vdots \\ \mu_{Gj} \end{pmatrix} \quad (2.39)$$

$$\boldsymbol{\Sigma}_j^{(\gamma)} = \begin{pmatrix} \sigma_{1j}^2 & 0 & \dots & 0 \\ 0 & \sigma_{2j}^2 & 0 & \vdots \\ \vdots & 0 & \ddots & 0 \\ 0 & \dots & 0 & \sigma_{Gj}^2 \end{pmatrix}. \quad (2.40)$$

The sample vector for the next group ($j + 1$) becomes [39]

$$\mathbf{x}^{(j+1,\gamma)} = \mathbf{x} - \sum_{i=1, i \neq j+1}^{N_G} \mathbf{H}_i \boldsymbol{\mu}_i^{(\gamma)} \quad (2.41)$$

and the covariance in (2.32) changes to [39]

$$\mathbf{R}_U^{(j,\gamma)} = \sum_{i=1, i \neq j}^{N_G} \mathbf{H}_i \boldsymbol{\Sigma}_i^{(\gamma)} \mathbf{H}_i^\dagger + N_0 \mathbf{I}. \quad (2.42)$$

The IMUD algorithm can now be described as shown in Table 2.2. The complexity of IMUD is exponential in the group size and linear in the number of groups [38]. Hence, the complexity order is $\mathcal{O}(N_G |\mathcal{A}|^G)$.

2.5 CONCLUSIONS

In this chapter, fundamental signal detection techniques were presented with an emphasis on their application to overloaded receivers. While substantial literature is available that investigates the underloaded receiver, the published literature on signal detection

under overload is limited. This has motivated the work presented in this thesis.

The classical detection problem leads to the definition of the integer least-squares problem over a finite lattice. Finding the solution requires a search over a discrete space. Optimum detectors such as JMAP and JML search over all possible symbol combinations. Computational complexity is exponential in the number of signals and therefore prohibits their use in most practical systems. This has led to the development of suboptimum detection algorithms that can find the solution to the least-squares problem with significantly lower complexity than the optimum detectors. Two classes of algorithms have evolved: linear and nonlinear.

Fig. 2.8 provides a qualitative complexity-performance overview of the algorithms described in this chapter¹³. It considers the case of moderate to severe overload with load factor $f(D, M) = \frac{M}{D} \geq 1.5$. Moreover, it is assumed that the receiver has perfect CSI.

Achievable performance and computational complexity are bounded¹⁴ by optimum JMAP and JML algorithms. Linear suboptimum detectors include ZF and MMSE. Both offer low complexity but achieve poor performance due to linear approximation that fails to adequately cancel CCI under overload, see e.g. [22, 40]. Computational complexity is often determined by a matrix inversion operation. Performance of the linear MMSE detector can be improved if it is combined with nonlinear interference cancellation, e.g. in MMSE-SIC [32] and MMSE-PIC [34].

Nonlinear suboptimum detectors offer better performance than linear algorithms under overload. This comes at the cost of higher computational complexity. Interference cancellation techniques rely on energy differences in the received signals. Therefore, performance is poor if two or more received signals have similar energies. Nonlinear detection techniques such as SRSJD [22] and IMUD [38, 39] rely on a nonlinear search over a discrete symbol subspace. Given a suitable selection of the search space, these

¹³A quantitative comparison of the different detectors is not given due to the different channel models considered in the literature. Moreover, different signal types and simulation parameters are used in references cited in this chapter allowing a qualitative comparison only.

¹⁴Note that only uncoded transmission is considered in this thesis. The use of error and space-time coding techniques will generally result in better performance than uncoded transmission.

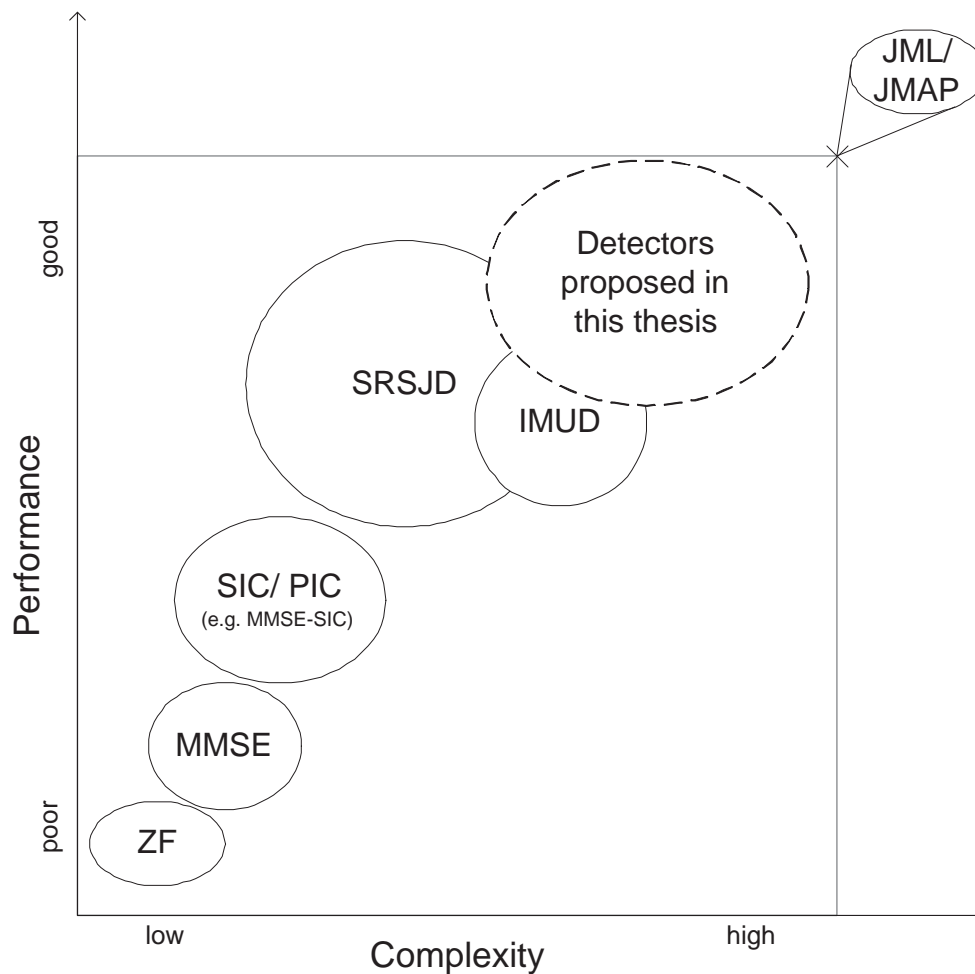


Figure 2.8 Performance/ complexity tradeoff of signal detection algorithms under moderate to severe overload.

algorithms can offer a good performance/ complexity tradeoff. SRSJD is an SDMA algorithm based on receive beamforming and a nonlinear search using a spatial trellis. Its application is restricted to AWGN channels and certain array geometries, e.g. circular arrays. In contrast, IMUD works in frequency-flat fading channels and can, in principle, be extended to frequency-selective fading channels. The algorithm forms decision groups from the received signals and defines a search subspace for the symbols of each group. IMUD performance is impaired due to correlation introduced by soft interference cancellation during the iterative process.

Fig. 2.8 clearly shows the gap between the previously described suboptimum detectors and the optimum JMAP/ JML detectors. This gap is filled by the algorithms

proposed in this thesis, which offer good performance at reduced complexity.

Chapter 3

DETECTOR FOR THE AWGN CHANNEL

A UNIFIED approach to the separation and detection of multiple co-channel signals in an overloaded receive system is now developed. In this chapter the signals are considered to be transmitted through an AWGN channel with LOS links between the transmitters and the receiver. The signals are incident on a receiver with an antenna array. The proposed receiver combines a linear preprocessor with an iterative nonlinear suboptimum detector. Simulation results show that this can approximate optimum JML performance at lower complexity. Complexity savings are achieved by first, exploiting the spatial separation of the transmitters to mitigate CCI in the preprocessor stage and second, by estimating residual CCI in the following symbol detection stage. The proposed symbol detection algorithm is applied to receivers with either a UCA or a ULA. The preprocessor is implemented using either a special purpose spatial filter to directly mitigate the CCI or MRC to achieve diversity gain thereby mitigating CCI. Simulation results and a complexity analysis indicate that the approach is suitable for practical application.

The chapter is organized as follows: The system model and receiver structure are introduced in Section 3.1. Preprocessor architectures are discussed in Section 3.2. Section 3.3 describes the proposed symbol detection algorithm. Simulation results and a complexity analysis are given in Sections 3.4 and 3.5, respectively. Conclusions are drawn in Section 3.6.

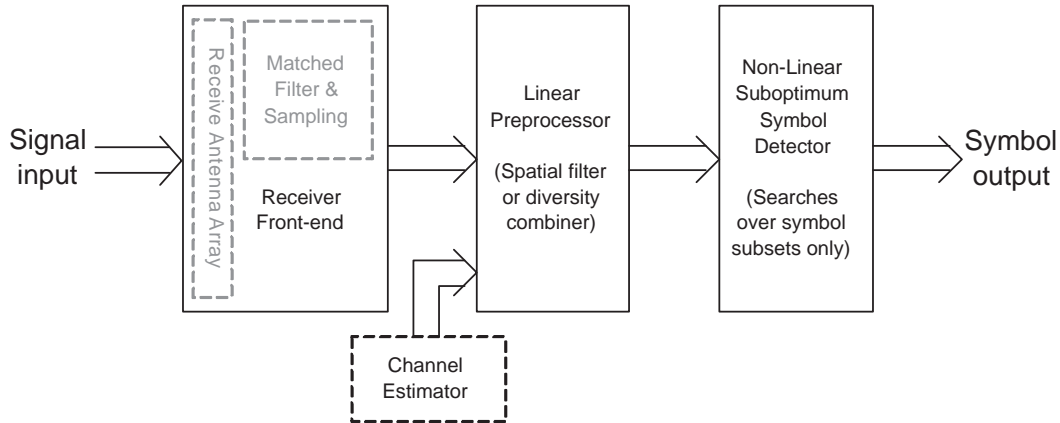


Figure 3.1 Overall block diagram of the proposed reduced complexity receiver.

3.1 SYSTEM MODEL AND RECEIVER STRUCTURE

Consider an overloaded communication system with multiple co-channel signals present at the receive antenna array. The block diagram of the proposed receiver is shown in Fig. 3.1. It consists of three main stages: a receiver front-end, a linear preprocessor and a nonlinear symbol detector. The front-end includes the antenna array, matched filter and signal sampling. A channel estimator supplies the receiver with CSI. The purpose of the linear preprocessor is to mitigate CCI. It is either implemented as a spatial filter¹ or as a diversity combiner. The preprocessed signal is then passed on to the detection stage where a nonlinear search algorithm detects the transmitted symbols. Fig. 3.2 illustrates the receiver structure in more detail.

It is assumed throughout that the receiver operates under overload with load factor $f(D, M) = \frac{D}{M}$ (defined in (1.14)) and $f(D, M) > 1$. A practical system will not always be overloaded. However, this is the most challenging case because complexity of optimum JML detection is often prohibitive and suboptimal linear detectors are ineffective in such cases. The receiver structure in Fig. 3.2 and the proposed Parallel Detection with Interference Estimation (PD-IE) detection algorithm also work when the system is underloaded.

The D co-channel signals are transmitted through an AWGN channel and impinge

¹A typical example of a spatial filter is a receive beamformer.

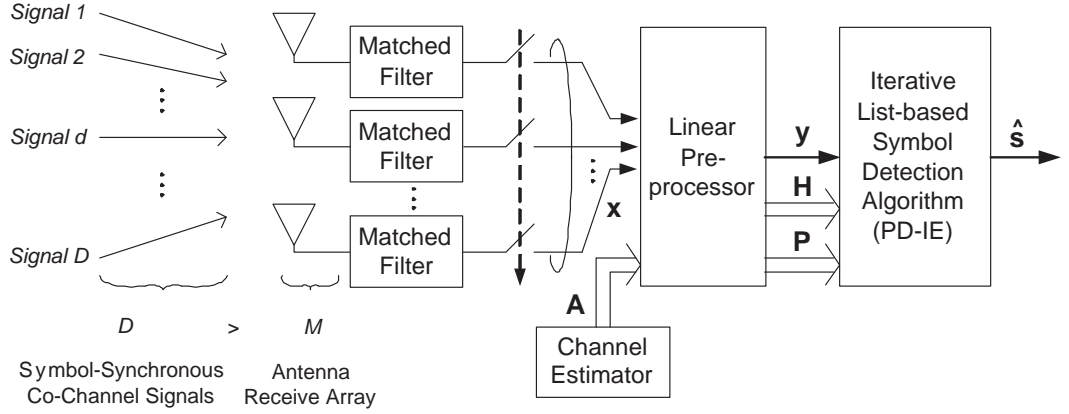


Figure 3.2 Receiver structure for the PD-IE detector.

on M receive antennas having either UCA or ULA geometry². The signals are passed through a filter matched to the transmitted pulse shape and are then sampled at rate T^{-1} to give the receive vector $\mathbf{x} \in \mathbb{C}^M$ in each T -s symbol interval. The corresponding channel model is given by (1.8). Suppressing the time dependence of all quantities for notational simplicity, (1.8) is written as

$$\mathbf{x} = \mathbf{A}\mathbf{s} + \mathbf{n}, \quad (3.1)$$

where $\mathbf{s} \in \mathcal{A}^D$ denotes the symbol vector $\mathbf{s} = [s_1 \ s_2 \ \dots \ s_D]^T$ containing the transmitted symbols s_d . Each symbol s_d is independent and uniformly drawn from the alphabet \mathcal{A} . In an AWGN channel the vector \mathbf{s} is multiplied by the $M \times D$ composite array response matrix $\mathbf{A} = [\mathbf{a}(1) \ \mathbf{a}(2) \ \dots \ \mathbf{a}(D)]$ with $\mathbf{a}(d) \in \mathbb{C}^M$ being the array steering vector for the d th signal. The components $a_m \in \mathbf{a}(d)$ are given by (1.9) for the UCA and (1.10) for the ULA, respectively. In a more complex channel, \mathbf{A} also includes the channel response. It is assumed that \mathbf{A} is computed by a channel estimator which estimates the direction of arrival for each of the D signals. This is shown in Fig. 3.2. The quantity $\mathbf{n} \in \mathbb{C}^M$ in (3.1) is the temporally uncorrelated noise vector with zero mean and autocorrelation $\mathbf{\Phi}_{nn} = E[\mathbf{nn}^H]$, where $E[\cdot]$ denotes the expectation operation. For spatially uncorrelated noise, $\mathbf{\Phi}_{nn} = \sigma_n^2 \mathbf{I}$, where σ_n^2 denotes the noise variance and \mathbf{I} is the $M \times M$ identity matrix.

²The PD-IE detection approach presented here can be applied to arbitrary antenna geometries. Specific considerations are limited to these two.

3.2 PREPROCESSOR

The estimated array response matrix \mathbf{A} and the received signal vector \mathbf{x} , following matched filtering and sampling, are input to a preprocessor as shown in Fig. 3.2. It exploits the spatial separation of the transmitters to mitigate CCI effects so as to enable complexity reduction in the subsequent detection stage³.

The preprocessor is based on an alternate form of the JML criterion defined in (2.10) that lends itself to sub-optimal approximation. Considering the channel model in (3.1) and assuming no intersymbol interference, JML leads to the symbol by symbol detector given by [17]

$$\hat{\mathbf{s}} = \arg \min_{\mathbf{s} \in \mathcal{A}^D} (\mathbf{x} - \mathbf{A}\mathbf{s})^H \Phi_{nn}^{-1} (\mathbf{x} - \mathbf{A}\mathbf{s}), \quad (3.2)$$

where $(\cdot)^H$ denotes Hermitian transpose.

The key to approximating (3.2) is to find a transformation that maps the $M \times 1$ received vector \mathbf{x} into the $D \times 1$ vector $\mathbf{y} = [y[1] \ y[2] \ \dots \ y[D]]^T$ and the $M \times D$ array response matrix \mathbf{A} into a $D \times D$ square matrix $\mathbf{H} = [\mathbf{h}[1] \ \mathbf{h}[2] \ \dots \ \mathbf{h}[D]]$, where $y[d]$ is the d th component of \mathbf{y} and $\mathbf{h}[d] = [h_{d1} \ h_{d2} \ \dots \ h_{dD}]$ is the corresponding row vector of \mathbf{H} with elements h_{du} . The required transformation maps

$$\begin{aligned} \mathbf{x}_{(M \times 1)} &\mapsto \mathbf{y}_{(D \times 1)} \\ \mathbf{A}_{(M \times D)} &\mapsto \mathbf{H}_{(D \times D)}, \end{aligned} \quad (3.3)$$

where $\mathbf{y} \in \mathbb{C}^D$ is called the transformed receive vector and $\mathbf{H} \in \mathbb{C}^{D \times D}$ is the transformed channel matrix⁴. There are two basic interpretations possible for the transformation of (3.3), either spatial filtering or diversity combining. Both are essentially projection operations and in each case, the solution is a complex weight matrix $\mathbf{W} \in \mathbb{C}^{D \times M}$

³This will become evident later.

⁴Even though \mathbf{H} is named the channel matrix it does not describe a physical channel as the matrix \mathbf{H} does in Chapter 1. The matrix \mathbf{H} here can be understood as the matrix describing a MIMO channel from D transmit antennas to a receiver with D “virtual” receive antennas. It includes the “real” channel \mathbf{A} as well as the linear preprocessor transformations.

such that

$$\mathbf{y} = \mathbf{W}\mathbf{x}. \quad (3.4)$$

3.2.1 Spatial Filtering

A spatial filter exploits the fact that signals incident on the antenna array with greater spread in AOA interfere with each other less than signals that are closely spaced in AOA. CCI from signals reasonably widely spaced in AOA can thus be effectively reduced. This is essentially a beamforming operation.

The matrix \mathbf{W} can be derived from the JML criterion of (3.2) by choosing \mathbf{y} and \mathbf{H} such that [22]

$$\begin{aligned} \mathbf{H}^H \mathbf{H} &= \mathbf{A}^H \mathbf{\Phi}_{nn}^{-1} \mathbf{A} \\ \mathbf{H}^H \mathbf{y} &= \mathbf{A}^H \mathbf{\Phi}_{nn}^{-1} \mathbf{x}. \end{aligned} \quad (3.5)$$

This choice satisfies the mapping of (3.3) and yields the JML detector in the form [22]

$$\begin{aligned} \hat{\mathbf{s}} &= \arg \min_{\mathbf{s} \in \mathcal{A}^D} \|\mathbf{y} - \mathbf{H}\mathbf{s}\|^2 \\ &= \arg \min_{\mathbf{s} \in \mathcal{A}^D} \sum_{d=1}^D |y[d] - \mathbf{h}[d]\mathbf{s}|^2 \\ &= \arg \min_{\mathbf{s} \in \mathcal{A}^D} \sum_{d=1}^D \left| y[d] - \sum_{u=1}^D h_{du} s_u \right|^2. \end{aligned} \quad (3.6)$$

Multiplying (3.5) with the pseudo-inverse $(\mathbf{H}^H)^\dagger$ gives (3.4) with $\mathbf{W} = (\mathbf{H}^H)^\dagger \mathbf{A}^H \mathbf{\Phi}_{nn}^{-1}$. The matrix \mathbf{W} here is a trellis oriented MIMO beamformer since each row places a beam in the direction of only one transmitted signal [22]. It increases the number of observation samples and acts as a noise whitening interference rejection filter. The elements of \mathbf{y} denote the received signal in each of the D beams and each row of \mathbf{H} shows the energy contribution of each transmitter to the received signal in the d th beam.

As an example, Fig. 3.3(a) shows the form of \mathbf{H} for a receiver employing a spatial

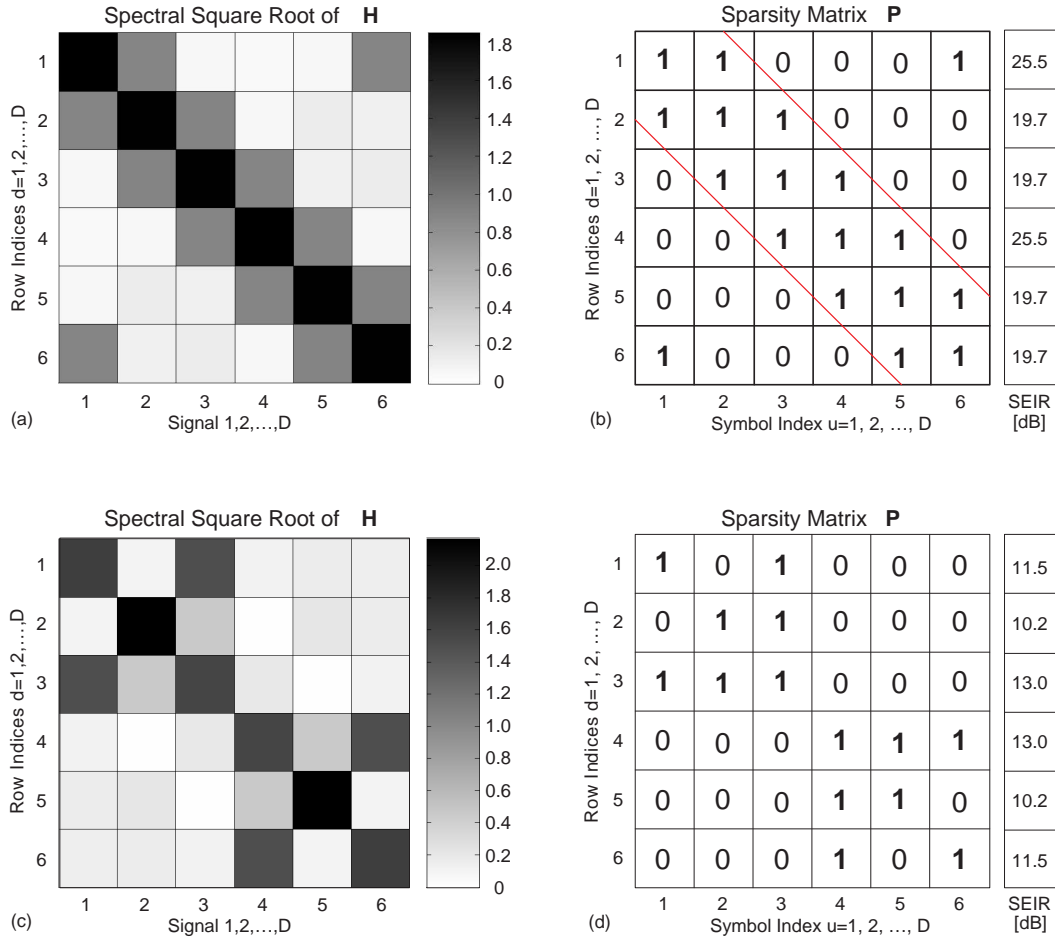


Figure 3.3 (a) Spectral square root $(\mathbf{H}^H \mathbf{H})^{(1/2)}$ of \mathbf{H} and (b) sparsity matrix \mathbf{P} for a 5-element UCA. The transmitted signals are uniformly spaced in AOA. (c) Spectral square root $(\mathbf{H}^H \mathbf{H})^{(1/2)}$ of \mathbf{H} and (d) sparsity matrix \mathbf{P} for a 5-element ULA. The received signal AOAs are uniform within $\theta_{max} = \pm 60^\circ$. There are $D = 6$ equal energy signals present at the receive antennas. Elements with '1' in \mathbf{P} are obtained by using the SEAIR and SSSER criteria (defined later) with thresholds $T_1 = 2$ and $T_2 = 0.1$, respectively.

filter as a preprocessor. Here, the receiver has a $M = 5$ -element UCA front-end with radius $R = 0.2\lambda$. Data signals are sent from $D = 6$ single antenna transmitters. The signals present at the receive antennas are assumed to have equal energy⁵ and to be uniformly spaced in AOA. It is clear that most of the energy is concentrated on or near the main diagonal of \mathbf{H} , resulting in a banded structure, where in each row only a few elements contain most of the energy. If the impinging signals have different energies or are unevenly distributed in AOA the energy is still centered on the main diagonal of \mathbf{H} but is not evenly distributed.

3.2.2 Diversity Combining

Another interpretation of (3.3) is to consider it from the viewpoint of diversity combining. In this case, multiple copies of the same information bearing signal are combined so as to maximize the instantaneous SNR at the output [41]. MRC is the classical and optimal [25] diversity combining technique. The combiner output is a weighted linear combination of the signal replicas. For MRC with perfect CSI, the optimum weight matrix in (3.4) is $\mathbf{W} = \mathbf{A}^H$ [25].

MRC tries to map the received vector \mathbf{x} into the transformed vector \mathbf{y} such that each signal has maximum SNR in one of the components of \mathbf{y} . Defining the channel matrix \mathbf{H} such that

$$\mathbf{H} = \mathbf{A}^H \mathbf{A} \quad (3.7)$$

allows the JML detector to be written as in (3.6) with the difference being the definitions of \mathbf{W} and \mathbf{H} in the two cases. The row elements of \mathbf{H} denote the energy contribution from each of the D signals to the received signal in which the SNR of the corresponding signal is maximized.

In the example of Fig. 3.3(c), the form of \mathbf{H} is illustrated for a receiver using MRC as a preprocessor. The antenna array considered in this example is a $M = 5$ -element ULA. Again, there are $D = 6$ signals with equal received energy. The transmitters are

⁵This is the more difficult case because many detection techniques exploit differences in the received signal energies (e.g. SIC, PIC) and suffer performance degradation if the signals have similar energies.

assumed uniformly spaced within the array's view angle, which is defined as $\theta_{max} = \pm 60^\circ$. Hence, the transmitter's azimuth AOAs are $\theta_d = \{\pm 60^\circ, \pm 36^\circ, \pm 12^\circ\}$ with $d = 1, 2, \dots, 6$. The antenna elements are spaced at distance $B = 3\lambda$ apart. In this example \mathbf{H} appears to be block diagonal and there are elements with “high”⁶ energy further away from the main diagonal. Thus \mathbf{H} does not have a banded structure and is therefore not trellis-oriented. This is in contrast to Fig. 3.3(a), where the energy is uniformly concentrated along the main diagonal.

3.2.3 Spatial Filtering vs. Diversity Combining

The beam forming spatial filter works best if relatively closely spaced antenna elements are available to form beam patterns. To ensure sufficient correlation, the element spacing should be no more than half a wave length at the carrier frequency. This follows from the *Nyquist sampling theorem* [42]. Under overload, it is important to note that a linear spatial filter can not cancel more than $D = M - 1$ interfering co-channel signals (see e.g. [43]). This is a physical limitation since if M beams can be formed with a null between each pair of neighboring beams, there can be only $M - 1$ nulls (cf. Fig. 1.9). Under overload and with increasing load factor $f(D, M)$, the advantage of beam forming tends to be lost as there will still be significant residual CCI in each component of \mathbf{y} .

In contrast, diversity combining requires little or no cross-correlation between the antenna elements. If a signal at one element goes through a deep fade, it is then unlikely that the other elements encounter a deep fade for the same signal at the same time. Hence, combining the signals from different elements can improve receive performance as there is nearly always good reception at one of them. Antenna spacing is usually on the order of several carrier frequency wave lengths and does not satisfy the Nyquist sampling theorem. As a result, spatial aliasing and grating lobes occur [44] when the array properties are considered. This is offset by the diversity gain attained. The goal is to develop a detection algorithm that works well with both types of preprocessors.

⁶At this stage, the term “high” refers to an intuitive definition of matrix elements with significant energy. The mathematical definition is given later.

3.2.4 Sparsity Pattern

The two examples of the channel matrix \mathbf{H} in Fig. 3.3(a) and Fig. 3.3(c) show that only a few elements in each row contain most of the signal energy. A detector can exploit the energy differences with the aid of a sparsity matrix \mathbf{P} . This is derived from \mathbf{H} and contains unity entries for elements with “high” energy and zeros for elements with “low”⁷ energy [22]. The sparsity matrix is a square binary matrix, $\mathbf{P} \in \mathbb{N}_2^{D \times D}$, which in row vector notation is denoted $\mathbf{P} = [\mathbf{p}[1] \ \mathbf{p}[2] \ \dots \ \mathbf{p}[D]]$. Each element p_{du} in \mathbf{P} corresponds to the element h_{du} in \mathbf{H} for $d, u = 1, \dots, D$. Its use allows provides reduced complexity approximations to the JML detector of (3.2). The sparsity matrices corresponding to Fig. 3.3(a) and Fig. 3.3(c) are shown in Fig. 3.3(b) and Fig. 3.3(d), respectively.

In order to specify \mathbf{P} , *enumeration sets* $U_e[d]$ are defined. This was first proposed in [22]. The term “enumeration set” is used because the detection algorithm enumerates over all possible combinations of transmit symbols $\{s_u | u \in U_e[d]\}$. An enumeration set $U_e[d]$ consists of the column indices of the unity elements in each matrix row $\mathbf{p}[d] \in \mathbf{P}$. Therefore, the indices in $U_e[d]$ indicate signals with “high” energy. For example, in the first row of \mathbf{H} in Fig. 3.3(a), $U_e[1] = \{6, 1, 2\}$ and $\bar{U}_e[1] = \{3, 4, 5\}$ are the column signal indices of elements with “high” and “low” energy, respectively. Hence, the corresponding sparsity pattern in Fig. 3.3(b) is $\mathbf{p}[1] = [1 \ 1 \ 0 \ 0 \ 0 \ 1]$.

The quality of the sparsity matrix found depends on the criterion used to choose its elements. A so-called Desired Energy to Interference Ratio (DEIR) criterion was proposed in [22]. It uses a threshold which, if chosen poorly, erroneously treats signals with low energy as high energy signals, and results in higher detection complexity than necessary for a given level of performance. A poor choice can also lead to considering strong signals as low energy signals, which results in lower complexity at the cost of poorer overall performance.

Here, a novel approach to the construction of \mathbf{P} is proposed. It is based on

⁷The criteria for separating matrix elements with “high” and “low” energy are described later. Here it is only an intuitive definition.

two energy ratio selection criteria, namely the Signal to Strongest Signal Energy Ratio (SSSER) and the Signal Energy to Average Interference Ratio (SEAIR). These appear more robust over a wider range of co-channel signal strengths than the use of existing criteria. Each criterion employs an empirically chosen threshold as a selection parameter. The choice of the thresholds determines to a large extent the complexity/ performance tradeoff in the subsequent signal detection algorithm. The proposed approach considers energy separation of the preprocessed received signals and is thus limited to scenarios where sufficient separation can be achieved. This means it tends to perform poorly if, after preprocessing, the signals have energies that are too similar. As a result, either too few or too many signals with high energy would be selected. This can occur under extreme overload when using a linear preprocessor⁸. While the selection of too few signals may result in low computational complexity and poor error performance, the choice of too many signals yields better error rate at possibly prohibitively high computational complexity. The optimum choice of the thresholds is an open research topic. In general, the choice depends on the desired complexity/ performance tradeoff, the receive antenna geometry, the type of preprocessor, the number of receive antennas M and the number of co-channel signals D .

The construction of \mathbf{P} using the SSSER and SEAIR criteria is now described. Both differ from the DEIR of [22] (described in Subsection 2.4.3).

The SSSER criterion is defined as

$$SSSER[d, u] = \frac{E [|h_{du}s_u|^2]}{E \left[\max_{1 \leq v \leq D} |h_{dv}s_v|^2 \right]} = \frac{|h_{du}|^2}{\max_{1 \leq v \leq D} |h_{dv}|^2}, \quad (3.8)$$

where the numerator represents the energy of the u th element in the d th row of $\mathbf{h}[d] \in \mathbf{H}$ and the denominator is the energy of the strongest signal in that row. Fig. 3.4(a) provides a graphical illustration.

The SEAIR criterion considers the energy of an element h_{du} in relation to the overall energy of the interference. Assuming that in the d th row of \mathbf{H} the column

⁸In fact, this is a fundamental limitation if a linear preprocessor is used in an overloaded receiver.

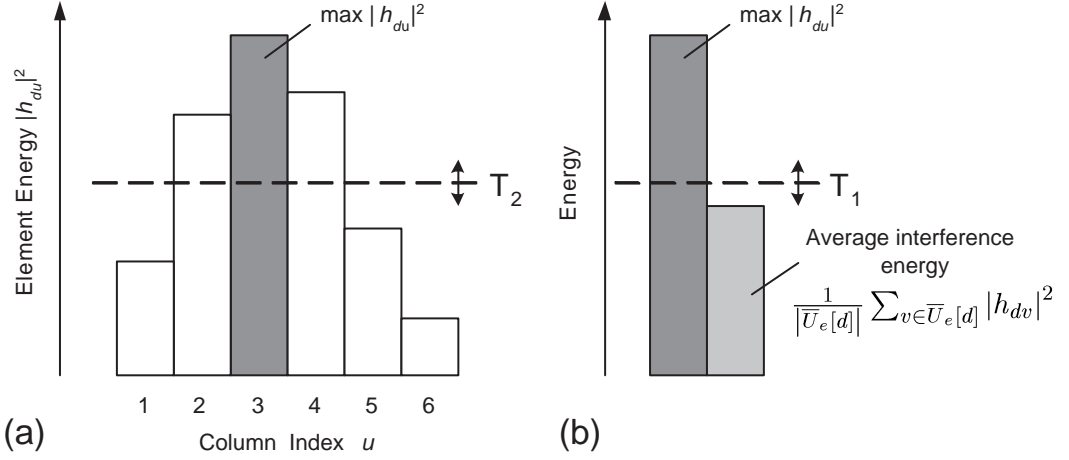


Figure 3.4 Graphical illustration of the (a) SSSER and (b) SEAIR criteria which are computed for the d th row $\mathbf{h}[d] \in \mathbf{H}$.

indices are grouped into the two sets $U_e[d]$ and $\bar{U}_e[d]$, the SEAIR is then defined as

$$SEAIR[d, u] = \frac{E \left[|h_{du}s_u|^2 \right]}{\frac{1}{|\bar{U}_e[d]|} E \left[\sum_{v \in \bar{U}_e[d]} |h_{dv}s_v|^2 \right]} = \frac{|h_{du}|^2}{\frac{1}{|\bar{U}_e[d]|} \sum_{v \in \bar{U}_e[d]} |h_{dv}|^2}, \quad (3.9)$$

where the numerator represents the channel coefficient of a high energy signal h_{du} and the denominator is the average interference energy with $|\bar{U}_e[d]| = D - |U_e[d]|$ denoting the number of signals outside the enumeration set $U_e[d]$. The SEAIR criterion is illustrated in Fig. 3.4(b).

Table 3.1 describes the algorithm for construction of the sparsity matrix \mathbf{P} . In each matrix row, the SSSER and SEAIR criteria are computed for up to $\rho[d] \leq D$ row elements h_{du} . The parameter $\rho[d]$ therefore defines the maximum allowed number of high energy elements in the d th row. It is arbitrarily set depending on constraints on the computational complexity of the receiver. Ideally, one would choose $\rho[d] = D$ to allow for all elements to be considered as high energy. This, however, may result in prohibitively high complexity of the subsequent detection algorithm in practical receivers.

The sparsity pattern $\mathbf{p}[d] \in \mathbf{P}$ is constructed by assigning unity entries to all symbols corresponding to indices $u \in U_e[d]$ and zero entries for those where $u \in \bar{U}_e[d]$.

Table 3.1 Construction of the sparsity matrix \mathbf{P}

-
1. Initialize the $D \times D$ matrix \mathbf{P} and set $\mathbf{P} = \mathbf{0}$.
 2. For matrix row $d = 1$ to D
 - (a) Initialize the set of column indices of high energy elements $U_e[d]$ and the complementary set of column indices of low energy elements $\overline{U}_e[d]$. Set $U_e[d] = \{\emptyset\}$ and $\overline{U}_e[d] = \{1, 2, \dots, D\}$.
 - (b) For $\varepsilon = 1$ to $\rho[d]$
 - i. Find the column index $u^{(\varepsilon)}$ of the element $h_{du}^{(\varepsilon)}$ which has the ε th greatest energy in the d th row,

$$u^{(\varepsilon)} = \arg \max_{1 \leq u \leq D}^{(\varepsilon)} |h_{du}|^2.$$
 - ii. Compute the SSSER for the element $h_{du}^{(\varepsilon)}$ using (3.8).
 - iii. If $SSSER[d, u^{(\varepsilon)}] < T_2$ terminate the algorithm.
 - iv. Remove the index $u^{(\varepsilon)}$ from the set $\overline{U}_e[d]$ and compute the SEAIR value for the element $h_{du}^{(\varepsilon)}$ using (3.9).
 - v. If $SEAIR[d, u^{(\varepsilon)}] < T_1$ store the index $u^{(\varepsilon)}$ in the set $\overline{U}_e[d]$ and terminate the algorithm.
 - vi. Store the index $u^{(\varepsilon)}$ in the set $U_e[d]$. Update the d th row of the sparsity matrix, $\mathbf{p}[d] \in \mathbf{P}$, by setting the corresponding element $p_{du} = 1$.
 - vii. Set $\varepsilon = \varepsilon + 1$.
-

From $\mathbf{p}[d] \in \mathbf{P}$, the two symbol sets

$$\tau[d] = \{s_u | u \in U_e[d]\}, \quad \omega[d] = \{s_u | u \in \overline{U}_e[d]\} \quad (3.10)$$

are obtained as the sets of high and low energy symbols, respectively. The low energy symbol sets, $\omega[d]$, are referred to as interfering symbol sets, since they correspond to residual CCI which degrades the detection of the signals in the high energy symbol sets, $\tau[d]$. For the examples in Fig. 3.3, the SEAIR and SSSER thresholds were found empirically and are set to $T_1 = 2$ and $T_2 = 0.1$, respectively. These yield the sets $\tau[1] = \{s_6, s_1, s_2\}$ and $\omega[1] = \{s_3, s_4, s_5\}$ in Fig. 3.3(a), and $\tau[1] = \{s_1, s_3\}$ and $\omega[1] = \{s_2, s_4, s_5, s_6\}$ in Fig. 3.3(c). Similar results are obtained for all other values of d corresponding to the other rows of \mathbf{H} . Note that different numbers of signals and receive antennas, D and M , as well as different antenna array geometries and element spacing may require changing the empirically determined thresholds T_1 and T_2 . However, once T_1 and T_2 have been set for a given M , the algorithm appears robust over a wide range of D . This is shown in Fig. 3.5. It provides an example of the $M = 5$

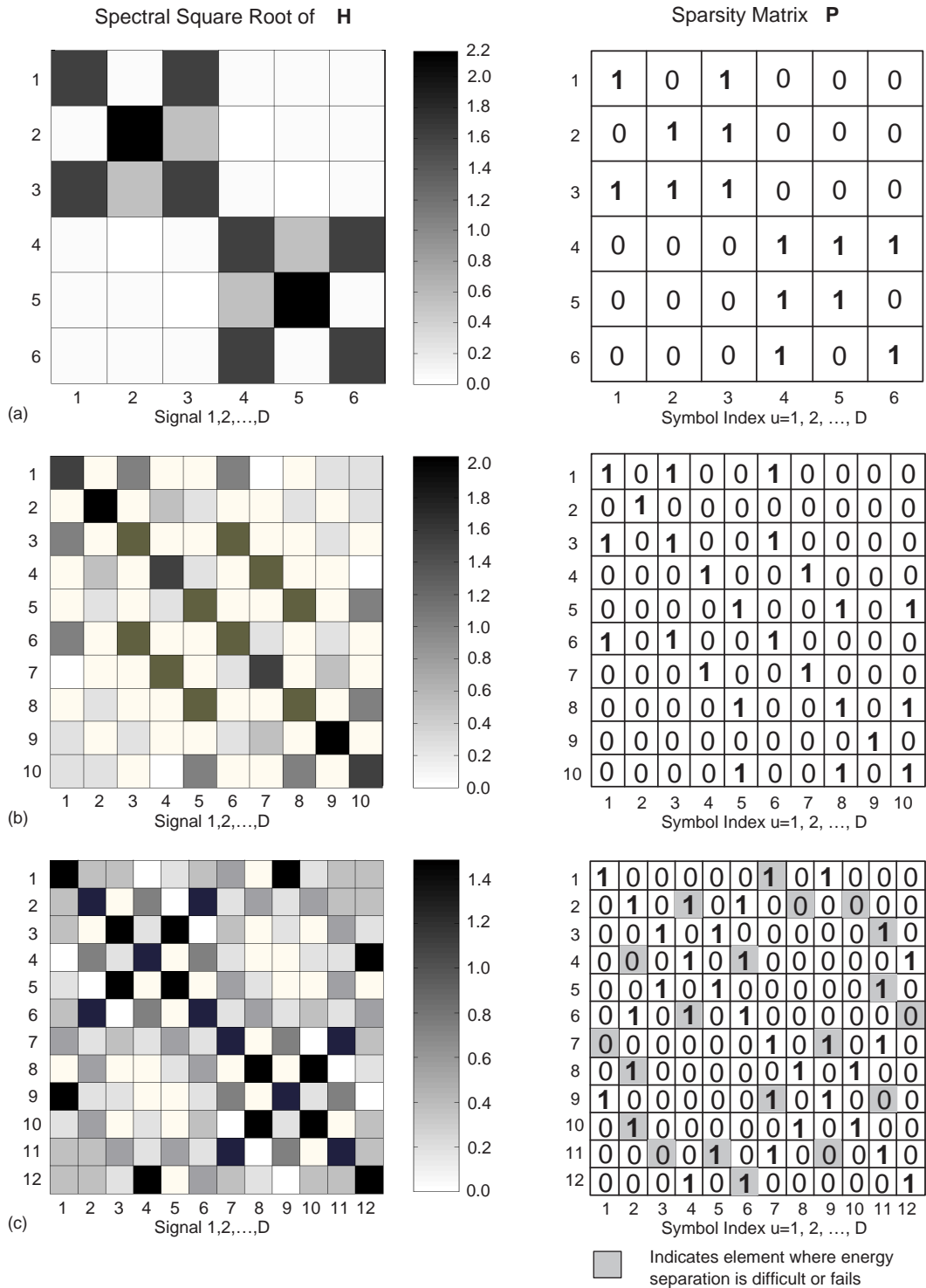


Figure 3.5 Spectral square root $(\mathbf{H}^H \mathbf{H})^{(1/2)}$ of \mathbf{H} and corresponding sparsity matrix \mathbf{P} for a $M = 5$ antenna ULA with $D = 6$, $D = 10$ and $D = 12$ transmitters using the SSSER and SEAIR criteria with thresholds $T_1 = 2$ and $T_2 = 0.1$. The impinging signals have equal energy and their AOAs are uniform within $\theta_{max} = \pm 60^\circ$.

antenna ULA of Figs. 3.3(c) and 3.3(d) for various numbers of transmit signals D . The receiver load factor $f(D, M)$ is varied with the choices $D = 6$ (Fig. 3.5(a)), $D = 10$ (Fig. 3.5(b)) and $D = 12$ (Fig. 3.5(c)) transmit signals resulting in $f(D, M) = 1.2$, 2 and 2.4, respectively. Again, the spectral square root of \mathbf{H} and the corresponding sparsity matrix \mathbf{P} are shown. The thresholds for the SSSER and SEAIR criteria remain unchanged with $T_1 = 2$ and $T_2 = 0.1$. It is clear that for $f(D, M) = 1.2$ (Fig. 3.5(a)) and $f(D, M) = 2$ (Fig. 3.5(b)) the linear preprocessor correctly separates the elements in \mathbf{H} into high and low energy subsets. At higher load factors, e.g. $f(D, M) = 2.4$ (Fig. 3.5(c)), the preprocessor has difficulty focussing the channel energies. This results in many matrix elements with similar energy levels. The SSSER and SEAIR criteria perform poorly under these conditions and start to fail to correctly distinguish between low and high energy elements. This is evident in Fig. 3.5(c).

3.3 PARALLEL DETECTION WITH INTERFERENCE ESTIMATION (PD-IE)

In this section, the proposed symbol detector known as Parallel Detection with Interference Estimation (PD-IE) is developed. It operates on the preprocessor output and takes the transformed receive vector \mathbf{y} , the channel matrix \mathbf{H} and the estimated sparsity matrix \mathbf{P} as inputs, as shown in Fig. 3.2. PD-IE has the following key features:

- It is a nonlinear detection algorithm, which offers better performance under overload than linear detection.
- It searches only over symbol subsets thereby reducing the complexity compared to optimum JMAP/ JML detectors, which search all possible symbol combinations.
- Parallel symbol estimators in the PD-IE detector allow fast processing for practical implementations.
- The integrated estimation process for residual CCI improves detection performance.

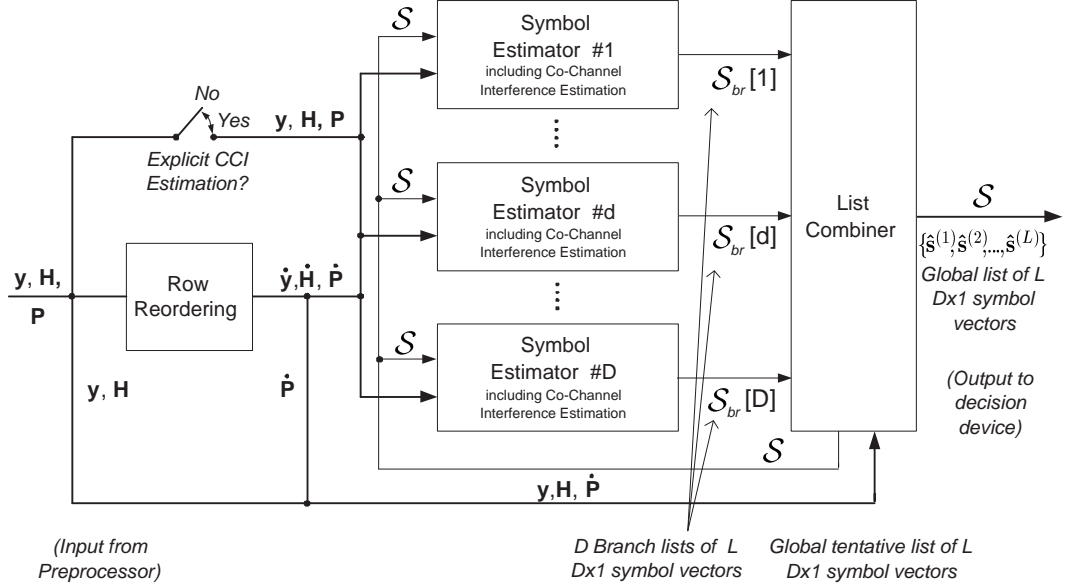


Figure 3.6 Block diagram of the PD-IE symbol detector.

- PD-IE considers two CCI estimation processes, *explicit CCI estimation* and *joint detection* of transmit symbols and residual CCI. The two processes allow conclusions concerning the optimum detector design.
- The detection algorithm works with arbitrary antenna array geometries. This is achieved by the PD-IE when using joint detection of transmit symbols and residual CCI.
- List processing and the output of an ordered list of likely symbol estimates make the PD-IE detector suitable for use with error control coding/ decoding, as it provides reliability information.

Fig. 3.6 provides a structural block diagram of the PD-IE detector. It uses Q overall iterations to compute and output an ordered global list of symbol vectors $\mathcal{S} = \{\hat{\mathbf{s}}^{(1)}, \hat{\mathbf{s}}^{(2)}, \dots, \hat{\mathbf{s}}^{(L)}\}$, where $\hat{\mathbf{s}}^{(l)} \in \mathcal{A}^D$ is the l th symbol vector in the list. The ordering is in terms of the Euclidean distance metric $\|\mathbf{y} - \mathbf{H}\hat{\mathbf{s}}^{(l)}\|$, which is chosen from the JML criterion of (3.6). The list \mathcal{S} is ordered from most to least likely. It is initialized with random symbol values and stored in the detector. In each iteration the list is updated

with improved symbol estimates and fed back to the parallel processing stages as shown in Fig. 3.6.

3.3.1 Branch Ordering

The rows of the detector inputs $\mathbf{y} \in \mathbb{C}^D$, $\mathbf{H} \in \mathbb{C}^{D \times D}$ and $\mathbf{P} \in \mathbb{N}_2^{D \times D}$ are first reordered, as indicated by the row reordering block in Fig. 3.6. Reordering of the input quantities improves performance in subsequent detection stages⁹ and is in terms of decreasing Strongest Energy to Interference Ratio (SEIR) (as defined below). The reordering can be described by the mapping operator

$$\begin{aligned} \mathbf{y}_{(D \times 1)} &\mapsto \dot{\mathbf{y}}_{(D \times 1)} \\ \mathbf{H}_{(D \times D)} &\mapsto \dot{\mathbf{H}}_{(D \times D)} \\ \mathbf{P}_{(D \times D)} &\mapsto \dot{\mathbf{P}}_{(D \times D)}, \end{aligned} \quad (3.11)$$

where the resulting output quantities $\dot{\mathbf{y}} \in \mathbb{C}^D$, $\dot{\mathbf{H}} \in \mathbb{C}^{D \times D}$ and $\dot{\mathbf{P}} \in \mathbb{N}_2^{D \times D}$ are permutations of the rows of the inputs.

The mapping of (3.11) is in order of the SEIR criterion. It is computed for each row of the matrix \mathbf{H} and is defined here as

$$SEIR[d] = \frac{E \left[\max_{1 \leq u \leq D} |h_{du} s_u|^2 \right]}{E \left[\sum_{v \in \bar{U}_e[d]} |h_{dv} s_v|^2 \right]} = \frac{\max_{1 \leq u \leq D} |h_{du}|^2}{\sum_{v \in \bar{U}_e[d]} |h_{dv}|^2}. \quad (3.12)$$

The numerator denotes the signal power of the strongest signal in the d th row $\mathbf{h}[d] \in \mathbf{H}$ and the denominator is the overall power of the signals outside the enumeration set $U_e[d]$. The reordering is in order of decreasing SEIR. In Figs. 3.3(c) and 3.3(d), the rows $\{1, 2, 3, 4, 5, 6\}$ of \mathbf{y} , \mathbf{H} and \mathbf{P} become rows $\{3, 5, 1, 2, 6, 4\}$ of $\dot{\mathbf{y}}$, $\dot{\mathbf{H}}$ and $\dot{\mathbf{P}}$, respectively.

⁹This is due to the employment of interference cancellation techniques in the PD-IE and will become evident later.

3.3.2 Symbol Estimation

The key to successful symbol detection in overloaded receivers is to correctly estimate and cancel residual CCI. PD-IE uses D parallel detection branches as shown in Fig. 3.6. Each branch corresponds to one received signal and performs CCI cancellation and symbol estimation. Fig. 3.7 shows two possible implementations of the symbol estimators. In Fig. 3.7(a), residual CCI is estimated explicitly using a trellis implementation. In contrast, Fig. 3.7(b) illustrates joint detection. The term “joint detection” is used because both the symbols and the residual CCI are jointly estimated using Parallel Interference Cancellation (PIC) techniques. Both implementations include identical high energy symbol estimators and take $\dot{\mathbf{y}}$, $\dot{\mathbf{H}}$, $\dot{\mathbf{P}}$ and the tentative global list \mathcal{S} as inputs. In addition, \mathbf{y} , \mathbf{H} and \mathbf{P} are needed for estimation of the residual CCI in Fig. 3.7(a). These are provided by the CCI estimation switch shown in Fig. 3.6. The switch is closed if PD-IE with explicit CCI estimation is used. In this case \mathbf{y} , \mathbf{H} and \mathbf{P} are input to the symbol estimators and are used in trellis construction and search¹⁰.

Each of the D symbol estimators outputs a branch list $\mathcal{S}_{br}[d] = \{\hat{\mathbf{s}}_{br}^{(1)}[d], \hat{\mathbf{s}}_{br}^{(2)}[d], \dots, \hat{\mathbf{s}}_{br}^{(L)}[d]\}$, where the L -members $\hat{\mathbf{s}}_{br}^{(k)}[d] \in \mathcal{A}^D$ are called branch symbol vectors. Each vector $\hat{\mathbf{s}}_{br}^{(k)}[d]$ contains estimates of the high and low energy symbol sets $\tau[d]$ and $\omega[d]$, respectively, and can be decomposed into

$$\hat{\mathbf{s}}_{br}^{(k)}[d] = \{\hat{\tau}^{(k)}[d], \hat{\omega}^{(k)}[d]\} \quad (3.13)$$

where $\hat{\omega}^{(k)}[d]$ and $\hat{\tau}^{(k)}[d]$ are the estimated low and high energy symbol sets¹¹ in the d th detection branch. The low energy sets $\hat{\omega}^{(k)}[d]$ are considered to be residual CCI. Symbol values for $\hat{\omega}^{(k)}[d]$ are obtained by an interference estimation process. The high energy sets $\hat{\tau}^{(k)}[d]$ are found by an exhaustive search over all possible $|\mathcal{A}|^{|\tau[d]|}$ symbol combinations $\tau[d]$, where $|\tau[d]| = |U_e[d]|$ is the number of signals in the d th enumeration set $U_e[d]$. This is done by the high energy symbol estimators shown in Fig. 3.7. Each such estimator takes the list $\widetilde{\mathcal{W}}[d] = \{\widetilde{\omega}^{(1)}[d], \widetilde{\omega}^{(2)}[d], \dots, \widetilde{\omega}^{(L_d)}[d]\}$ and the quantities

¹⁰Trellis construction and CCI estimation will be explained in detail later.

¹¹The symbol sets $\tau[d]$ and $\omega[d]$ for each branch list $\mathcal{S}_{br}[d]$ are derived from $\dot{\mathbf{p}}[d] \in \dot{\mathbf{P}}$.

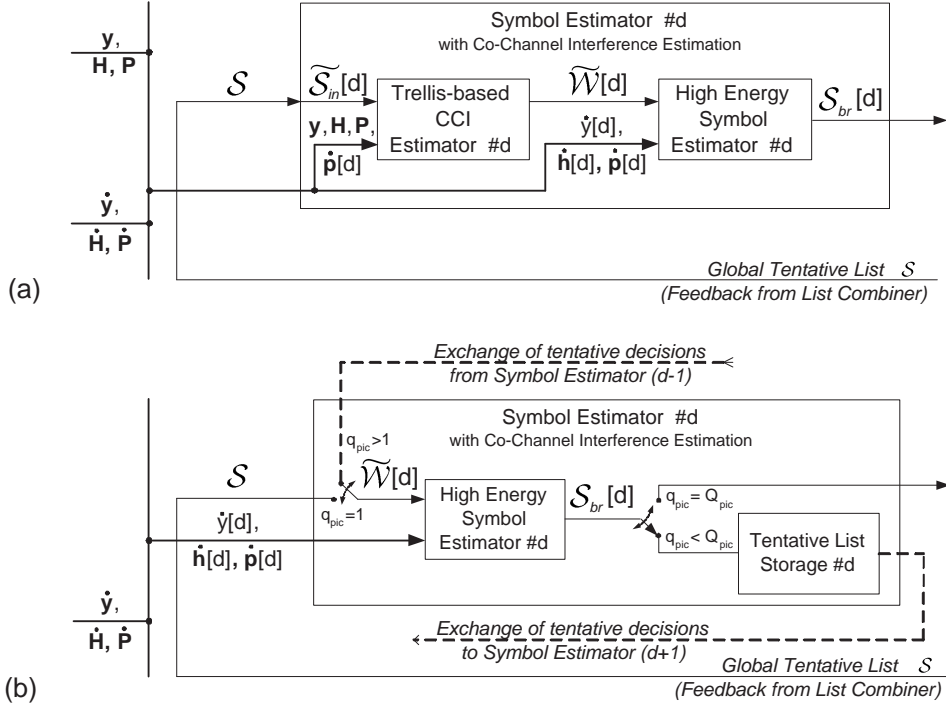


Figure 3.7 The d th symbol estimator in the PD-IE in Fig. 3.6 using (a) explicit CCI estimation and (b) joint detection.

$\hat{y}[d] \in \hat{\mathbf{y}}$, $\hat{\mathbf{h}}[d] \in \hat{\mathbf{H}}$ and $\hat{\mathbf{p}}[d] \in \hat{\mathbf{P}}$ as inputs. The list $\tilde{\mathcal{W}}[d]$ contains estimates of the residual CCI with the tilde notation $\tilde{(\cdot)}$ denoting non-redundant list elements¹². Storing only the non-redundant elements $\tilde{\omega}^{(i)}[d] \in \tilde{\mathcal{W}}$, $i = 1, 2, \dots, I_d$, ensures that the complexity of high energy symbol estimation is kept low. The list size I_d is maintained within the interval $1 \leq I_d \leq L$.

Next, the d th symbol estimator searches over all elements in the high energy symbol sets $\tau[d]$ and computes the Euclidean error metric for each element as

$$e^{(i,j)}[d] = \left| \hat{y}[d] - \hat{y}^{(i,j)}[d] \right|^2 \quad (3.14)$$

where $\hat{y}[d]$ is the d th component of $\hat{\mathbf{y}}$ and $\hat{y}^{(i,j)}[d]$ is the (i, j) th “candidate component” used as an approximation of $\hat{y}[d]$. Values for $\hat{y}^{(i,j)}[d]$ are computed as the sum of an

¹²The list $\tilde{\mathcal{W}}[d]$ is found by removing the symbols with high energy in $\hat{\mathbf{h}}[d] \in \hat{\mathbf{H}}$. As a result, there may then be redundant symbol sets which are removed from the list. This is done to keep the computational complexity low.

“enumeration component” $\hat{y}_e^{(j)}[d]$ and an “interference component” $\hat{y}_{if}^{(i)}[d]$ as

$$\begin{aligned}
 \hat{y}^{(i,j)}[d] &= \hat{y}_e^{(j)}[d] + \hat{y}_{if}^{(i)}[d] \\
 \hat{y}_e^{(j)}[d] &= \sum_{u \in U_e[d]} \dot{h}_{du} s_u \\
 \hat{y}_{if}^{(i)}[d] &= \sum_{u \in \bar{U}_e[d]} \dot{h}_{du} \hat{s}_u^{(i)}
 \end{aligned} \tag{3.15}$$

where \dot{h}_{du} is an element of $\dot{\mathbf{h}}[d] \in \dot{\mathbf{H}}$. The values of s_u for $\hat{y}_e^{(j)}[d]$ are drawn from the j th high energy symbol set $\tau^{(j)}[d]$ with $j = 1, 2, \dots, |\mathcal{A}|^{|\tau[d]|}$. The values of $\hat{s}_u^{(i)}$ in the interference component $\hat{y}_{if}^{(i)}[d]$ are estimates of the residual CCI, drawn from the i th list element $\tilde{\omega}^{(i)}[d] \in \tilde{W}[d]$ with $i = 1, 2, \dots, I_d$.

Finally, the vectors $\hat{\mathbf{s}}_{br}^{(k)}[d] \in \mathcal{S}_{br}[d]$ are found by choosing symbol values from the (i, j) symbol combination with the k th smallest error metric,

$$(i, j)^{(k)} = \arg \min_{\substack{1 \leq i \leq I_d \\ 1 \leq j \leq |\mathcal{A}|^{|\tau[d]|}}}^{(k)} \left\{ e^{(i,j)}[d] \right\}, \quad k = 1, 2, \dots, L \tag{3.16}$$

where $\min^{(k)}$ denotes the k th smallest value.

To illustrate estimation of the residual CCI, the following two examples are presented, one performing explicit CCI estimation and the other using the joint detection approach.

Symbol Estimation with explicit CCI Estimation

Consider a receiver with UCA antenna geometry resulting in a banded sparsity matrix \mathbf{P} as illustrated in Fig. 3.3(b). The d th CCI estimator in Fig. 3.7(a) has the inputs \mathbf{y} , \mathbf{H} , \mathbf{P} , $\dot{\mathbf{p}}[d] \in \dot{\mathbf{P}}$ and the global tentative symbol list¹³ \mathcal{S} . It employs the ITB-DDFSE algorithm of [22] to compute estimates of the residual CCI (as described later). A spatial trellis is first constructed from \mathbf{P} . Thereafter, the Viterbi algorithm is applied

¹³The list \mathcal{S} is initialized with random symbol values at the start of the PD-IE. It is later updated with improved estimates in each of the detector iterations.

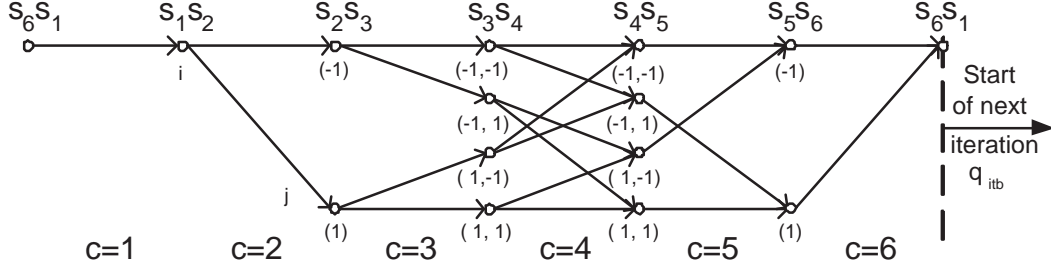


Figure 3.8 ITB-DDFSE trellis for explicit CCI estimation in symbol estimator #1 in Fig. 3.7(a). The trellis is shown for the UCA example in Figs. 3.3(a) and 3.3(b) using BPSK signals. It corresponds to matrix row $d = 1$.

to find the minimum cost path through the spatial trellis.

In order to minimize computational complexity, first create the list $\tilde{\mathcal{S}}_{in}[d]$ from \mathcal{S} in each receiver branch using the sparsity pattern $\dot{\mathbf{p}}[d] \in \dot{\mathbf{P}}$. This results in $\tilde{\mathcal{S}}_{in}[d] = \left\{ \tilde{\mathbf{s}}_{in}^{(1)}[d], \tilde{\mathbf{s}}_{in}^{(2)}[d], \dots, \tilde{\mathbf{s}}_{in}^{(K_d)}[d] \right\}$, where K_d is the list size with $1 \leq K_d \leq L$. Its elements $\tilde{\mathbf{s}}_{in}^{(k)}[d] \in \tilde{\mathcal{S}}_{in}[d]$ contain the non-redundant high energy symbol sets together with the best initial estimates of the residual CCI. Hence, the k th symbol vector in the d th list, $\tilde{\mathbf{s}}_{in}^{(k)}[d] \in \tilde{\mathcal{S}}_{in}[d]$, is decomposed into

$$\tilde{\mathbf{s}}_{in}^{(k)}[d] = \left\{ \tilde{\tau}_{in}^{(k)}[d], \hat{\omega}_{in}^{(k)}[d] \right\} \quad (3.17)$$

where $\tilde{\tau}_{in}^{(k)}[d]$ is the k th non-redundant high energy symbol set in $\tilde{\mathcal{S}}_{in}[d]$ and the corresponding low energy symbol set $\hat{\omega}_{in}^{(k)}[d]$ represents the best initial estimate of the residual CCI chosen from \mathcal{S} . The best initial estimate $\hat{\omega}_{in}^{(k)}[d]$ can easily be found from \mathcal{S} because the elements in \mathcal{S} are ordered from most to least likely. The list $\tilde{\mathcal{S}}_{in}[d]$ is input to the d th CCI estimator in Fig. 3.7(a). It operates on a spatial trellis having D stages indexed by $c = 1, 2, \dots, D$. The states at the c th trellis stage are denoted as $\sigma[c]$. The trellis starts and ends in a fixed state. Note that both fixed states contain the high energy symbol set $\tilde{\tau}_{in}^{(k)}[d]$ and are equivalent due to the tail-biting trellis structure. The trellis is applied to each of the K_d symbol vectors $\tilde{\mathbf{s}}_{in}^{(k)}[d] \in \tilde{\mathcal{S}}_{in}[d]$. It is used to compute improved estimates of the low energy symbols $\omega[d]$.

Fig. 3.8 illustrates an example trellis for the CCI estimator of Fig. 3.7(a) for the $M = 5$ antenna, $D = 6$ signal environment of Figs. 3.3(a) and 3.3(b). It is shown for

BPSK signaling. The extension to other signal types is straightforward and results in more trellis states. The states at the c th stage of the trellis are defined as

$$\sigma[c] = \{s_u | u \in U_e[c-1] \cap U_e[c]\} = \tau[c-1] \cap \tau[c], \quad c = 1, 2, \dots, D. \quad (3.18)$$

Note that for the chosen example the set $\tau[c=1] = \{s_6 s_1 s_2\}$ contains the high energy symbols. These are represented by fixed states in the trellis and initialized with the k th value $\tilde{\tau}_{in}^{(k)}[d]$. The corresponding low energy symbol sets $\hat{\omega}_{in}^{(k)}[d]$ are used as initial estimates of the residual CCI and are stored in the partial state estimate $\hat{\nu}[c]$. The trellis state sequence is $\sigma[1] = \{s_6 s_1\}$, $\sigma[2] = \{s_1 s_2\}$, $\sigma[3] = \{s_2 s_3\}$, $\sigma[4] = \{s_3 s_4\}$, $\sigma[5] = \{s_4 s_5\}$, $\sigma[6] = \{s_5 s_6\}$ and the number of symbols with variable state values is $\{\mu[c]\} = \{0, 0, 1, 2, 2, 1\}$, where $c = 1, 2, \dots, 6$ is the trellis stage index. The number of transitions from a previous state i into a new state j is denoted as $T_j[c]$. At the c th trellis stage, there are $j = |\mathcal{A}|^{\mu[c]}$ states and

$$T[c] = \sum_{j=1}^{|\mathcal{A}|^{\mu[c]}} T_j[c] \quad (3.19)$$

is the total number of transitions. In Fig. 3.8, the sequence of overall $i \rightarrow j$ transitions is $\{T[c]\} = \{1, 2, 4, 8, 4, 2\}$. The ITB-DDFSE algorithm of [22] is now employed. It finds the minimum cost path, according to a Euclidean distance error metric using the symbols from the current $i \rightarrow j$ transition and the partial state estimate $\hat{\nu}[c]$. After processing all transitions at the c th trellis stage, the surviving transitions are stored and the partial state estimate $\hat{\nu}[c]$ is updated. After typically $Q_{itb} = 2$ or 3 iterations around the tail-biting trellis, the estimate of the residual CCI, $\hat{\omega}^{(i)}[d]$, is found by tracing back the trellis path with the least cost. The non-redundant estimates, $\tilde{\omega}^{(i)}[d]$, are stored as the list $\tilde{\mathcal{W}}[d]$ which is output by the d th CCI estimator. This is illustrated in Fig. 3.7(a). The ITB-DDFSE algorithm of [22] is summarized in Table 3.2.

Table 3.2 Summary of the ITB-DDFSE algorithm of [22]

-
1. Define $\mu_{\max} = \max_{1 \leq c \leq D} \{\mu[c]\}$ and allocate an $|\mathcal{A}|^{\mu_{\max}} \times 1$ array of cumulative partial path metrics $\xi^{(i)}[c]$. Initialize $\xi^{(i)}[c=1] = 0, \forall i = 0, 1, \dots, |\mathcal{A}|^{\mu_{\max}} - 1$.
 2. Allocate a list of D arrays of size $|\mathcal{A}|^{\mu[c]} \times 1$ to store surviving transitions into the $\sigma[c+1] = j^{th}$ state at the c^{th} trellis stage, $i_s^{(j)}[c]$.
 3. For each iteration around the trellis, $q_{itb} = 1, 2, \dots, Q_{itb}$, and each value of (next state) $j = 0, 1, \dots, |\mathcal{A}|^{\mu[c+1]} - 1$ of each stage $c = 1, 2, \dots, D$
 - Find the survivor $i_s^{(j)}[c] = \arg \min_{i \in T_j} \{\xi^{(i)}[c] + e^{(i,j)}[c]\}$, where $i \in T_j$ denotes all valid $i \rightarrow j$ transitions and $e^{(i,j)}[c]$ is computed using (3.14).
 - Update the list of cumulative partial path metrics, $\xi^{(j)}[c+1] = \min_{i \in T_j} \{\xi^{(i)}[c] + e^{(i,j)}[c]\}$.
 - Update the partial state estimate $\hat{v}[c+1]$ by picking out symbol values from the surviving path.
 4. Choose a trellis state at the final stage with the least cumulative cost.
 5. Reconstruct the least cost path from the survivor list $i_s^{(j)}[c]$.
 6. Translate the states of the least cost path into a symbol sequence.
-

Symbol Estimation with Joint Detection

Now consider a receiver with ULA antenna geometry resulting in a non-banded sparsity matrix \mathbf{P} as shown in Fig. 3.3(b). In this case a spatial trellis cannot be easily formed and a more useful symbol estimator is that of Fig. 3.7(b). It uses an iterative PIC approach to jointly find estimates of the low and high energy symbol sets $\omega[d]$ and $\tau[d]$. The required inputs to the d th symbol estimator are the tentative global list \mathcal{S} and the d th row components of $\dot{y}[d] \in \dot{\mathbf{y}}$, $\dot{\mathbf{h}}[d] \in \dot{\mathbf{H}}$ and $\dot{\mathbf{p}}[d] \in \dot{\mathbf{P}}$.

The symbol estimators compute D tentative branch lists $\mathcal{S}_{br}[d]$ by searching over the high energy symbol sets $\tau[d]$ using (3.14) and (3.15). Each list $\mathcal{S}_{br}[d]$ serves as input to the $(d+1)$ th high energy symbol estimator in the $(q_{pic} + 1)$ th iteration. This is shown in Fig. 3.7(b). For $q_{pic} = 1$, the tentative global list \mathcal{S} is chosen as the input. From the input list to the d th symbol estimator, the list of estimates of the residual CCI, $\widetilde{\mathcal{W}}[d]$, is obtained using the sparsity pattern $\dot{\mathbf{p}}[d] \in \dot{\mathbf{P}}$. This is indicated in Fig. 3.7(b). The list elements for $\widetilde{\mathcal{W}}[d]$ are easily found by copying all symbol values that are represented by a 0 element in the sparsity pattern $\dot{\mathbf{p}}[d] \in \dot{\mathbf{P}}$. Redundant list elements are not stored

in $\widetilde{\mathcal{W}}[d]$ to keep the complexity low. After the Q_{pic} th iteration, the branch lists $\mathcal{S}_{br}[d]$ are output by the symbol estimators. Empirical trials have shown that using $Q_{pic} = 2$ to 5 iterations works well.

3.3.3 List Combining

The D branch lists $\mathcal{S}_{br}[d]$ are output by the symbol estimators and input to a list combiner (cf. Fig. 3.6). The symbols in each branch vector $\hat{\mathbf{s}}_{br}[d] \in \mathcal{S}_{br}[d]$ contain estimates of both the low and high energy symbol sets $\omega[d]$ and $\tau[d]$. The symbol estimators obtain an estimate of the symbols in the set $\omega[d]$ and perform an exhaustive search over the symbol values of the sets $\tau[d]$ only. This is in contrast to the JML detector in (3.6) which performs an exhaustive search over all possible symbol values. As a result, the symbol vector $\hat{\mathbf{s}}$ satisfying (3.6) may not be included in the D branch lists $\mathcal{S}_{br}[d]$. By searching and combining the branch lists, an improved list can be formed that has high probability of including the desired symbol vector $\hat{\mathbf{s}}$. This is done by the proposed list combining algorithm that finds the L -member tentative ordered global list \mathcal{S} of most likely symbol estimate vectors $\hat{\mathbf{s}}^{(l)} \in \mathcal{S}$, $l = 1, 2, \dots, L$. The list combiner is shown in Fig. 3.6. It takes \mathbf{y} , \mathbf{H} , $\dot{\mathbf{P}}$ and the D branch lists $\mathcal{S}_{br}[d]$ as inputs and outputs \mathcal{S} . The list combiner also stores the tentative global list \mathcal{S} and a list of corresponding error metrics $\mathcal{E} = \{e^{(1)}, e^{(2)}, \dots, e^{(L)}\}$. Both lists \mathcal{S} and \mathcal{E} are updated in each of the Q global PD-IE iterations.

At the beginning of the PD-IE algorithm, the list \mathcal{S} is initialized with random symbol values. The corresponding error metrics $e^{(l)} \in \mathcal{E}$ are computed from \mathcal{S} as

$$e^{(l)} = \left\| \mathbf{y} - \mathbf{H}\hat{\mathbf{s}}^{(l)} \right\|^2, \quad l = 1, 2, \dots, L. \quad (3.20)$$

The two lists \mathcal{S} and \mathcal{E} are then reordered according to an increasing error metric.

In the q th detector iteration ($q = 1, 2, \dots, Q$) the list \mathcal{S} is updated with improved symbol estimates. The improved list \mathcal{S} is then fed back to the D detector branches to further improve the symbol estimates. The iteration parameter Q is arbitrarily set so

Table 3.3 Iterative list combining algorithm

Initial Update	
1.	Define a list of length D branch symbol vectors, $\tilde{\mathcal{S}}_{br}$. Initialize the elements $\tilde{\mathbf{s}}_{br}^{(k)} \in \tilde{\mathcal{S}}_{br}$ with the non-redundant symbol vectors from the D branch lists $\mathcal{S}_{br}[d]$. Note that $k = 1, 2, \dots, K$ and the list size K is in the range $1 \leq K \leq LD$.
2.	The list of error metrics corresponding to $\tilde{\mathcal{S}}_{br}$ is defined as $\mathcal{E}_{br} = \{e_{br}^{(1)}, e_{br}^{(2)}, \dots, e_{br}^{(K)}\}$. Compute each $e_{br}^{(k)} \in \mathcal{E}_{br}$ as $e_{br}^{(k)} = \ \mathbf{y} - \mathbf{H}\tilde{\mathbf{s}}_{br}^{(k)}\ ^2$, where $\tilde{\mathbf{s}}_{br}^{(k)} \in \tilde{\mathcal{S}}_{br}$.
3.	Define the list of L tentative minimum error metrics, \mathcal{E}_{min} , and the corresponding list of $D \times 1$ symbol vectors, \mathcal{S}_{min} . Obtain the elements $e_{min}^{(l)} \in \mathcal{E}_{min}$ by searching $e_{min}^{(l)} = \min_{\substack{1 \leq i \leq L \\ 1 \leq k \leq K}}^{(l)} \{e_{br}^{(k)}, e^{(i)}\}, \quad l = 1, 2, \dots, L$ where $e^{(i)}$ is the i th element in \mathcal{E} , obtained in the $(q-1)$ th iteration. For $q = 1$, choose $e^{(i)} = \infty$ for all list elements $e^{(i)} \in \mathcal{E}$. Find the elements $\tilde{\mathbf{s}}_{min}^{(l)} \in \mathcal{S}_{min}$ by choosing symbol values from the corresponding lists $\tilde{\mathcal{S}}_{br}$ and \mathcal{S} .
4.	Set $\mathcal{S} = \mathcal{S}_{min}$ and $\mathcal{E} = \mathcal{E}_{min}$.
Iterative Search	
5.	Define the D lists $\tilde{\mathcal{T}}[d]$ ($d = 1, 2, \dots, D$). Find the elements $\tilde{\tau}^{(j)}[d] \in \tilde{\mathcal{T}}[d]$ by using $\dot{\mathbf{p}}[d] \in \mathbf{P}$ to select the non-redundant high energy symbol sets from $\mathcal{S}_{br}[d]$. Note that $j = 1, 2, \dots, J_d$ and the list size J_d is in the range $1 \leq J_d \leq L$.
6.	Define the lists $\tilde{\mathcal{S}}_{cand} = \{\tilde{\mathbf{s}}_{cand}^{(1)}, \tilde{\mathbf{s}}_{cand}^{(2)}, \dots, \tilde{\mathbf{s}}_{cand}^{(L)}\}$ and $\mathcal{E}_{cand} = \{e_{cand}^{(1)}, e_{cand}^{(2)}, \dots, e_{cand}^{(L)}\}$. These store $D \times 1$ candidate symbol vectors and corresponding error metrics.
7.	For each iteration $q_{lc} = 1, 2, \dots, Q_{lc}$, and all $j = 1, 2, \dots, J_d$ elements $\tilde{\tau}^{(j)}[d] \in \tilde{\mathcal{T}}[d]$ of the $d = 1, 2, \dots, D$ lists, $\tilde{\mathcal{T}}[d]$, <ul style="list-style-type: none"> • Use $\dot{\mathbf{p}}[d] \in \dot{\mathbf{P}}$ to find the estimates of the low energy symbol sets $\omega[d]$ in the list \mathcal{S} and copy the non-redundant symbol sets $\tilde{\omega}^{(l)}[d]$ from \mathcal{S} into $\tilde{\mathcal{S}}_{cand}$. The resulting list $\tilde{\mathcal{S}}_{cand}$ has size L_d with $1 \leq L_d \leq L$. • For each element $\tilde{\mathbf{s}}_{cand}^{(k)} \in \tilde{\mathcal{S}}_{cand}$, $k = 1, 2, \dots, L_d$, do <ul style="list-style-type: none"> – Copy the high energy symbol set estimate $\tilde{\tau}^{(j)}[d]$ into $\tilde{\mathbf{s}}_{cand}^{(k)}$. – Compute the error metric, $e_{cand}^{(k)} = \ \mathbf{y} - \mathbf{H}\tilde{\mathbf{s}}_{cand}^{(k)}\ ^2$. • Update the tentative list \mathcal{E}_{min} by finding the l smallest metrics, $e_{min}^{(l)} = \min_{\substack{1 \leq i \leq L \\ 1 \leq k \leq L_d}}^{(l)} \{e_{cand}^{(k)}, e^{(i)}\}, \quad l = 1, 2, \dots, L$ where $e^{(i)} \in \mathcal{E}$ is the ith element in \mathcal{E}. Update the corresponding list \mathcal{S}_{min} by choosing the $l = 1, 2, \dots, L$ symbol vectors from $\tilde{\mathcal{S}}_{cand}$ and \mathcal{S} with minimum error metric $e_{min}^{(l)}$. • Set $\mathcal{S} = \mathcal{S}_{min}$ and $\mathcal{E} = \mathcal{E}_{min}$.
8.	Terminate the list combining algorithm. Set $q = q + 1$.

that further iterations produce negligible improvement. If $q = Q$, \mathcal{S} is output by the detector as an estimate of the ordered list of most likely symbol vectors. Typically, only $Q = 2$ or 3 iterations are necessary. A decision device then selects the first element $\hat{\mathbf{s}}^{(1)} \in \mathcal{S}$ as the best estimate of the D transmitted symbols. Alternatively, \mathcal{S} can be used to provide soft information to subsequent receiver stages such as error control decoders.

List combining is done in two stages: initial update and iterative search over the estimates of the high energy symbol sets $\tau[d]$. In the initial update, the stored lists \mathcal{S} and \mathcal{E} are updated with the symbol vectors and error metrics obtained in the current iteration. The iterative search combines the estimates of the high energy symbol sets $\tau[d]$ with the symbols stored in \mathcal{S} . This typically requires $Q_{lc} = 2$ or 3 iterations. The algorithm uses dynamic programming principles¹⁴ and is summarized in Table 3.3.

3.4 PERFORMANCE

A performance analysis of PD-IE is difficult to obtain due to both the iterative and list reduction processes. Therefore, Monte Carlo simulation is used to determine performance and to compare it with other detectors under overload. Results are obtained for the two cases where either perfect or imperfect CSI is available to the receiver. In simulations, equal power symbol synchronous QPSK (4-QAM) signals are assumed to be sent from D transmit antennas. The signals are incident on a receiver with an M -element UCA or ULA where $D > M$. In order to measure the error performance, the Symbol Error Rate (SER) of the worst performing signal is used as a measurement unit. Simulations were stopped after the detector had made 50 symbol errors for at least one of the D transmitted signals.

¹⁴The sizes of the internal lists vary during the iterative combining process. This is due to the removal of redundant information in the lists and requires dynamic memory allocation.

3.4.1 Perfect Channel State Information

If perfect CSI is assumed at the receiver, the channel estimator in Fig. 3.2 is error free and correctly estimates the matrix \mathbf{A} in (3.1). This is the ideal case which, in practice, is only achieved by a genie-added channel estimator. Although not realistic, simulations with perfect CSI show the best achievable performance and provide insights into the behavior of the algorithm as a function of the various parameters.

UCA

Fig. 3.9 shows the relative performance of the proposed PD-IE algorithm, the SRSJD approach of [22] and JML detection [13] at SNR $\Gamma = 10dB$. The receiver employs a $M = 5$ -element UCA front end with radius $R = 0.2\lambda$. It is assumed that all impinging signals have the same phase reference. At the preprocessing stage of the detector, the linear beamformer of (3.5) is used as a spatial filter. The SEAIR and SSSER thresholds for derivation of the sparsity matrix \mathbf{P} are empirically set to $T_1 = 2$ and $T_2 = 0.1$, respectively, for up to 100% overload ($f(D, M) \leq 2$). For higher overload factors ($f(D, M) > 2$), the thresholds are set to $T_1 = 2$ and $T_2 = 0.5$, respectively. As a result, in this example, each row of the channel matrix \mathbf{H} contains $|\tau[d]| = 3$ high energy symbols $\tau[d]$. The matrix \mathbf{P} is used for both the PD-IE and SRSJD algorithms. SRSJD performs two iterations around the tail-biting trellis as suggested in [22]. Simulations using more iterations achieved only marginal performance improvements for the resulting increase in SRSJD complexity.

The choices of the PD-IE parameters are shown in Table 3.4. The PD-IE symbol estimators use either explicit CCI estimation or joint detection as described earlier. The iteration parameter Q_{itb} is set to $Q_{itb} = 2$ and Q_{pic} is adjusted so that both approaches have similar complexity. Complexity values are presented in Table 3.4 as the number of real squaring operations per output symbol vector.

From Fig. 3.9 it can be seen that the SER essentially increases with the number of signals D . This is due to the residual CCI in the filtered received signal which increases with the load factor $f(D, M)$. The somewhat better performance for odd numbers of

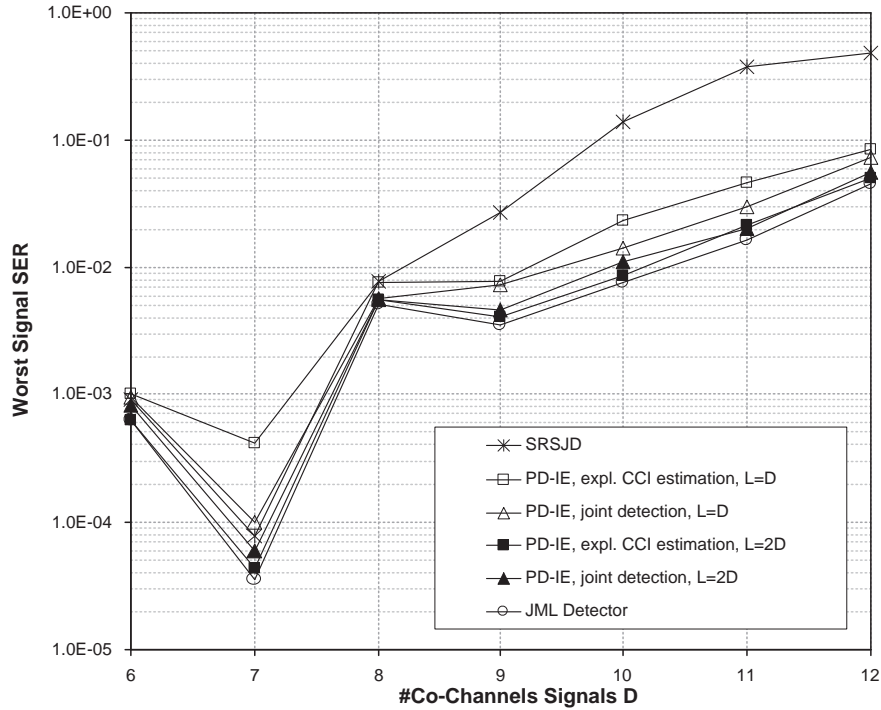


Figure 3.9 SER of the signal with worst performance versus the number of co-channel signals at SNR, $\Gamma = 10dB$ for a $M = 5$ -element UCA using JML, SRSJD and PD-IE algorithms. Iteration parameters for PD-IE are shown in Table 3.4.

Table 3.4 Iteration parameters and computational complexity for PD-IE simulations in Fig. 3.9 and Fig. 3.10 using an $M = 5$ -element UCA.

Signals D	Size of \mathcal{S} , $L = D$			Size of \mathcal{S} , $L = 2D$		
	$Q_{lc} = Q = 2$		Complexity	$Q_{lc} = Q = 2$		Complexity
	Q_{itb}	Q_{pic}		Q_{itb}	Q_{pic}	
6	2	3	$\sim 2.5E4$	2	3	$\sim 4.2E4$
7	2	3	$\sim 4.0E4$	2	4	$\sim 8.1E4$
8	2	4	$\sim 6.6E4$	2	5	$\sim 1.4E5$
9	2	4	$\sim 1.0E5$	2	5	$\sim 2.2E5$
10	2	5	$\sim 1.5E5$	2	6	$\sim 3.4E5$
11	2	5	$\sim 2.0E5$	2	6	$\sim 4.8E5$
12	2	6	$\sim 2.8E5$	2	7	$\sim 6.8E5$

co-channel signals, e.g. $D = 7, 9$, is an artifact of the UCA geometry, as in these cases there are no signals received from opposite AOAs. Note that the AOA dependence of the UCA is not observed if the error performance is dominated by the residual CCI. This occurs under heavier overload (e.g. $D = 11$ as shown in Fig. 3.9).

JML is the optimum detector and achieves the lowest SER in all cases. SRSJD approximates JML up to $D = 8$ signals. Its performance degrades for $D > 8$. PD-IE outperforms SRSJD at the cost of higher complexity and achieves near JML performance when using a global list \mathcal{S} of size $L = 2D$. For $L = D$, performance is impaired due to the increased probability of the transmitted symbols not being in the list \mathcal{S} . At a similar complexity, symbol estimation with explicit CCI estimation slightly outperforms joint detection in PD-IE for $L = 2D$, but performance is worse for $L = D$. This arises because the trellis-based CCI estimation process can outperform the PIC technique if the correct high energy symbols are already contained in the global list \mathcal{S} . In contrast, joint detection is able to better estimate the CCI for smaller list sizes L because it jointly estimates both the CCI and the high energy symbol sets.

Fig. 3.10 illustrates SER versus SNR performance for PD-IE using the same receiver setup as in Fig. 3.9. Results are shown for $D = 8, 10$ and 12 signals (Figs. 3.10(a), 3.10(b) and 3.10(c)). Two PD-IE implementations are considered. The first employs symbol estimators with explicit CCI estimation whereas the other uses joint detection of high energy symbol sets and CCI. The SER values in Fig. 3.10 decrease with increasing SNR. In most cases an error floor is shown at high SNR. Its value is determined by the load factor $f(D, M)$ and the PD-IE configuration. In general, the error floor is lower at smaller load factors because the residual CCI level is lower. This is evident in Figs. 3.10(a) to (c).

The minimum value of the error floor in PD-IE is further influenced by the probability of the correct symbol values not being included in the branch lists $\mathcal{S}_{br}[d]$. This explains the higher error floor for the smaller list size of $L = D$ in contrast to $L = 2D$. Increasing L reduces the error floor because more symbol combinations are considered as candidates. This of course increases PD-IE complexity. At low SNR ($\Gamma < 10dB$),

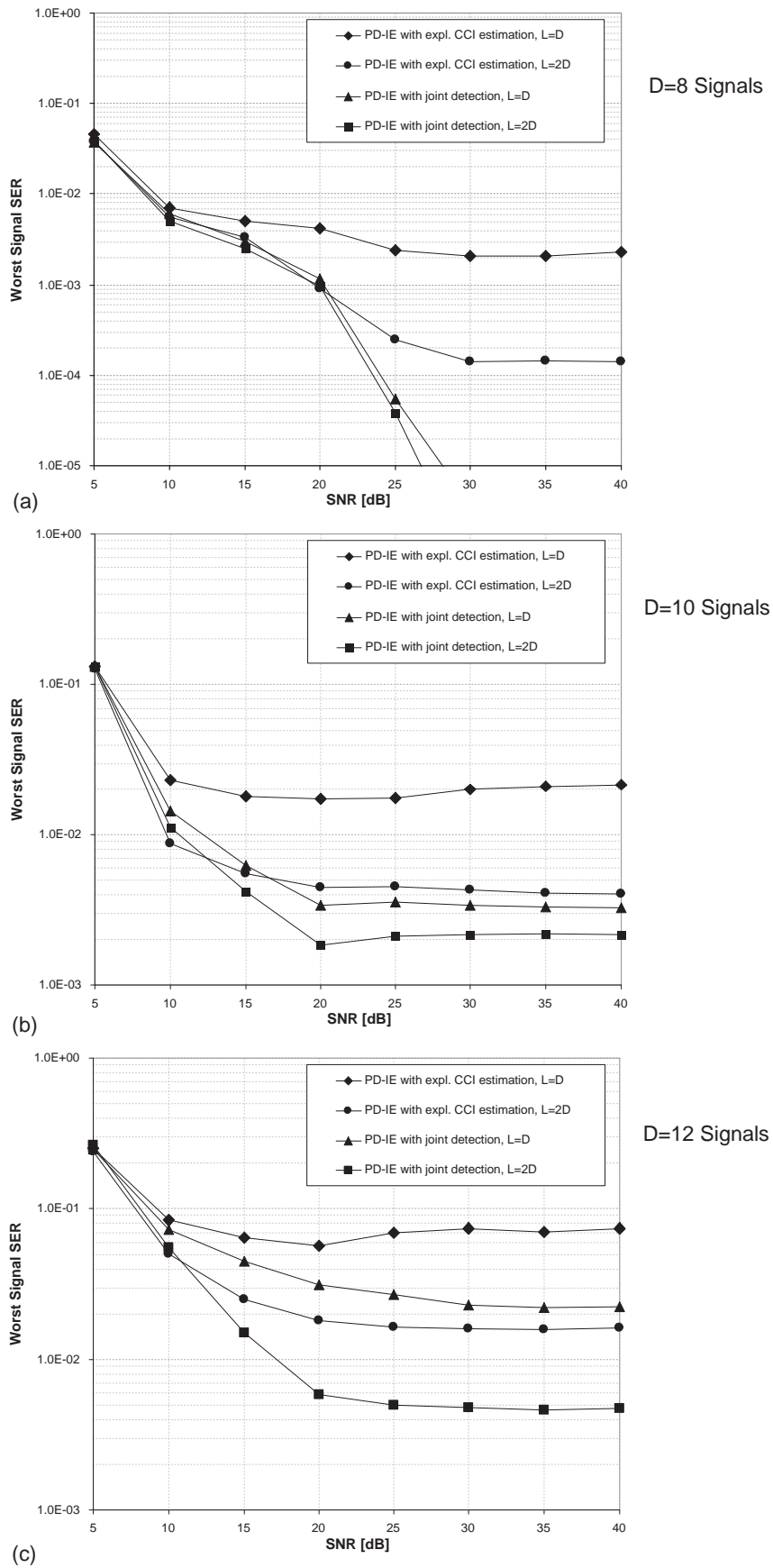


Figure 3.10 SER of the signal with worst performance versus SNR for PD-IE with list sizes $L = D$ and $2D$ using a $M = 5$ -element UCA with (a) $D = 8$, (b) $D = 10$ and (c) $D = 12$ signals. The iteration parameters are set to give comparable complexity for PD-IE with explicit CCI estimation and PD-IE with joint detection as shown in Table 3.4.

the performance results are similar for both PD-IE symbol estimator implementations whereas at higher SNR ($\Gamma \geq 15dB$), joint detection clearly outperforms explicit CCI estimation in PD-IE. This is most obvious in Fig. 3.10(a) and can be explained by the different symbol estimation processes considered. Since PD-IE with explicit CCI estimation relies on correct estimates of the residual CCI, its error performance is sensitive to CCI estimation errors. These are more likely to occur if the global list \mathcal{S} contains only erroneous symbols and the list size L is small. The explicit CCI estimation process has too few degrees of freedom and cannot accurately estimate all the CCI. There will then always be significant residual CCI. In contrast, PD-IE with joint detection re-estimates both the residual CCI and the high energy symbol values during the iterative PIC process. It has more degrees of freedom and thus higher probability of finding the correct symbol estimates even if the list \mathcal{S} is small or initially contains only erroneous estimates. Increasing the size of \mathcal{S} from $L = D$ to $2D$ reduces the superiority of joint detection in the PD-IE due to better explicit CCI estimation. This is clearly observed in Figs. 3.10(b) and 3.10(c).

ULA

Fig. 3.11 depicts SER versus SNR curves for a receiver with an $M = 6$ -element ULA with element spacing $B = 3\lambda$. The transmitters are randomly allocated to D equal size sectors¹⁵ within the array's view angle of $\theta_{\max} = \pm 60^\circ$. The transmitted signals are incident with random phase on the antenna array. At the preprocessor, MRC is employed as the diversity combining technique. The SEAIR and SSSER thresholds to obtain the sparsity matrix \mathbf{P} are set to $T_1 = 2$ and $T_2 = 0.1$, respectively. The detection algorithm is PD-IE with joint detection of high energy symbol sets and residual CCI. The iterative PIC process uses either $Q_{pic} = 1$ or $Q_{pic} = 5$ iterations. The global list \mathcal{S} has size $L = 2D$. Results are shown for $D = 9$ and 12 signals (load factor $f(D, M) = 1.5$ and 2). All other parameters remain unchanged.

¹⁵For non-fading memoryless channels, the ULA is highly selective in AOA. Therefore, random spacing of the transmitters into equal size sectors is used to obtain comparable results for different numbers of co-channel signals.

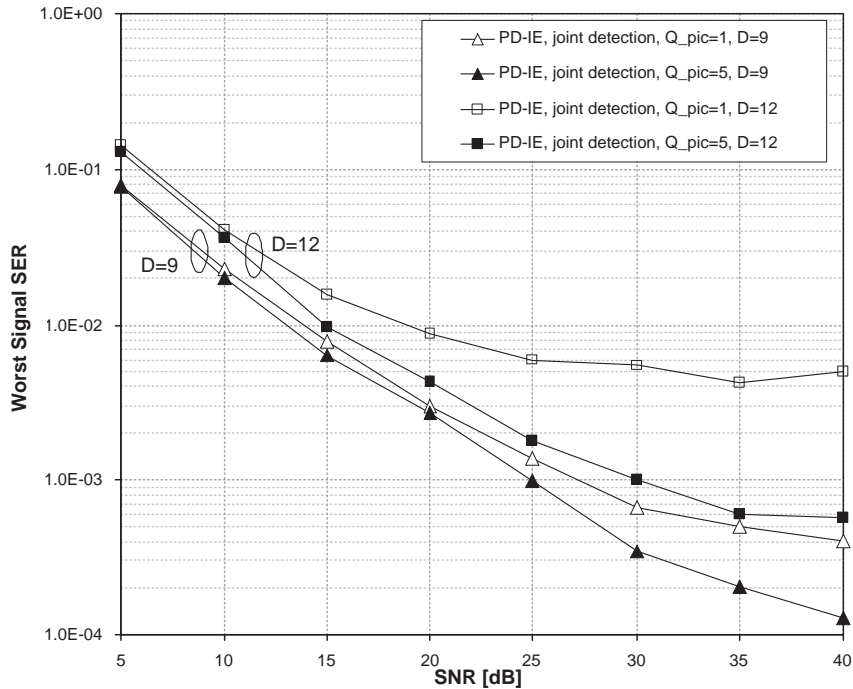


Figure 3.11 SER of the signal with worst performance versus SNR for PD-IE using an $M = 6$ -element ULA with element spacing $B = 3\lambda$. There are $D = 9$ and 12 co-channel signals. The size of the global list \mathcal{S} is $L = 2D$.

It can be seen in Fig. 3.11 that increasing the number of iterations, Q_{pic} , significantly improves detection performance for $D = 12$ signals. In contrast, performance improvements are much smaller for $D = 9$ signals as Q_{pic} increases. This is expected because increasing Q_{pic} yields more accurate estimation of the residual CCI which is more important at higher levels of overload. Furthermore, it is evident that more iterations (increased Q_{pic}) yield a lower error floor as the SNR increases. Better CCI estimation comes at the cost of increased complexity.

3.4.2 Imperfect Channel State Information

In a practical receiver, the channel estimator in Fig. 3.2 does not output the correct array response matrix \mathbf{A} in (3.1). Instead, it outputs an estimate of \mathbf{A} which includes an estimation error. Actual estimation of the CSI is beyond the scope of this thesis. Therefore, only the effects of random estimation errors are considered. The imperfect

CSI is modelled as [45]

$$\hat{a} = \eta a + \sqrt{1 - \eta^2} \epsilon, \quad (3.21)$$

where a is the actual CSI, ϵ is an independent zero-mean complex Gaussian random variable with variance $\sigma_\epsilon^2 = 1/2$ per dimension and η is the power correlation coefficient between a^2 and \hat{a}^2 . This model is used so that the estimated CSI has the same variance as the actual CSI. The added estimation noise energy is evaluated as $\frac{1-\eta^2}{\eta^2} \times 100\%$ with respect to the actual CSI energy. Note that the coefficient η approaches 1 with increasing SNR [46]. In this case, $\eta = 1$ and it follows $\hat{a} = a$ meaning perfect CSI is available. Using fixed η -values provides the worst-case performance and usually results in an error floor at high SNR.

$$\text{Denoting } \hat{\mathbf{A}} = \begin{pmatrix} \hat{a}_{11} & \hat{a}_{12} & \dots & \hat{a}_{1D} \\ \hat{a}_{21} & \hat{a}_{22} & \ddots & \hat{a}_{2D} \\ \vdots & \vdots & \ddots & \vdots \\ \hat{a}_{M1} & \hat{a}_{M2} & \dots & \hat{a}_{MD} \end{pmatrix} \text{ and } \mathbf{E} = \begin{pmatrix} \epsilon_{11} & \epsilon_{12} & \dots & \epsilon_{1D} \\ \epsilon_{21} & \epsilon_{22} & \ddots & \epsilon_{2D} \\ \vdots & \vdots & \ddots & \vdots \\ \epsilon_{M1} & \epsilon_{M2} & \dots & \epsilon_{MD} \end{pmatrix}$$

allows the output of the channel estimator with imperfect CSI in matrix form to be written as

$$\hat{\mathbf{A}} = \eta \mathbf{A} + \sqrt{1 - \eta^2} \mathbf{E}, \quad (3.22)$$

where $\hat{\mathbf{A}} \in \mathbb{C}^{M \times D}$ is the imperfect CSI output matrix, $\mathbf{A} \in \mathbb{C}^{M \times D}$ is the actual CSI and $\mathbf{E} \in \mathbb{C}^{M \times D}$ is the matrix of independent and identically distributed (i.i.d.) complex Gaussian random variables. For the case of imperfect CSI, the preprocessor in Fig. 3.2 computes \mathbf{H} from $\hat{\mathbf{A}}$ (instead of \mathbf{A}). This impacts the sparsity matrix \mathbf{P} which is derived from \mathbf{H} . For example, if imperfect CSI is considered with the configuration used in Figs. 3.3(a) and 3.3(b) (UCA at the receiver front-end and equal energy signals from transmitters equally spaced in AOA), the matrix \mathbf{P} is not guaranteed to have a diagonally-banded structure. This means that the simple spatial trellis required for PD-IE with explicit CCI estimation cannot be formed. Consequently, only PD-IE with joint detection and JML detection are considered here.

Fig. 3.12 depicts SER curves for the same configuration as used in Fig. 3.9. The

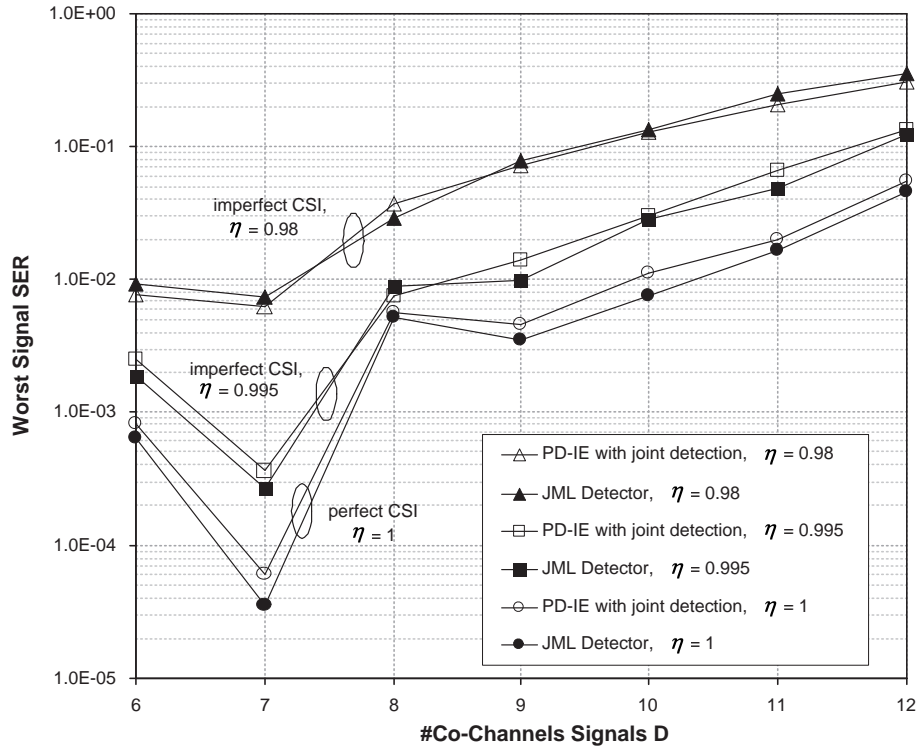


Figure 3.12 SER of the signal with worst performance versus number of co-channel signals at SNR, $\Gamma = 10dB$ with perfect and imperfect CSI. The power correlation coefficient is set to $\eta = 0.98, 0.995$ and 1 (perfect CSI). The receiver setup and detection parameters are the same as in Fig. 3.9.

power correlation coefficient η is set to $\eta = 0.98, 0.995$ and 1 (perfect CSI). This is equivalent to an average estimation error energy of 4.1%, 1% and 0% of the actual CSI, respectively. The list size for PD-IE is $L = 2D$. It is clear that with imperfect CSI the performance of both JML and PD-IE degrades. At the chosen SNR of $\Gamma = 10dB$ the SER penalty for JML and PD-IE algorithms is approximately one order of magnitude at $\eta = 0.98$ and a factor of three at $\eta = 0.995$. This appears independent of the number of co-channel signals over a wide range of D . Also note, that the performance advantage for odd signal numbers ($D = 7, 9$) is less pronounced the smaller η is.

In Fig. 3.13, the SER is shown for $D = 6$ and 10 signals for the cases of perfect and imperfect CSI. The receiver setup and the detection parameters remain the same as in Fig. 3.9. It is clear that the case of perfect CSI ($\eta = 1$) achieves the best performance, whereas for smaller values of η the SER increases and an error floor occurs. The error floor increases with decreasing η . Hence, an accurate CSI estimation process is crucial

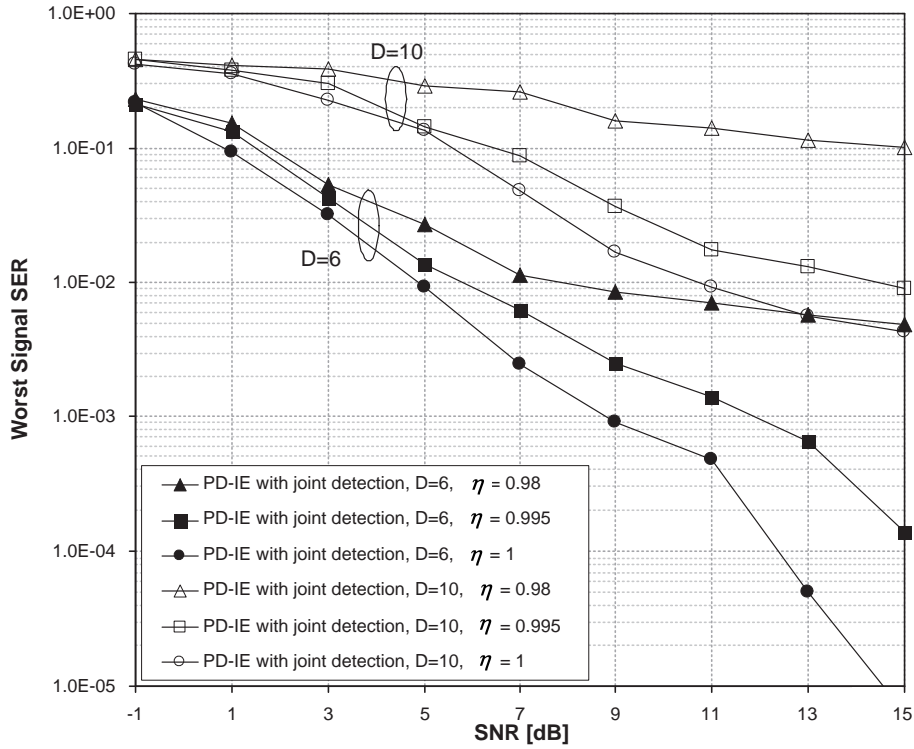


Figure 3.13 SER of the signal with worst performance versus the SNR with perfect and imperfect CSI. The power correlation coefficient is set to $\eta = 0.98, 0.995$ and 1 (perfect CSI). The receiver setup and detection parameters are the same as in Fig. 3.9. Results are shown for $D = 6$ and 10 signals.

for good error performance if the receiver operates under overloaded. This is most important when the receiver load factor $f(D, M)$ is higher, because higher load tends to increase the error floor¹⁶.

3.5 COMPLEXITY

The computational complexity of PD-IE is now considered. It is determined here in terms of the number of real squaring operations in the calculation of the Euclidean error metrics. This is usually the most hardware intensive operation [10, 17, 22].

PD-IE complexity depends on many parameters. Among these are the number of signals D , the alphabet size $|\mathcal{A}|$, the number of high energy symbols $|\tau[d]|$, the number of iterations Q_{itb} or Q_{pic} , Q_{lc} and Q , and the sizes of the lists $\mathcal{S}_{br}[d]$ and \mathcal{S} .

¹⁶This was observed in Fig. 3.10.

The overall complexity of PD-IE, denoted here as C , can be expressed as the sum of the complexities of the symbol estimator and the list combiner namely, C_{se} and C_{lc} , respectively. This must be done for each of the Q overall iterations. Analyzing the block diagram in Fig. 3.6, C can be calculated as

$$C = 2 \sum_{q=1}^Q (C_{se} + C_{lc}) \quad (3.23)$$

where $C_{se} = \sum_{d=1}^D C_{se}[d]$ is the sum of the individual symbol estimator complexities, $C_{se}[d]$. Note that the scaling factor of two is introduced because computation of each Euclidean error metric requires two real squarings. The complexity C_{se} depends on the type of symbol estimator used in PD-IE. If PD-IE with explicit CCI estimation is used, $C_{se}[d]$ is denoted as $C_{se}^{(itb)}[d]$. The superscript (*itb*) refers to the ITB-DDFSE algorithm, which is used to estimate residual CCI. Similarly for PD-IE with joint detection, $C_{se}[d]$ is denoted as $C_{se}^{(pic)}[d]$, where the superscript (*pic*) refers to the internal iterative PIC process. Both PD-IE versions contain a high energy symbol estimator in each branch. It searches over all possible values of the symbols in the high energy symbol sets $\tau[d]$. This complexity is denoted as $C_\tau[d]$ and is computed as $C_\tau[d] = I_d |\mathcal{A}|^{|\tau[d]|}$. The variable I_d denotes the size of the input list $\widetilde{\mathcal{W}}[d]$ (cf. Fig. 3.7(a) and Fig. 3.7(b)). For PD-IE with explicit CCI estimation based on a trellis (Fig. 3.7(a)), $C_{se}^{(itb)}[d]$ may be written as

$$C_{se}^{(itb)}[d] = C_{itb}[d] + C_\tau[d], \quad (3.24)$$

where $C_{itb}[d] = K_d Q_{itb} \sum_{c=1}^D T[c]$ is the complexity of the d th CCI estimator. The variables K_d and $T[c]$ denote the size of the input list $\widetilde{\mathcal{S}}_m[d]$ and the number of transitions at the c th trellis stage defined in (3.19), respectively.

For PD-IE with joint detection using the iterative PIC technique (Fig. 3.7(b)), $C_{se}[d]$ is derived as

$$C_{se}^{(pic)}[d] = Q_{pic} C_\tau[d]. \quad (3.25)$$

Table 3.5 Comparison of computational complexity for a receiver with $M = 8$ -element UCA front-end

Signals D	JML C	SRSJD		PD-IE			
		$\mu[d]$	C	expl. CCI estimation		joint detection	
				C_{se}/C_{lc}	C	C_{se}/C_{lc}	C
9	4.2E06	2	2.3E03	1.2	3.0E5	3.1	1.4E5
10	1.7E07	2	2.6E03	1.3	5.2E5	2.6	1.8E5
11	6.7E07	2	2.8E03	2.7	1.2E6	1.9	2.5E5
12	2.7E08	4	4.9E04	2.8	1.8E6	1.5	3.3E5
13	1.1E09	4	5.3E04	2.7	2.5E6	1.3	4.2E5
14	4.3E09	4	5.7E04	6.4	7.2E6	1.1	5.2E5
15	1.7E10	4	6.1E04	16.7	2.2E7	0.8	7.1E5

The complexity of the list combining algorithm (Table 3.3) is given by

$$C_{lc} = D \left[K + \sum_{q_{lc}=1}^{Q_{lc}} \left(\sum_{d=1}^D J_d L_d \right) \right] \quad (3.26)$$

where J_d , K and L_d are the sizes of the lists $\tilde{\mathcal{T}}[d]$, $\tilde{\mathcal{S}}_{br}$, and $\tilde{\mathcal{S}}_{cand}$, respectively. Note that K and J_d may vary in each of the Q global iterations, whereas L_d may change in each of the Q_{lc} list combining iterations.

In Table 3.5, complexity of the JML [17], SRSJD [22] and PD-IE algorithms is compared for receivers with an $M = 8$ -element UCA. The array radius is $R = \lambda/4$ and the linear beamformer of (3.5) is used as a preprocessor. JML requires $2M|\mathcal{A}|^D$ while SRSJD needs only $2Q_{itb}D|\mathcal{A}|^{(\mu[c]+1)}$ real squarings [22]. Complexity values for PD-IE are shown for $|\tau[d]| = 3$ high energy symbols, obtained through adjusting the SEAIR and SSSER thresholds. The global list \mathcal{S} has size $L = 2D$. Finally, the iteration parameters are set to $Q_{itb} = Q_{lc} = Q = 2$ for PD-IE with explicit CCI estimation and $Q_{pic} = 3$, $Q_{lc} = Q = 2$ for PD-IE with joint detection. Both the list size and the iteration parameters were chosen empirically to achieve good detection performance at low complexity. In general, these parameters provide a complexity-performance tradeoff and their values may thus be chosen according to practical restrictions and requirements.

The results of Table 3.5 clearly show that JML has extremely high complexity, increasing exponentially with the number of signals D . SRSJD achieves the lowest complexity. It has a linear increase within subsets for which $\mu[d]$ is constant and increases exponentially with the subset size. PD-IE provides complexity savings of several orders of magnitude over JML, but has higher complexity than SRSJD. This is the cost for the better performance of PD-IE (cf. Fig. 3.9). The comparison of symbol estimation with explicit CCI estimation and joint detection in PD-IE indicates that joint detection of high energy symbols and residual CCI has complexity advantages over explicit CCI estimation. This is expected because explicit CCI estimation requires an additional trellis stage for each additional signal, whereas for joint detection, the complexity of each symbol estimator remains constant. This can be seen in Table 3.5 by the increasing complexity ratio C_{se}/C_{lc} for explicit CCI estimation and decreasing values for joint detection.

3.6 CONCLUSIONS

This chapter has presented a unified list-based algorithmic structure for the separation and detection of multiple co-channel signals in an overloaded receiver and transmission through an AWGN channel. Detection at the receiver is performed in two stages: linear preprocessing and nonlinear suboptimum symbol detection using PD-IE. This two stage structure is applied to receivers with either a UCA or a ULA. The approach may also be applied to receivers with arbitrary antenna array geometries.

The linear preprocessor employs either spatial beam forming or diversity combining to reduce the level of CCI in the received signals. Due to the overloaded environment and the linear preprocessing, residual CCI is still present. This is accounted for in the subsequent PD-IE algorithm, which estimates the residual CCI and performs iterative list detection of the received symbols.

Performance is evaluated using Monte Carlo simulation. PD-IE is shown to approximate the optimum JML detector with significantly lower complexity and outperforms existing low complexity algorithms. Comparison to the SRSJD algorithm of [22]

shows that PD-IE yields better performance at the cost of some increase in complexity. Unlike JML whose complexity is exponential in the number of signals, PD-IE has a much lower rate of complexity increase. Complexity savings become more significant when the number of receive antennas is large. PD-IE simulation results suggest that joint detection and CCI estimation has advantages over explicit CCI estimation. It achieves a better performance-complexity tradeoff, yields simpler implementation and most importantly, it can be used with arbitrary receive array geometries. The parallel processing structure makes PD-IE well suited for practical implementation.

Chapter 4

DETECTOR FOR THE MULTIPATH FADING CHANNEL

IN THIS chapter, receiver design and signal processing are proposed for the detection of multiple co-channel signals in a frequency-flat Rayleigh fading channel under overloaded conditions. The transmitted co-channel signals impinge on a receiver employing an antenna array. Optimum detectors such as JMAP and JML often have prohibitively high complexity due to their exhaustive search algorithm. Reduced complexity algorithms are therefore required for practical systems. In a multipath fading channel, the elements of the channel matrix are random variables. This means that in contrast to an AWGN channel, a preprocessor in a reduced complexity receiver cannot always concentrate the channel energy to only few elements in each matrix row. In case of the previously described PD-IE detector, there would be too many high energy elements which would result in a large subset size and prohibitively high complexity. Hence, a different approach is required to separate and detect the transmitted signals in a multipath fading channel.

The proposed receiver structure again uses a two stage detection process. It consists of a linear preprocessor which is followed by a novel nonlinear iterative symbol detector. The detection algorithm performs a group-wise search to extract the ordered list of most likely symbols. This is called List Group Search (LGS) detection. The preprocessor uses diversity combining to mitigate CCI. Here, the optimum MRC technique is employed. It effectively focusses the received signal energies and allows the formation of symbol subsets with either high or low received energy. The subset with low energy represents residual CCI. This occurs under overload when using a linear preprocessor. In the

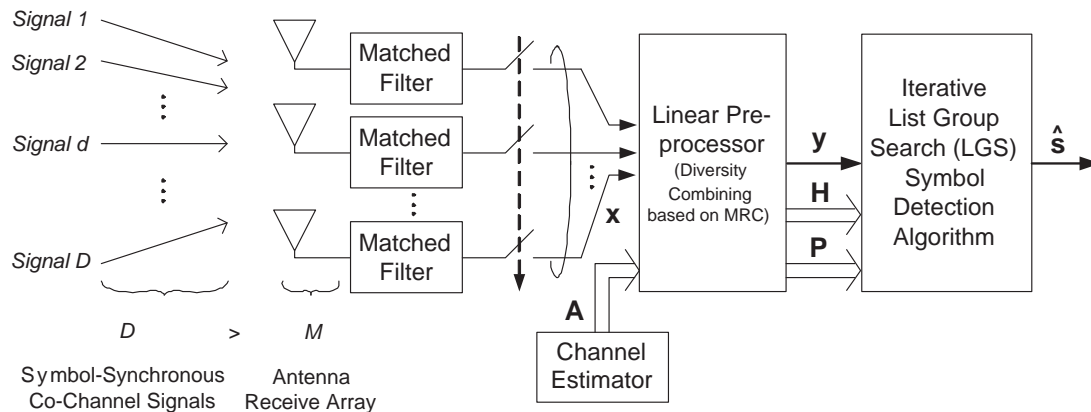


Figure 4.1 Receiver structure for the LGS detector.

following detection stage, the symbol subset with high energy is further split into symbol groups over which an exhaustive search is performed. Residual CCI is estimated to aid detection. The result is lower overall complexity than required for optimum JML detection. Simulation results demonstrate that the proposed receiver structure achieves good complexity-performance tradeoffs.

In Section 4.1, the system model and the receiver structure are introduced. The preprocessor is described in Section 4.2 and the detector is discussed in detail in Section 4.3. Simulation results and a complexity analysis are presented in Sections 4.4 and 4.5, respectively. Conclusions are drawn in Section 4.6.

4.1 SYSTEM MODEL AND RECEIVER STRUCTURE

The overloaded communication system considered in this chapter assumes that multiple co-channel signals are transmitted through a frequency-flat Rayleigh fading channel. The overall structure of the receiver is illustrated in Fig. 4.1. It appears similar to the PD-IE receiver in Fig. 3.1. The main differences lie in the channel model and in the detection stage.

The receiver front-end is equipped with an M -element arbitrary receive antenna array whose antennas are uncorrelated¹. There are D independent co-channel signals that impinge on each receive antenna. The signals are assumed to be equal energy

¹This requires the antennas to be spaced far apart.

QPSK signals that are symbol-synchronous² but independently transmitted. The receiver is overloaded with load factor $f(D, M) > 1$. At each antenna, the received signal is passed through a filter matched to the transmitted pulse shape and is then sampled at the symbol rate to give the received signal vector $\mathbf{x} \in \mathbb{C}^M$ in each interval,

$$\mathbf{x} = \mathbf{A}\mathbf{s} + \mathbf{n}, \quad (4.1)$$

where $\mathbf{A} \in \mathbb{C}^{M \times D}$ is the channel response matrix³ and $\mathbf{s} \in \mathcal{A}^D$ is given as the symbol vector $\mathbf{s} = [s_1 \ s_2 \ \dots \ s_D]^T$ containing the transmitted symbols s_d . Each s_d is independent and uniformly drawn from an alphabet \mathcal{A} . The elements of \mathbf{A} are independent, complex Gaussian random variables with zero mean and variance $1/2$ in each dimension. This is in contrast to the AWGN channel in (3.1) where \mathbf{A} includes the array response⁴. The vector $\mathbf{n} \in \mathbb{C}^M$ denotes temporally uncorrelated noise with zero mean and autocorrelation $\Phi_{nn} = E[\mathbf{nn}^H]$, where $E[\cdot]$ is the expectation operator. The noise is also assumed to be spatially uncorrelated so that $\Phi_{nn} = \sigma_n^2 \mathbf{I}$, where σ_n^2 denotes the noise variance and \mathbf{I} is the $M \times M$ identity matrix.

4.2 PREPROCESSOR

The received signal vector \mathbf{x} and the channel response matrix \mathbf{A} are input to a preprocessor. It performs diversity combining to maximize the SNR of each individual signal. This improves the error performance of the following detection stage.

4.2.1 Maximum Ratio Diversity Combining

MRC is the optimum diversity combining technique. It requires CSI at the receiver, specifically knowledge of the channel response matrix \mathbf{A} . Optimum performance is obtained if the antenna elements are uncorrelated. This requires the antenna elements

²The extension to the non-synchronous case requires an additional synchronization process.

³This is the same channel model described by (2.1). The matrix \mathbf{H} of (2.1) is here denoted \mathbf{A} to unify notation with Chapter 3.

⁴The Rayleigh fading channel requires sufficient antenna separation to avoid correlation in the received signals. As a result, the antenna array response has no meaning due to uncorrelated replicas of the transmitted signals at the receiver.

to be spaced far apart which is assumed here. In practice, the antenna element spacing exceeds $1/2$ the carrier frequency wave length and is often in the order of several wave lengths⁵.

MRC maps the receive vector $\mathbf{x} \in \mathbb{C}^M$ into a vector $\check{\mathbf{y}} \in \mathbb{C}^D$ such that each of the D signals has maximum SNR in one of the components of $\check{\mathbf{y}}$. The preprocessor output is a weighted linear combination of the different signal replicas observed at the receive antennas. The MRC weight matrix is given by $\check{\mathbf{W}} = \mathbf{A}^H$ [25]. Multiplying (4.1) with $\check{\mathbf{W}}$ gives the desired MRC received signal vector $\check{\mathbf{y}}$ as

$$\begin{aligned}\check{\mathbf{y}} &= \check{\mathbf{W}}\mathbf{x} \\ &= \check{\mathbf{W}}\mathbf{A}\mathbf{s} + \check{\mathbf{W}}\mathbf{n}.\end{aligned}\tag{4.2}$$

The MRC operation in (4.2) results in correlation and produces the colored noise term $\check{\mathbf{W}}\mathbf{n}$. This degrades performance in the following detection stage. To overcome this problem a noise whitening filter is used to regain optimum detection performance in a similar manner to the work of [48].

The noise whitening filter is now described. First, define the square matrix $\check{\mathbf{H}} \in \mathbb{C}^{D \times D}$ as $\check{\mathbf{H}} = \mathbf{A}^H \mathbf{A}$. Using $\check{\mathbf{H}}$, (4.2) becomes

$$\check{\mathbf{y}} = \check{\mathbf{H}}\mathbf{s} + \check{\mathbf{W}}\mathbf{n}.\tag{4.3}$$

Letting $\mathbf{H} = \check{\mathbf{H}}^{1/2}$ and denoting the square root inverse⁶ of $\check{\mathbf{H}}$ as $\check{\mathbf{H}}^{-1/2}$, the noise whitened MRC output is obtained as

$$\begin{aligned}\mathbf{y} &= \check{\mathbf{H}}^{-1/2}\check{\mathbf{y}} \\ &= \mathbf{H}\mathbf{s} + \mathbf{z},\end{aligned}\tag{4.4}$$

where $\mathbf{y} \in \mathbb{C}^D$ is the filtered received signal vector and $\mathbf{z} \in \mathbb{C}^D$ is the whitened noise

⁵Physical constraints often do not allow the use of antenna spacing that is required for independent fading across multiple antennas [47].

⁶The matrix $\check{\mathbf{H}}^{-1/2}$ is the response matrix of the noise whitening filter.

vector which is computed as $\mathbf{z} = \mathbf{H}^{-1} \mathbf{A}^H \mathbf{n}$. If the JML decision metric of (2.10) is applied to (4.4) the optimum JML detector becomes

$$\hat{\mathbf{s}} = \arg \min_{\mathbf{s} \in \mathcal{A}^D} \|\mathbf{y} - \mathbf{H}\mathbf{s}\|^2, \quad (4.5)$$

where \mathcal{A}^D is the combined $2D$ -dimensional alphabet formed by the D signals. Note that (4.5) has the same form as the JML detector for the AWGN channel in (3.6). The difference in the two lies in the definition of \mathbf{H} .

4.2.2 Sparsity Matrix

After the preprocessor has computed \mathbf{H} , the sparsity matrix $\mathbf{P} \in \mathbb{N}_2^{D \times D}$ is derived. It is formed by denoting the elements with “low” and “high” energy in \mathbf{H} as ‘0’ and ‘1’ values, respectively. Here, the same approach as in Chapter 3 is used to obtain \mathbf{P} . The selection algorithm employs the SSSER and SEAIR criteria defined in (3.8) and (3.9), respectively and is described in Table 3.1. Since in a frequency-flat Rayleigh fading channel the elements in \mathbf{H} are random variables, it can happen that some columns of \mathbf{H} contain no elements that are considered as “high” energy. In this case, the matrix \mathbf{P} contains only ‘0’ elements for these columns which means that the corresponding symbols would not be detected by the LGS detector. To avoid this problem, all column vectors $\mathbf{p}(d) \in \mathbf{P}$ with $\mathbf{p}(d) = \mathbf{0}$ are set to $\mathbf{p}(d) = \mathbf{1}$, where $\mathbf{1}$ is a length D vector containing only unit elements.

The d th row vectors of \mathbf{H} and \mathbf{P} are denoted as $\mathbf{h}[d] \in \mathbf{H}$ and $\mathbf{p}[d] \in \mathbf{P}$ and the elements are denoted as h_{du} and p_{du} . In addition, column group matrices are denoted as \mathbf{H}_j and contain one or more column vectors of \mathbf{H} .

The definition of enumeration sets $U_e[d] = \{u | p_{du} = 1, p_{du} \in \mathbf{p}[d]\}$ and their complements $\bar{U}_e[d] = \{v | p_{dv} = 0, p_{dv} \in \mathbf{p}[d]\}$ for $d = 1, 2, \dots, D$ provides a means of specifying the symbol sets with either high or low energy elements in each row of \mathbf{H} . For the d th row, $\mathbf{h}[d] \in \mathbf{H}$, these are given by

$$\tau[d] = \{s_u | u \in U_e[d]\}, \quad \omega[d] = \{s_v | v \in \bar{U}_e[d]\}, \quad (4.6)$$

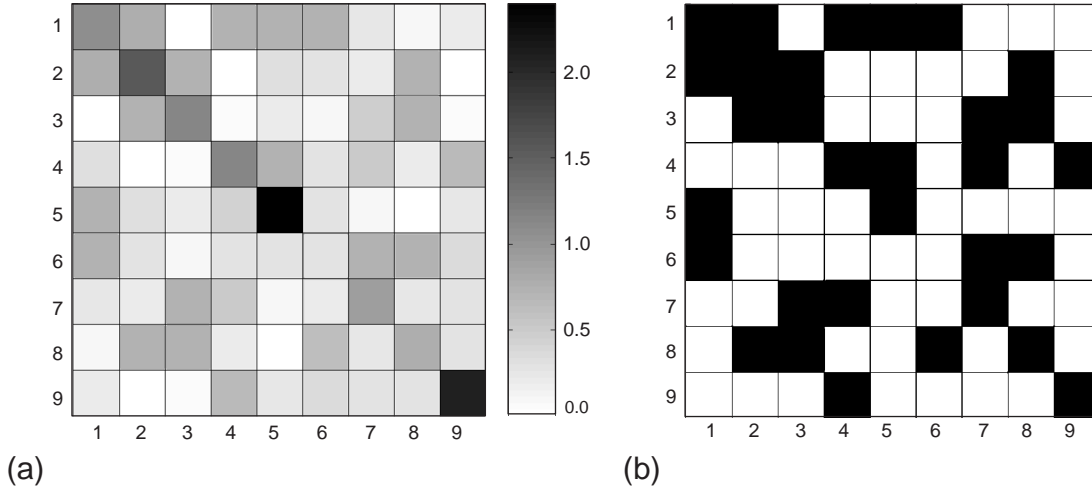


Figure 4.2 (a) Example of the energy of the preprocessor output matrix \mathbf{H} , $(\mathbf{H}^H \mathbf{H})^{(1/2)}$, for a receiver with $M = 6$ antennas and $D = 9$ signals in a frequency-flat Rayleigh fading channel, (b) Sparsity matrix \mathbf{P} derived from \mathbf{H} using the selection algorithm of Table 3.1.

where $\tau[d]$ denotes high and $\omega[d]$ is the low energy symbol set. Consequently, each row vector $\mathbf{h}[d]$ can be split into two subset vectors $\mathbf{h}_\tau[d]$ and $\mathbf{h}_\omega[d]$, where $\mathbf{h}_\tau[d] = \{h_{du}|u \in U_e[d]\}$ and $\mathbf{h}_\omega[d] = \{h_{dv}|v \in \bar{U}_e[d]\}$, respectively. The symbol vectors corresponding to the subsets $\tau[d]$ and $\omega[d]$ are denoted as \mathbf{s}_τ and \mathbf{s}_ω , respectively.

Fig. 4.2(a) depicts an example of the energy of \mathbf{H} after performing MRC and noise whitening for a receiver with $M = 6$ antennas and $D = 9$ equal energy signals. The corresponding sparsity matrix \mathbf{P} is shown in Fig. 4.2(b). For example in row 3 of Fig. 4.2(b), the sets $\tau[3]$ and $\omega[3]$ are $\tau[3] = \{s_2, s_3, s_7, s_8\}$ and $\omega[3] = \{s_1, s_4, s_5, s_6, s_9\}$ with corresponding subset vectors $\mathbf{h}_\tau[3] = [h_{32} \ h_{33} \ h_{37} \ h_{38}]$ and $\mathbf{h}_\omega[3] = [h_{31} \ h_{34} \ h_{35} \ h_{36} \ h_{39}]$, respectively. Similarly, the symbol vectors are $\mathbf{s}_\tau = [s_2 \ s_3 \ s_7 \ s_8]$ and $\mathbf{s}_\omega = [s_1 \ s_4 \ s_5 \ s_6 \ s_9]$. All other rows are characterized accordingly.

4.3 LIST GROUP SEARCH DETECTION

The symbol detector for the frequency-flat Rayleigh fading channel is now developed. It is known as List Group Search (LGS) detector and has the following key features:

- The LGS detector uses nonlinear detection to achieve good performance under overload.

- It splits up the symbol subsets represented by “high” energy elements in the channel matrix into multiple symbol groups. The algorithm then independently searches over the symbols in each group thereby reducing the computational complexity compared to optimum JML detection.
- Parallel detector branches allow fast processing for practical implementations.
- The LGS detector accounts for residual CCI in order to achieve good performance under overload.
- List processing and the output of an ordered list of likely symbol estimates provide reliability information. This makes the LGS detector ideal for use with error control decoders.

A block diagram of the proposed LGS detector is shown in Fig. 4.3. It takes the quantities \mathbf{y} , \mathbf{H} and \mathbf{P} from the preprocessor as inputs and outputs the ordered ($D \times 1$) list of L symbol vectors, $\mathcal{S} = \{\hat{\mathbf{s}}^{(1)}, \hat{\mathbf{s}}^{(2)}, \dots, \hat{\mathbf{s}}^{(L)}\}$, where the ordering⁷ from most to least likely.

The LGS detector uses D parallel processing branches each containing a Branch List Estimator (BLE). The d th BLE has \mathbf{y} , \mathbf{H} , \mathbf{P} and the list $\mathcal{S}_{in}[d]$ as inputs and outputs the ordered branch list $\mathcal{S}_{br}[d] = \{\hat{\mathbf{s}}_{br}^{(1)}[d], \hat{\mathbf{s}}_{br}^{(2)}[d], \dots, \hat{\mathbf{s}}_{br}^{(L)}[d]\}$. The elements $\hat{\mathbf{s}}_{br}^{(k)}[d] \in \mathcal{S}_{br}[d]$ are the estimated ($D \times 1$) branch symbol vectors. The input lists $\mathcal{S}_{in}[d]$ are either the BLE output branch lists or the tentative list \mathcal{S} from the previous detector iteration. This is shown in Fig. 4.3. Detection starts by initializing the list \mathcal{S} with random symbol values drawn from the alphabet \mathcal{A} . The overall detector then performs Q global iterations in which the input lists $\mathcal{S}_{in}[d]$ are initialized with symbol values from the tentative combined list \mathcal{S} .

The LGS detector exchanges tentative branch lists $\mathcal{S}_{br}[d]$ between BLE blocks to update estimates of the symbols with low energy contribution. Therefore, a switch at the input of each BLE is required as shown in Fig. 4.3. The order in which the branch

⁷The ordering is based on an Euclidean distance metric and is similar to the PD-IE algorithm in Chapter 3.

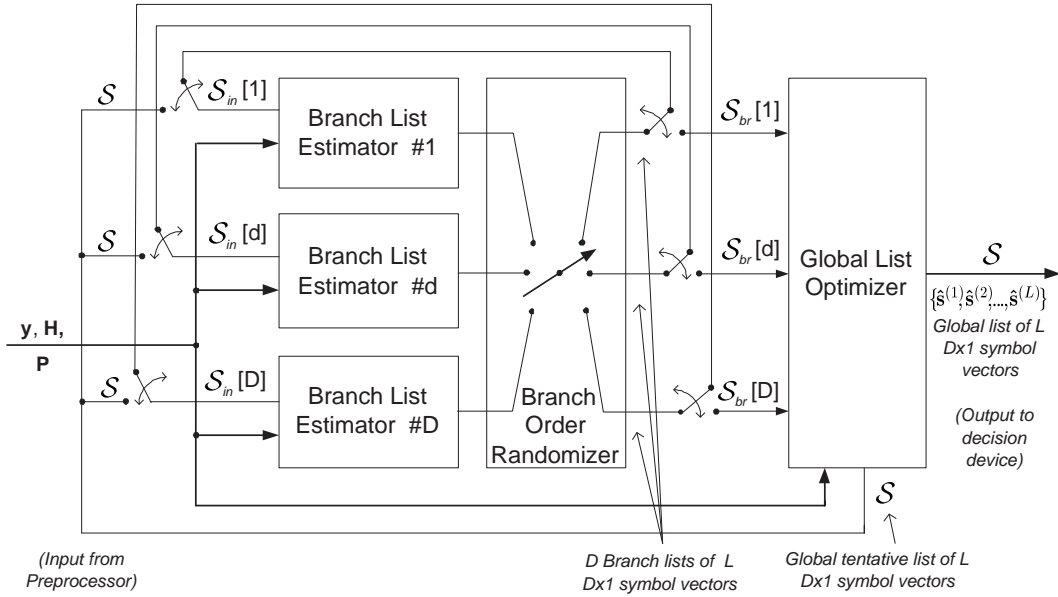


Figure 4.3 Block diagram of the LGS detector.

lists are passed to the next branch is randomized to break up statistical dependencies. After Q_{BLE} iterations, the D lists $\mathcal{S}_{br}[d]$ are input to the Global List Optimizer (GLO) stage. Here, the global list \mathcal{S} is updated by searching over the symbol groups. The improved list \mathcal{S} is fed back to the D branches and after $q = Q$ iterations the LGS detector outputs \mathcal{S} . A decision device selects the first element $\hat{\mathbf{s}}_1 \in \mathcal{S}$ as the best estimate \mathbf{s} . Alternatively, \mathcal{S} can be used to compute soft information for subsequent stages such as error control decoders.

4.3.1 Branch List Estimation

The d th BLE searches only over the symbols grouped in the set $\tau[d]$. Using the subset vectors $\mathbf{h}_\tau[d]$ and $\mathbf{h}_\omega[d]$, the d th receive component can be written as

$$y[d] = \mathbf{h}_\tau[d]\mathbf{s}_\tau + \mathbf{h}_\omega[d]\mathbf{s}_\omega + z[d], \quad (4.7)$$

where $z[d] \in \mathbf{z}$ is the d th noise element. In a fading channel, the size of the high energy symbol subsets, $|\tau[d]|$, is a random variable with $0 \leq |\tau[d]| \leq D$. The resulting search complexity often exceeds the limit of the receiver. In the LGS detector, this

problem is solved by splitting each subset $\tau[d]$ into G groups, $\tau_j[d]$, such that $\tau[d] = \{\tau_1[d], \tau_2[d], \dots, \tau_G[d]\}$. The size of the j th group is denoted $|\tau_j[d]|$. Similarly, the vector $\mathbf{h}_\tau[d]$ is split into G group vectors denoted $\mathbf{h}_\tau[d] = [\mathbf{h}_1[d], \mathbf{h}_2[d], \dots, \mathbf{h}_G[d]]$.

In order to search over the group $j = 1$, (4.7) is rewritten as

$$y[d] = \mathbf{h}_1[d]\mathbf{s}_1 + \left[\left(\sum_{j=2}^G \mathbf{h}_j[d]\mathbf{s}_j \right) + \mathbf{h}_\omega[d]\mathbf{s}_\omega + z[d] \right], \quad (4.8)$$

where \mathbf{s}_j denotes the group vector of the symbols in $\tau_j[d]$. Note that for the detection of group $j = 1$ all terms within the square brackets are undesired components defined as $y_u[d]$. Hence, (4.8) may be written as

$$y[d] = \mathbf{h}_1[d]\mathbf{s}_1 + y_u[d]. \quad (4.9)$$

The exhaustive search of the d th BLE over the symbols of the j th group, $\tau_j[d]$, is described by

$$\hat{\mathbf{s}}_j = \arg \min_{\mathbf{s}_j \in \tau_j[d]} \|y_j[d] - \mathbf{h}_j[d]\mathbf{s}_j\|^2, \quad j = 1, 2, \dots, G \quad (4.10)$$

where the received component for the j th group is

$$y_j[d] = y_0[d] - \sum_{i=1, i \neq j}^G \mathbf{h}_i[d]\mathbf{s}_i \quad (4.11)$$

and the received signal after cancelling contributions from all signals with low energy is given by

$$y_0[d] = y[d] - \mathbf{h}_\omega[d]\mathbf{s}_\omega. \quad (4.12)$$

This is done before processing the first group $\tau_1[d]$.

Branch symbol lists $\mathcal{S}_{br}[d]$ are obtained by using (4.10), (4.11) and (4.12). The branch list estimation algorithm is described in Table 4.1. For a given candidate symbol

Table 4.1 Iterative group-wise branch list estimation algorithm

-
1. Initialize the d th branch list $\mathcal{S}_{br}[d]$ of L length D symbol vectors and the corresponding list of L branch error metrics $\mathcal{E}_{br}[d]$.
 2. Find the elements $s_{br}^{(l)}[d] \in \mathcal{S}_{br}[d]$ and $e_{br}^{(l)}[d] \in \mathcal{E}_{br}[d]$ by computing (4.10) and (4.13) for all L elements $s_{in}^{(l)}[d]$ from the input list $\mathcal{S}_{in}[d]$.
 3. Apply $\mathbf{p}[d] \in \mathbf{P}$ to obtain symbol values for \mathbf{s}_ω from the first element $s_{in}^{(1)}[d] \in \mathcal{S}_{in}[d]$. Cancel residual CCI using (4.12).
 4. For $\theta = 1 : \Theta$ do
 - (a) Find the members of the G groups τ_j , $j = 1, 2, \dots, G$, by choosing $|\tau_j|$ column indices u from $\mathbf{p}[d] \in \mathbf{P}$ with $p_{du} = 1$. If $\theta = 1$ select the indices u according to decreasing value of $\|h_{du}\|^2$ otherwise use random selection.
 - (b) For $j = 1 : G$ do
 - i. Perform an exhaustive search over all symbol values of the j th group τ_j using (4.10) and (4.13). Symbol values for all elements \mathbf{s}_i from the undesired groups i are drawn from $\mathbf{s}_{in}^{(1)}[d] \in \mathcal{S}_{in}[d]$. Update the lists $\mathcal{S}_{in}[d]$ and $\mathcal{E}_{br}[d]$.
 - ii. Calculate $y_{j+1}[d]$ using (4.11).
 - iii. Increase the group index j , $j = j + 1$.
 - (c) Increase the iteration index θ , $\theta = \theta + 1$.
 5. Output the list $\mathcal{S}_{br}[d]$.
-

vector $\hat{\mathbf{s}}$, the squared Euclidean distance metric

$$e[d] = |y[d] - \mathbf{h}[d]\hat{\mathbf{s}}|^2 \quad (4.13)$$

is used to order the symbol list. The branch list estimation algorithm in Table 4.1 is employed by each BLE during Q_{BLE} iterations.

4.3.2 Global List Optimizer

After the branch lists $\mathcal{S}_{br}[d]$ have been computed they are passed on to the Global List Optimizer (GLO), as shown in Fig. 4.3. Here, the lists are searched to find symbol vectors $\hat{\mathbf{s}}^{(l)} \in \mathcal{S}$ that minimize (4.5). The global list optimization algorithm is also based on a group-wise search to reduce the computational complexity. In the Global List Optimizer (GLO), the set v is defined containing the symbols from all D signals. This is in contrast to the BLEs, where the symbols are divided into two subsets with either low or high energy contribution in \mathbf{H} , τ and ω , respectively. The symbol set v

is given by

$$v = \{s_1, s_2, \dots, s_D\}. \quad (4.14)$$

Defining subsets v_j for F groups⁸, v is written as $v = \{v_1, v_2, \dots, v_F\}$. Similar to (4.8), (4.4) can now be written using column group matrices as

$$\mathbf{y} = \mathbf{H}_j \mathbf{s}_j + \left[\left(\sum_{i=1, i \neq j}^F \mathbf{H}_i \mathbf{s}_i \right) + \mathbf{z} \right] \quad (4.15)$$

$$= \mathbf{H}_j \mathbf{s}_j + \mathbf{y}_u, \quad (4.16)$$

where, for the detection of the j th group, the terms within the square brackets are the undesired components \mathbf{y}_u . The group symbol vectors \mathbf{s}_i and \mathbf{s}_j are drawn from their corresponding sets $v_i \in v$ and $v_j \in v$, respectively. Note that the columns of \mathbf{H}_i and \mathbf{H}_j are the permuted column vectors of \mathbf{H} . Symbol decisions are based on

$$\hat{\mathbf{s}}_j = \arg \min_{\mathbf{s}_j \in v_j} \|\mathbf{y}_j - \mathbf{H}_j \mathbf{s}_j\|^2, \quad j = 1, 2, \dots, F \quad (4.17)$$

where the received component for the j th group is

$$\mathbf{y}_j = \mathbf{y} - \sum_{i=1, i \neq j}^F \mathbf{H}_i \mathbf{s}_i. \quad (4.18)$$

All candidate symbol vectors $\hat{\mathbf{s}}$ are evaluated by their Euclidean distance

$$e = \|\mathbf{y} - \mathbf{H} \hat{\mathbf{s}}\|^2. \quad (4.19)$$

The GLO stage in the LGS detector stores the tentative global list \mathcal{S} and the corresponding list \mathcal{E} containing the L error metrics $e^{(l)} \in \mathcal{E}$. The list \mathcal{S} is fed back to the D branches and output by the LGS-MUD detector after Q global iterations. Table 4.2 summarizes the global list optimization algorithm.

⁸The number of groups F and the group size represent a complexity/ performance trade-off. These are preset for simulations but will be determined by further complexity/ performance considerations in a practical detector.

Table 4.2 Iterative group-wise global list optimization algorithm

-
1. Compute (4.19) for all non-redundant input vectors $\mathbf{s}_{br}^{(k)}[d] \in \mathcal{S}_{br}[d]$. There are $1 \leq K \leq (LD)$ non-redundant input vectors. Update the tentative list \mathcal{S} by storing the L vectors with minimum error metric in \mathcal{S} . The corresponding error metrics are stored in \mathcal{E} .
 2. Allocate a L -member list of length D search symbol vectors, \mathcal{S}_{search} .
 3. For $\phi = 1 : \Phi$ do
 - (a) Find the members of the F groups v_j , $j = 1, 2, \dots, F$, by choosing $|v_j|$ column indices u . If $\phi = 1$ select the indices u according to decreasing value of $\|\mathbf{h}[u]\|^2$ otherwise use random selection. Note that here $\mathbf{h}[u]$ is the u th column vector of \mathbf{H} .
 - (b) For $j = 1 : F$ do
 - i. Copy the L symbol vectors $\hat{\mathbf{s}}^{(l)} \in \mathcal{S}$ into \mathcal{S}_{search} . Delete the column entries of the symbols in the j th group and remove all redundant elements from \mathcal{S}_{search} . The resulting list for the j th group is denoted $\tilde{\mathcal{S}}_{search}$ and has size $1 \leq K_j \leq L$.
 - ii. For $k = 1 : K_j$ do
 - A. Use (4.18) to calculate \mathbf{y}_j for the k th list member. This is denoted as $\mathbf{y}_j^{(k)}$. Symbol values for the elements \mathbf{s}_i from all groups i are drawn from $\hat{\mathbf{s}}^{(k)} \in \tilde{\mathcal{S}}_{search}$.
 - B. Perform an exhaustive search over all symbol values of the j th group v_j using (4.17) and (4.19). Update the lists \mathcal{S} and \mathcal{E} .
 - iii. Increase the group index j , $j = j + 1$.
 - (c) Increase the iteration index ϕ , $\phi = \phi + 1$.
 4. Store the lists \mathcal{S} and \mathcal{E} . Output \mathcal{S} .
-

4.4 PERFORMANCE

Performance results for the LGS and JML detectors are obtained by simulation. It is assumed that D equal energy QPSK (4-QAM) signals are transmitted through a frequency-flat Rayleigh fading channel. The D co-channel signals impinge on a receiver with an array of M uncorrelated antennas. Results are obtained for the two cases where the receiver has either perfect or imperfect CSI. The SNR at each receive antenna is given as $\Gamma = 10 \log_{10} (\sigma_s^2 / \sigma_n^2)$, where σ_s^2 denotes the average received signal power. Performance is evaluated in terms of the SER of the worst signal. Simulations were stopped after 80 symbol errors occurred in the detection of one signal.

4.4.1 Perfect Channel State Information

If perfect CSI is assumed, the channel response matrix \mathbf{A} is known to the receiver. This provides a measure of the best achievable detection performance. In Fig. 4.4, the SER of a $M = 4$ antenna receiver for different numbers of co-channel signals D is shown.

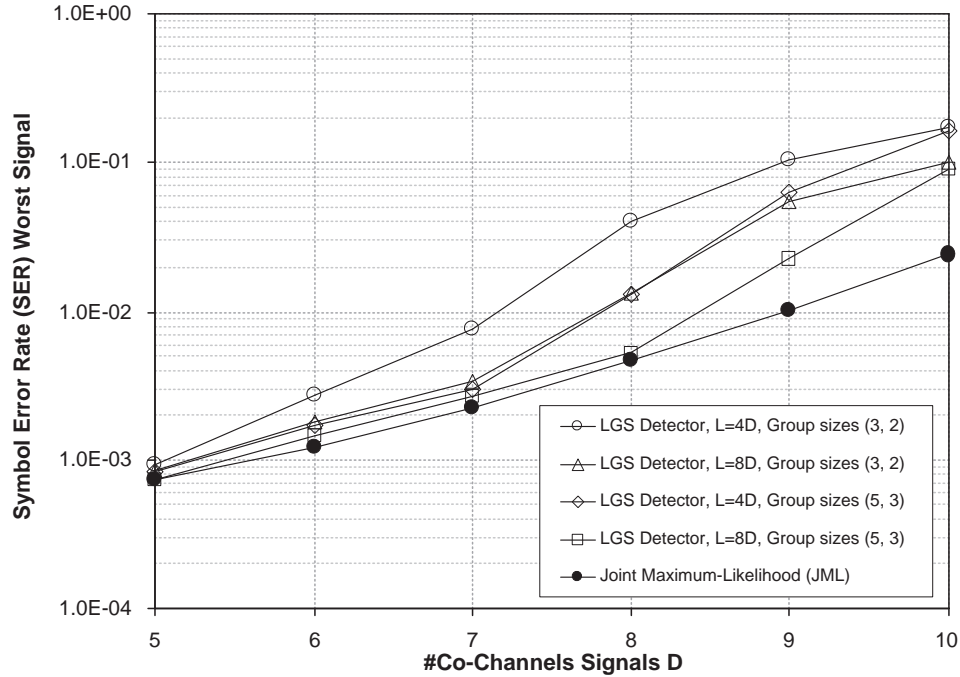


Figure 4.4 SER versus the number of co-channel signals for a $M = 4$ antenna receiver at SNR, $\Gamma = 10dB$.

Table 4.3 Simulation parameters for LGS detection in Fig. 4.4.

SEAIR threshold	2	List size L (for \mathcal{S} and $\mathcal{S}_{br}[d]$)	$4D, 8D$
SSSER threshold	0.5	BLE group iterations Θ	2
Receive antennas M	4	BLE iterations Q_{BLE}	2
Co-channel signals D	$> M$	GLO group iterations Φ	2
BLE group size $ \tau_j $	3, 5	Overall iterations Q	2
GLO group size $ v_j $	2, 3	Symbol errors	100

The parameters used for LGS simulation in Fig. 4.4 are summarized in Table 4.3.

JML is the optimum detector and provides a lower bound on the error performance of the LGS detector. The SER degrades with increasing number of co-channel signals D . For list size $L = 8D$ and group sizes $(|\tau_j|, |v_j|) = (5, 3)$, the LGS detector achieves near JML performance for up to $D = 8$ signals (load factor $f(D, M) \leq 2$). Under heavy overload, i.e. $f(D, M) > 2$, performance is degraded due to the use of groups, limitations in list size and iterative processing. It can further be seen that decreasing the list size to $L = 4D$ degrades the performance of the LGS detector over all D . This is caused by an increased probability that the correct symbols are not included

Table 4.4 Simulation parameters for LGS detection in Fig. 4.5.

SEAIR threshold	2	List size L (for \mathcal{S} and $\mathcal{S}_{br}[d]$)	$2D, 4D, 8D$
SSSER threshold	0.5	BLE group iterations Θ	2
Receive antennas M	6	BLE iterations Q_{BLE}	2
Co-channel signals D	9, 12	GLO group iterations Φ	2
BLE group size $ \tau_j $	5	Overall iterations Q	2, 3
GLO group size $ v_j $	4	Symbol errors	100

in the lists $\mathcal{S}_{br}[d]$ and \mathcal{S} . For smaller group sizes, i.e. $(|\tau_j|, |v_j|) = (3, 2)$, the LGS detector loses performance if the receiver is heavily overloaded, i.e. $D > 6$ signals ($f(D, M) > 1.5$). It is also noted that in contrast to the detection in AWGN channels (Chapter 3), in a Rayleigh fading channel the geometry of the receive antenna array does not have any effect on the error performance. This is due to the assumption of no correlation in the received signal replicas and, in practice, requires sufficient antenna spacing. As a result, a sudden dip in the SER curves for different numbers of D does not occur. Better performance for odd values of D was observed for the AWGN channel and receivers with UCA antenna array (cf. Fig. 3.9).

Fig. 4.5 illustrates SER curves for a $M = 6$ antenna receiver in the cases of $D = 9$ (Fig. 4.5(a)) and $D = 12$ (Fig. 4.5(b)) co-channel signals at different SNRs. The LGS detector uses group sizes $(|\tau_j|, |v_j|) = (5, 4)$. The number of global iterations is set to $Q = 2$ for $D = 9$ signals and $Q = 3$ for $D = 12$ signals. The simulation parameters are provided in Table 4.4. JML provides a lower bound on the error performance in Fig. 4.5. SER curves for JML were obtained by simulation for SNR $\Gamma \leq 5dB$ and by computing the bound⁹ in [13] for $\Gamma > 5dB$.

The results show that the LGS detector approximates JML in the low SNR region but introduces an error floor for small list sizes, i.e. $L = 2D$ and $4D$, and under heavy overload, i.e. $D = 12$ ($f(D, M) = 2$). Near JML performance over a wide range of SNR and under heavy overload is achieved by increasing the list size L . This is at the cost of an increase in complexity. The comparison of the error performance of the LGS

⁹More information on the computation of the JML performance bound is found in Chapter 5 of this thesis.

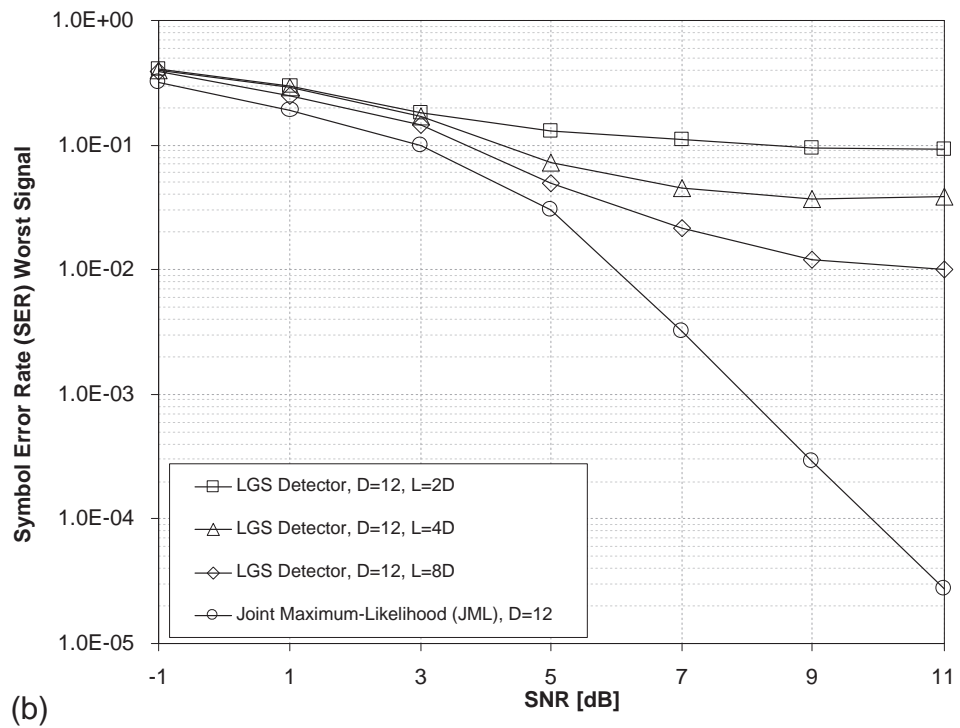
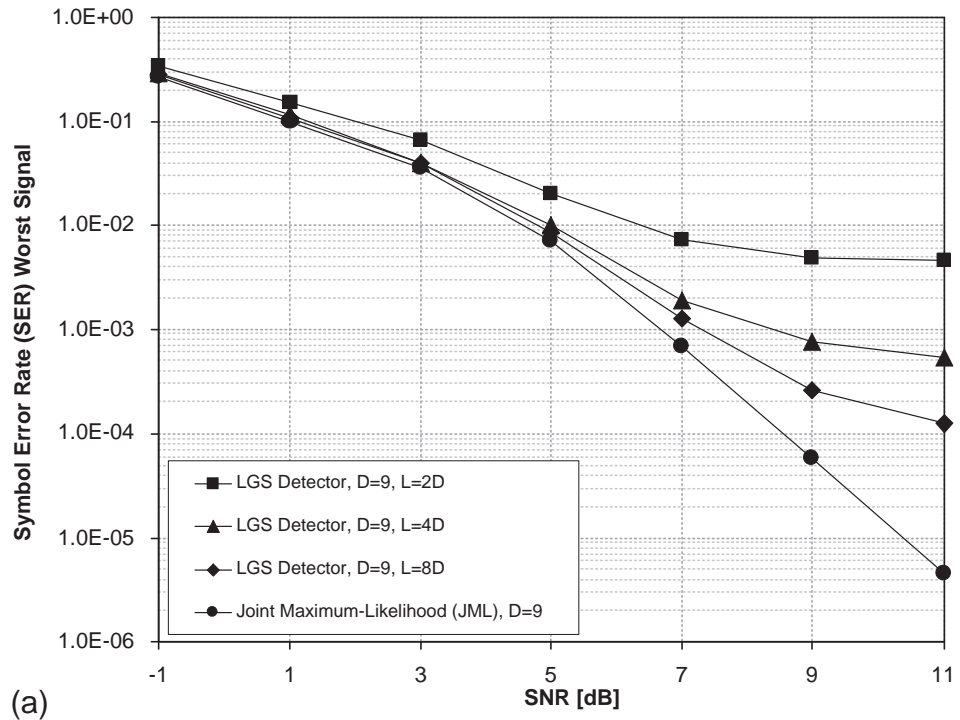


Figure 4.5 SER versus SNR for a $M = 6$ antenna receiver with (a) $D = 9$ and (b) $D = 12$ co-channel signals.

Table 4.5 Simulation parameters for LGS detection in Figs. 4.6 and 4.7.

SEAIR threshold	2	List size L (for \mathcal{S} and $\mathcal{S}_{br}[d]$)	$8D$
SSSER threshold	0.5	BLE group iterations Θ	2
Receive antennas M	4	BLE iterations Q_{BLE}	2
Co-channel signals D	$> M$	GLO group iterations Φ	2
BLE group size $ \tau_j $	3	Overall iterations Q	2
GLO group size $ v_j $	2	Symbol errors	100

and the PD-IE detectors shows that in order to achieve near JML performance, the LGS algorithm requires a larger list size than PD-IE¹⁰. This is due to the formation of multiple groups in the LGS detector. In general, larger group sizes ($|\tau_j|, |v_j|$) result in higher computational complexity and better performance.

4.4.2 Imperfect Channel State Information

The case of imperfect CSI at the receiver is now considered. Here, the same approach as in Chapter 3 is used. The channel response matrix \mathbf{A} with imperfect CSI is written as

$$\hat{\mathbf{A}} = \eta \mathbf{A} + \sqrt{1 - \eta^2} \mathbf{E}, \quad (4.20)$$

where $\hat{\mathbf{A}} \in \mathbb{C}^{M \times D}$ is the imperfect CSI output matrix, $\mathbf{A} \in \mathbb{C}^{M \times D}$ is the actual CSI and $\mathbf{E} \in \mathbb{C}^{M \times D}$ is the matrix of i.i.d. complex Gaussian random variables. The matrix $\hat{\mathbf{A}}$ is used instead of \mathbf{A} in (4.1). The power correlation coefficient η is set to $\eta = 0.98$, 0.995 and 1 (perfect CSI). Table 4.5 summarizes the receiver setup and the detection parameters used in Figs. 4.6 and 4.7.

In Fig. 4.6, the SER with perfect and imperfect CSI is shown for a $M = 4$ antenna receiver and various numbers of co-channel signals. The imperfect CSI clearly degrades the error performance and causes an upshift of the SER curves. This occurs for both JML and LGS detectors. The gap in error performance between the two detectors decreases at higher SER.

¹⁰PD-IE with joint detection can also be used in a frequency-flat Rayleigh fading channel. However, it would have higher complexity than LGS detection due to larger subset sizes.

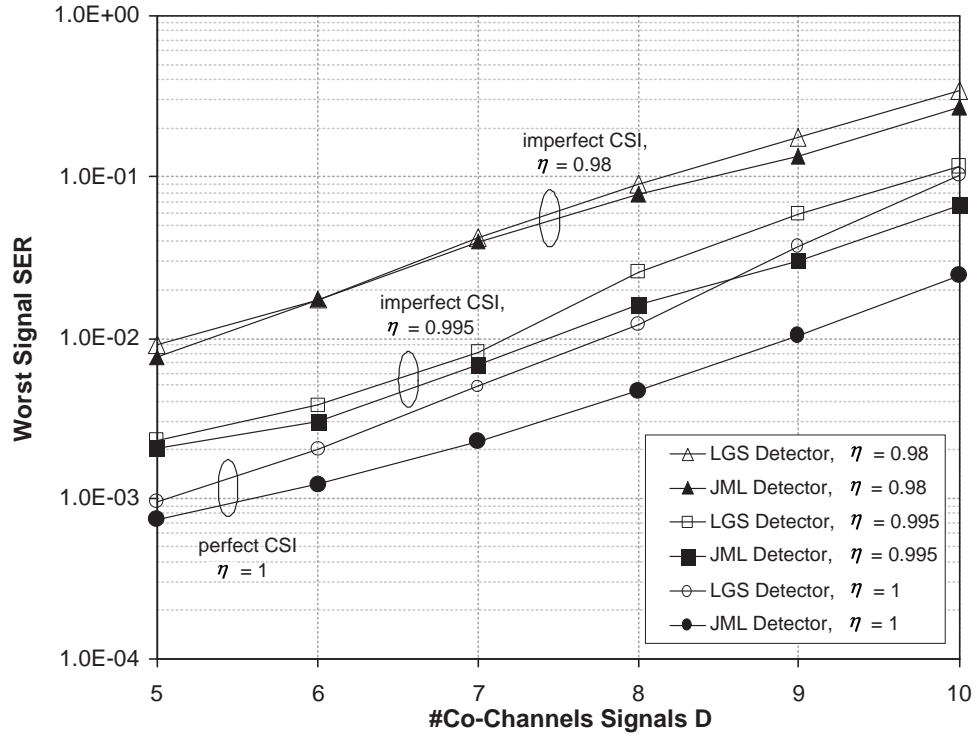


Figure 4.6 SER versus number of co-channel signals at SNR, $\Gamma = 10dB$ with perfect and imperfect CSI. The power correlation coefficient is set to $\eta = 0.98, 0.995$ and 1 (perfect CSI).

Fig. 4.7 depicts LGS simulation results for the cases of $D = 6$ ($f(D, M) = 1.5$) and 8 signals ($f(D, M) = 2$) with imperfect and perfect CSI. It can be seen that the SER is higher for higher load factors $f(D, M)$. Moreover, the error performance significantly degrades if the CSI is imperfect. This is clearly seen for $\eta = 0.98$, where the error floor is increased by more than one order of magnitude compared to the perfect CSI case ($\eta = 1$). Hence, in order to achieve good error performance in an overloaded receiver, an accurate CSI estimation process is required.

4.5 COMPLEXITY

The computational complexity of the LGS detector is measured in the number of required real squaring operations in the computation of the Euclidean distance. This is usually the most hardware intensive operation.

Analyzing the block diagram in Fig. 4.3 gives the computational complexity of the

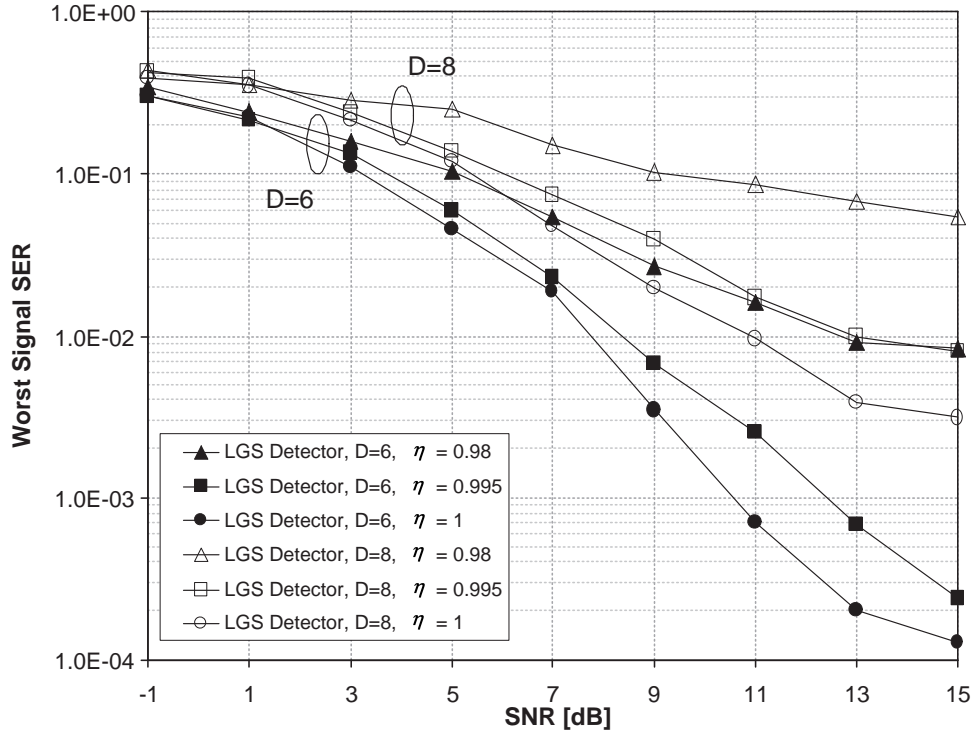


Figure 4.7 SER versus the SNR with perfect and imperfect CSI. The power correlation coefficient is set to $\eta = 0.98, 0.995$ and 1 (perfect CSI). Results are shown for $D = 6$ and 8 signals.

LGS detector as

$$C = 2 \sum_{q=1}^Q (Q_{ble} C_{ble} + C_{glo}), \quad (4.21)$$

where C_{ble} and C_{glo} denote the complexities of branch list estimation and global list optimization stages, respectively. The additional factor of 2 is introduced because computation of the Euclidean distance for complex values requires two real squaring operations. Taking into account the D individual BLE blocks in Fig. 4.3, C_{ble} can be split into individual complexities $C_{ble}[d]$. It is then computed as $C_{ble} = \sum_{d=1}^D C_{ble}[d]$, where each $C_{ble}[d]$ is given by

$$C_{ble}[d] = \Theta \sum_{j=1}^G C_{\tau_j}[d] \quad (4.22)$$

where $C_{\tau_j}[d] = |\mathcal{A}|^{|\tau_j[d]|}$ denotes the complexity of the exhaustive search over the symbols in the j th group and Θ is the number of BLE group iterations. The complexity

Table 4.6 Comparison of computational complexity for the $M = 6$ antenna receiver in Fig. 4.5.

Detector	Co-channel Signals			
	D=9	% JML	D=12	% JML
LGS Detection, $L = 2D$	$7.1E5$	23%	$3.0E6$	1%
LGS Detection, $L = 4D$	$1.0E6$	32%	$4.8E6$	2%
LGS Detection, $L = 8D$	$1.6E6$	51%	$8.2E6$	4%
JML Detection	$3.1E6$	100%	$2.0E8$	100%

of global list optimization in (4.21), C_{glo} , is obtained as

$$C_{glo} = K + \sum_{\phi=1}^{\Phi} \left(\sum_{j=1}^F K_j |\mathcal{A}|^{|v_j|} \right), \quad (4.23)$$

where K denotes the number of non-redundant input symbol vectors $\mathbf{s}_{br}^{(k)}[d] \in \mathcal{S}_{br}[d]$, K_j is the number elements in the list $\tilde{\mathcal{S}}_{search}$, $|v_j|$ is the size of the j th symbol group $|v_j|$ and Φ is the number of GLO group iterations.

Table 4.6 provides results for JML and LGS detection. The choices of the group sizes $(|\tau_j|, |v_j|)$ and the list size L determine the performance-complexity tradeoff. Small values of $(|\tau_j|, |v_j|)$ and L result in lower complexity, while larger values achieve better performance. Table 4.6 shows that for $L = 8D$ LGS detection requires only approximately 50% of the JML complexity for $D = 9$ signals and saves more than 95% for $D = 12$ signals. Complexity savings are more significant for higher numbers of receive antennas and co-channel signals.

4.6 CONCLUSIONS

In this chapter, an algorithmic structure for the separation and detection of multiple co-channel signals transmitted through a frequency-flat Rayleigh fading channel was developed. The receiver is assumed to operate under overloaded conditions with more co-channel signals than receive antennas. Detection is performed in two stages: linear preprocessing employing diversity combining and nonlinear group-wise symbol detection using the LGS detection algorithm.

The linear preprocessor performs optimum MRC diversity combining to maximize the instantaneous SNR of each individual signal. This reduces the amount of CCI. However, under overload, residual CCI is still present in the received signal vector. This must be accounted for in the detection stage.

The LGS symbol detection algorithm uses iterative processing to extract a list of the most likely symbols. This list is output by the detector and can be used by error control decoders. The detector employs parallel branch list estimators which independently search over subsets of the transmitted symbols. In each detector branch, the subsets contain the symbols with either high or low received energy. The subset with low energy represents the residual CCI which is estimated during the detection process. If a given subset exceeds a certain maximum size, it is split up into independent groups. The detector then searches over the symbol groups thereby reducing the computational complexity. The results are fed back to the detection branches.

Simulation results show that the proposed LGS detector achieves good complexity-performance tradeoffs compared to the optimum JML detector. Parallel processing makes LGS detection well suited for practical implementation.

Chapter 5

PERFORMANCE BOUNDS

A UNION bound on the performance of nonlinear suboptimum symbol detectors in frequency-flat Rayleigh fading channels is derived in this chapter. The bound is applicable to detectors that search over only a subspace of the total symbol space. These include group-wise and list-based group-wise symbol detectors such as the List Group Search (LGS) detector of Chapter 4. The error performance of such detectors under overload is limited by the Co-Channel Interference (CCI) from signals outside the current detection group. The analytical performance bound provides an approximation of the error performance without the need for simulation. Moreover, it can be used to determine detector parameters (e.g. group and list sizes) and to investigate tradeoffs among system parameters.

The chapter is organized as follows: In Section 5.1, the union bound of [13, 49] on the error performance of the optimum JML detector is summarized. In Section 5.2, a novel union bound for group-wise and list-based symbol detectors is proposed. Section 5.3 presents results and conclusions are drawn in Section 5.4.

5.1 JOINT MAXIMUM LIKELIHOOD BOUND

A wireless receiver with M antennas and D co-channel signals impinging on each antenna is considered. The signals are transmitted through a frequency-flat Rayleigh fading channel. The received signal vector $\mathbf{x} \in \mathbb{C}^M$ for this channel model was given in (2.1) as

$$\mathbf{x} = \mathbf{H}\mathbf{s} + \mathbf{n}, \quad (5.1)$$

where $\mathbf{H} \in \mathbb{C}^{M \times D}$ denotes the channel matrix, $\mathbf{s} \in \mathcal{A}^D$ is the D -dimensional transmitted symbol vector and $\mathbf{n} \in \mathbb{C}^M$ is the vector representing white Gaussian noise. A tight union bound on the performance of the optimum JML symbol detector in this channel is derived in [13, 49]. It considers the set¹ $\mathcal{S} = \{\mathbf{s}\}$ of all possible received symbol vectors $\mathbf{s} \in \mathcal{A}^D$, where \mathbf{s} is denoted $\mathbf{s} = [s_1 \ s_2 \ \dots \ s_D]$. The set \mathcal{S} is the overall search space and there are $|\mathcal{A}|^D$ vectors in \mathcal{S} . Next, the set \mathcal{S} is divided into the subset \mathcal{T} and the complementary subset $\overline{\mathcal{T}}$ such that $\mathcal{S} = \mathcal{T} \cup \overline{\mathcal{T}}$. The set $\mathcal{T} = \{\mathbf{t}_j\}$ contains the vectors $\mathbf{s} = \mathbf{t}_j$ that have the symbol $s_d^{(k)}$ as their d th element. Values for $s_d^{(k)}$ are drawn from the symbol alphabet \mathcal{A} where the superscript k denotes the k th symbol value and $k = 1, 2, \dots, |\mathcal{A}|$. There are $|\mathcal{A}|^{(D-1)}$ elements in \mathcal{T} . The complementary subset $\overline{\mathcal{T}} = \{\mathbf{t}_i\}$ contains the remaining symbol vectors $\mathbf{s} = \mathbf{t}_i$ from \mathcal{S} . Therefore, the subset $\overline{\mathcal{T}}$ has $|\mathcal{A}|^D - |\mathcal{A}|^{(D-1)}$ elements. The JML detector of (2.10) minimizes the Euclidean distance $\|\mathbf{x} - \mathbf{H}\mathbf{s}\|^2$. For the symbol vectors $\{\mathbf{t}_i\} \in \overline{\mathcal{T}}$ and $\{\mathbf{t}_j\} \in \mathcal{T}$, the Euclidean distances are denoted Λ_i and Λ_j , respectively. These are given by

$$\begin{aligned} \Lambda_i &= \|\mathbf{x} - \mathbf{H}\mathbf{t}_i\|^2 \\ &= \sum_{m=1}^M |x[m] - \mathbf{h}[m]\mathbf{t}_i|^2 \end{aligned} \quad (5.2)$$

and

$$\begin{aligned} \Lambda_j &= \|\mathbf{x} - \mathbf{H}\mathbf{t}_j\|^2 \\ &= \sum_{m=1}^M |x[m] - \mathbf{h}[m]\mathbf{t}_j|^2, \end{aligned} \quad (5.3)$$

where $x[m]$ denotes the m th element of \mathbf{x} and $\mathbf{h}[m] \in \mathbf{H}$ is the m th row vector. The detector chooses an erroneous symbol vector \mathbf{t}_i over \mathbf{t}_j when $\Delta_{ij} = \Lambda_i - \Lambda_j < 0$ [50]. In this case a detection error occurs because \mathbf{t}_j has been transmitted but \mathbf{t}_i was detected. The Euclidean distances Λ_i and Λ_j of (5.2) and (5.3) can alternatively be written as a

¹In previous chapters, \mathcal{S} is used to denote the list of L symbol vectors $\mathbf{s}^{(l)} \in \mathcal{S}$. Here, \mathcal{S} includes the total symbol space which is identical to a list that contains all $L = |\mathcal{A}|^D$ possible symbol vectors $\mathbf{s}^{(l)} \in \mathcal{S}$.

sum of M Hermitian quadratic forms [50]

$$\Lambda_i = \sum_{m=1}^M \mathbf{z}_m^H \mathbf{t}'_i \mathbf{t}'_i^T \mathbf{z}_m \quad (5.4)$$

$$\Lambda_j = \sum_{m=1}^M \mathbf{z}_m^H \mathbf{t}'_j \mathbf{t}'_j^T \mathbf{z}_m, \quad (5.5)$$

where the vectors $\mathbf{t}'_i \in \mathbb{C}^{M+1}$ and $\mathbf{t}'_j \in \mathbb{C}^{M+1}$ are defined as

$$\mathbf{t}'_i = [1 \ -\mathbf{t}_i^T]^T \quad (5.6)$$

$$\mathbf{t}'_j = [1 \ -\mathbf{t}_j^T]^T \quad (5.7)$$

and the vector $\mathbf{z}_m \in \mathbb{C}^{M+1}$ is given as

$$\mathbf{z}_m = [x[m] \ \mathbf{h}[m]]^T. \quad (5.8)$$

The difference $\Delta_{ij} = \Lambda_i - \Lambda_j$ can now be expressed as the following sum of Hermitian quadratic forms [50]

$$\Delta_{ij} = \sum_{m=1}^M \mathbf{z}_m^H \mathbf{F}_{ij} \mathbf{z}_m, \quad (5.9)$$

where the Hermitian matrix \mathbf{F}_{ij} is defined as [50]

$$\mathbf{F}_{ij} = \mathbf{t}'_i \mathbf{t}'_i{}^H - \mathbf{t}'_j \mathbf{t}'_j{}^H = \begin{pmatrix} 0 & \mathbf{t}_j^T - \mathbf{t}_i^T \\ \mathbf{t}_j^H - \mathbf{t}_i^H & \mathbf{t}_i^H \mathbf{t}_i^T - \mathbf{t}_j^H \mathbf{t}_j^T \end{pmatrix}. \quad (5.10)$$

The covariance matrix of the vector \mathbf{z}_m is given by [50]

$$\mathbf{R} = E[\mathbf{z}_m \mathbf{z}_m^H | \mathbf{t}_j] = \begin{pmatrix} \|\mathbf{t}_j\|^2 + N_0 & \mathbf{t}_j^T \\ \mathbf{t}_j^H & \mathbf{I}_M \end{pmatrix}, \quad (5.11)$$

where \mathbf{I}_M is the $M \times M$ identity matrix. The rank of the matrix $\mathbf{R}\mathbf{F}_{ij}$ is two and it has two eigenvalues, one positive and one negative [13]. These are denoted λ_{ij1} and

λ_{ij2} , respectively, and are found as [50]

$$\lambda_{ij1/2} = \frac{T \pm \sqrt{T^2 + 4N_0T}}{2}, \quad (5.12)$$

where $T = \text{trace}[\mathbf{R}\mathbf{F}_{ij}] = \|\mathbf{t}_i - \mathbf{t}_j\|$.

A union bound on the error probability P_s of the d th transmitted signal ($d = 1, 2, \dots, D$) is found by evaluating the Pairwise Error Probability (PEP) between all vectors $\{\mathbf{t}_j\} \in \mathcal{T}$ and $\{\mathbf{t}_i\} \in \bar{\mathcal{T}}$. It is computed as [13]

$$P_s \leq |\mathcal{A}|^{-D} \sum_d \sum_j \left(\sum_i P_{s_d^{(k)}, ij} \right), \quad (5.13)$$

where $P_{s_d^{(k)}, ij}$ denotes the PEP between \mathbf{t}_i and \mathbf{t}_j , given that the symbol $s_d^{(k)}$ is transmitted by the d th transmitter. The PEP is determined by [13]

$$\begin{aligned} P_{s_d^{(k)}, ij} &= P\left(\Delta_{ij} < 0 | s_d^{(k)}, \mathbf{t}_j\right) \\ &= \int_{-\infty}^0 p(\Delta_{ij}) d\Delta_{ij}, \end{aligned} \quad (5.14)$$

where $p(\Delta_{ij})$ is the probability density function (pdf) of Δ_{ij} . Its two-sided Laplace transform $\phi_{\Delta_{ij}}(s)$ is [13]

$$\phi_{\Delta_{ij}}(s) = \left[\frac{p_{ij1} p_{ij2}}{(s - p_{ij1})(s - p_{ij2})} \right]^M, \quad (5.15)$$

where $p_{ij1} = -1/\lambda_{ij1}$ and $p_{ij2} = -1/\lambda_{ij2}$ denote the poles in the left and right-half plane, respectively. Since (5.15) is similar in form to eq. (B-7) in [25], a closed-form expression for (5.14) can be derived as [13, 25]

$$P_{s_d^{(k)}, ij} = \frac{1}{\left(1 + r_{s_d^{(k)}, ij}\right)^{2M-1}} \sum_{m=0}^{M-1} \binom{2M-1}{m} \left(r_{s_d^{(k)}, ij}\right)^m, \quad (5.16)$$

where $r_{s_d^{(k)}, ij} = -\frac{p_{ij2}}{p_{ij1}}$ is the ratio of the values of the two real poles. An analytical form

for $r_{s_d^{(k)},ij}$ under the assumption of perfect CSI at the receiver can be found as [49]

$$r_{s_d^{(k)},ij} = a_{s_d^{(k)},ij} \Gamma_{s_d^{(k)}} + \sqrt{\left(a_{s_d^{(k)},ij} \Gamma_{s_d^{(k)}}\right)^2 + 2 \left(a_{s_d^{(k)},ij} \Gamma_{s_d^{(k)}}\right) + 1} \quad (5.17)$$

where $\Gamma_{s_d^{(k)}} = \frac{E_s}{N_0}$ is the SNR of the d th symbol $s_d^{(k)}$ and $a_{s_d^{(k)},ij}$ is defined as

$$a_{s_d^{(k)},ij} = \frac{\|\mathbf{t}_i - \mathbf{t}_j\|^2}{2E_s}. \quad (5.18)$$

Analytical expressions for (5.16) and (5.17) for the case of imperfect CSI are available in [49].

The computation of the union bound in (5.13) requires a search over all combinations of $\mathbf{t}_i, \mathbf{t}_j$ for all D co-channel signals. If all symbols $s_d \in \mathbf{s}$ have equal probability of occurrence, they have the same PEPs $P_{s_d^{(k)}} = P_{s^{(k)}} \forall d = 1, 2, \dots, D$. In this case (5.13) simplifies to [13]

$$P_s \leq |\mathcal{A}|^{1-D} \sum_j \left(\sum_i P_{s^{(k)},ij} \right). \quad (5.19)$$

For uncorrelated receive antennas and frequency-flat Rayleigh fading, (5.13) and (5.19) are independent of the channel matrix \mathbf{H} . If the fading statistics of the signals are correlated, as in Rician and AWGN² channels, the covariance matrix \mathbf{R} of (5.11) contains the antenna array response coefficients $a_{md} \in \mathbf{A}$. This follows from (5.11) and (5.8) since in correlated fading the channel \mathbf{H} includes the array response \mathbf{A} . For the UCA and ULA antenna geometries, \mathbf{A} is specified by (1.9) and (1.10), respectively. The matrix $\mathbf{R}\mathbf{F}_{ij}$ then has rank $2M$ and there are $2M$ eigenvalues (one positive and one negative eigenvalue per receive antenna) [51, 52].

²The AWGN channel model is given in (1.8). See, e.g. [25, 43] for a more detailed description of AWGN and Rician channels.

5.2 PERFORMANCE BOUND FOR GROUP-WISE SYMBOL DETECTORS

Group-wise symbol detection algorithms such as the LGS detector of Chapter 4 and the Iterative Multiuser Detection (IMUD) algorithm of [38, 39] attempt to reduce the search complexity by searching over only a subspace of the symbol space. The penalty is performance degradation compared to the optimum JML/ JMAP detectors.

5.2.1 Mapping and Grouping

Before deriving a performance bound for these group-wise symbol detectors, some group notation is introduced. First, a mapping operator is defined that maps the symbol vector $\mathbf{s} = [s_1 \ s_2 \ \dots \ s_D]$ into a new vector $\dot{\mathbf{s}} \in \mathcal{A}^D$, denoted $\dot{\mathbf{s}} = [\dot{s}_1 \ \dot{s}_2 \ \dots \ \dot{s}_D]$. The mapping operator is used to allow arbitrary permutations of the symbols $s_d \in \mathbf{s}$ and is denoted

$$\mathbf{s}_{(1 \times D)} \mapsto \dot{\mathbf{s}}_{(1 \times D)}. \quad (5.20)$$

Next, an arbitrary symbol group is formed by expressing $\dot{\mathbf{s}}$ in group form as

$$\dot{\mathbf{s}} = [\dot{\mathbf{s}}_g \ \dot{\mathbf{s}}_{\bar{g}}]. \quad (5.21)$$

Here, $\dot{\mathbf{s}}_g \in \mathcal{A}^G$ denotes the group symbol vector and $\dot{\mathbf{s}}_{\bar{g}} \in \mathcal{A}^{D-G}$ consists of all symbols outside the group. The vector $\dot{\mathbf{s}}_g = [\dot{s}_1 \ \dot{s}_2 \ \dots \ \dot{s}_G]$ then contains G symbols and $\dot{\mathbf{s}}_{\bar{g}} = [\dot{s}_{G+1} \ \dot{s}_{G+2} \ \dots \ \dot{s}_D]$ contains $D - G$ symbols.

Fig. 5.1 provides an example of the permutation operator (5.20) and the grouping of (5.21). The vector \mathbf{s} consists of $D = 9$ QPSK symbols, $\mathbf{s} = [s_1 \ s_2 \ \dots \ s_9]$. These are mapped into the new vector $\dot{\mathbf{s}} = [\dot{s}_1 \ \dot{s}_2 \ \dots \ \dot{s}_9]$ which is a permutation of the symbols in \mathbf{s} . The vector $\dot{\mathbf{s}}$ is then subdivided into the two vectors $\dot{\mathbf{s}}_g$ and $\dot{\mathbf{s}}_{\bar{g}}$, where $\dot{\mathbf{s}}_g$ contains $G = 3$ and $\dot{\mathbf{s}}_{\bar{g}}$ contains $D - G = 6$ symbols. In Fig. 5.1, the resulting vectors $\dot{\mathbf{s}}_g$ and $\dot{\mathbf{s}}_{\bar{g}}$ are $\dot{\mathbf{s}}_g = [(-1, -1) \ (-1, 1) \ (-1, 1)]$ and $\dot{\mathbf{s}}_{\bar{g}} = [(1, 1) \ (-1, -1) \ (-1, 1) \ (1, -1) \ (1, 1) \ (-1, -1)]$, respectively.

Many group-wise symbol detectors perform iterative processing where they form

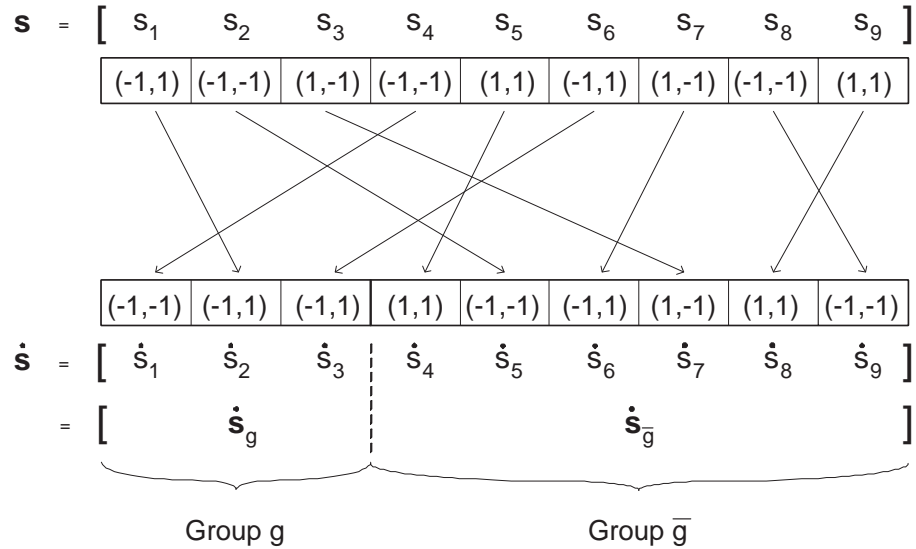


Figure 5.1 Example of mapping the QPSK vector \mathbf{s} with $D = 9$ symbols into the new vector $\dot{\mathbf{s}}$. It contains a permutation of the symbols in \mathbf{s} and is further divided into the group vectors $\dot{\mathbf{s}}_g$ and $\dot{\mathbf{s}}_{\bar{g}}$.

multiple groups to aid detection and to improve error performance. Examples are the LGS detector of Chapter 4 and the IMUD algorithm of [38, 39]. These use permutations of the symbol vector \mathbf{s} (as described by (5.20)) in each iteration and find multiple symbol groups by using various groupings (i.e. by applying (5.21) multiple times). For the LGS detector of Chapter 4, symbol groups are found by defining subsets of symbols with either *high* or *low* energy³ elements in the corresponding channel matrix \mathbf{H} . The symbols with high energy in \mathbf{H} are then further split into multiple groups. This, in fact, is a specific application of (5.20) and (5.21). The mapping and grouping must be done for each individual symbol group under detection.

5.2.2 Bound Equation

A union bound on the performance of group-wise symbol detectors is now derived. The approach is similar to the derivation of the JML union bound of (5.13).

The overall symbol space over which the optimum JML detector performs an exhaustive search is denoted \mathcal{S} . It includes a total of $|\mathcal{A}|^D$ different possible symbol combinations for the vector $\dot{\mathbf{s}}$. In case of a group-wise symbol detector, the overall

³See Section 4.2 for a detailed description.

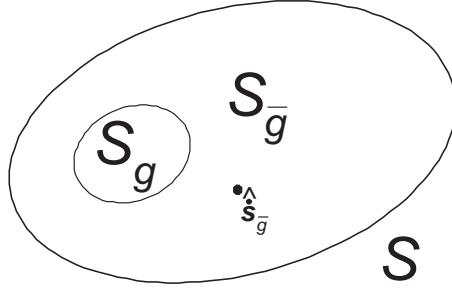


Figure 5.2 Search space of a group-wise symbol detector.

space \mathcal{S} is divided into two subspaces, denoted \mathcal{S}_g and $\mathcal{S}_{\bar{g}}$. This is illustrated in Fig. 5.2. The subspace \mathcal{S}_g contains all $|\mathcal{A}|^G$ possible symbol vectors $\{\dot{\mathbf{s}}_g\}$, whereas the subspace $\mathcal{S}_{\bar{g}}$ includes all remaining $|\mathcal{A}|^{D-G}$ symbol vectors $\{\dot{\mathbf{s}}_{\bar{g}}\}$. A group-wise symbol detector searches only over the symbols $\dot{\mathbf{s}}_g$ and thereby reduces the search complexity for this group from $|\mathcal{A}|^D$ for the optimum detector to only $|\mathcal{A}|^G$ symbol combinations. This requires knowledge of the symbols in $\dot{\mathbf{s}}_{\bar{g}}$.

Group-wise symbol detectors normally employ an estimation process to obtain an estimate of $\dot{\mathbf{s}}_{\bar{g}}$. It is denoted $\hat{\mathbf{s}}_{\bar{g}}$ and there are a total of $|\mathcal{A}|^{D-G}$ possible estimates $\hat{\mathbf{s}}_{\bar{g}} \in \mathcal{S}_{\bar{g}}$. The choice of the estimate clearly affects the performance of the group-wise detector, since symbol errors in $\hat{\mathbf{s}}_{\bar{g}}$ cause interference which degrades correct detection of the symbols in $\dot{\mathbf{s}}_g$. Here, the two subsets \mathcal{T} and $\bar{\mathcal{T}}$ are chosen differently to Section 5.1 in order to properly include the estimate $\hat{\mathbf{s}}_{\bar{g}}$. The subset $\mathcal{T}(\hat{\mathbf{s}}_{\bar{g}})$ is the set of symbol vectors $\{\dot{\mathbf{t}}_j\}$ which have the symbol $\dot{s}_d^{(k)}$ as the d th element ($d = 1, 2, \dots, G$) and the vector $\hat{\mathbf{s}}_{\bar{g}}$ as the estimate of the group symbol vector $\dot{\mathbf{s}}_{\bar{g}}$. There are $|\mathcal{A}|^{G-1}$ elements in $\{\dot{\mathbf{t}}_j\} \in \mathcal{T}(\hat{\mathbf{s}}_{\bar{g}})$. The complementary subset $\bar{\mathcal{T}}(\hat{\mathbf{s}}_{\bar{g}})$ contains the remaining vectors $\{\dot{\mathbf{t}}_i\}$, which do not have the symbol $\dot{s}_d^{(k)}$ as their d th element. The subset $\bar{\mathcal{T}}(\hat{\mathbf{s}}_{\bar{g}})$ has $|\mathcal{A}|^D - |\mathcal{A}|^{G-1}$ elements $\{\dot{\mathbf{t}}_i\} \in \bar{\mathcal{T}}(\hat{\mathbf{s}}_{\bar{g}})$.

For a group-wise detector, a union bound on the symbol error probability $P_s(\hat{\mathbf{s}}_{\bar{g}})$ of the d th signal ($d = 1, 2, \dots, G$) is computed by evaluating the PEPs between all vectors $\{\dot{\mathbf{t}}_j\} \in \mathcal{T}(\hat{\mathbf{s}}_{\bar{g}})$ and $\{\dot{\mathbf{t}}_i\} \in \bar{\mathcal{T}}(\hat{\mathbf{s}}_{\bar{g}})$ for a given estimate $\hat{\mathbf{s}}_{\bar{g}} \in \mathcal{S}_{\bar{g}}$. This is similar

in form to the JML union bound of (5.13) and is given by

$$P_s(\hat{\mathbf{s}}_{\bar{g}}) \leq |\mathcal{A}|^{-G} \sum_d \sum_j \left(\sum_i P_{\dot{s}_d^{(k)}, \hat{\mathbf{s}}_{\bar{g}}, ij} \right), \quad d = 1, 2, \dots, G, \quad (5.22)$$

where $P_{\dot{s}_d^{(k)}, \hat{\mathbf{s}}_{\bar{g}}, ij}$ denotes the PEP between \mathbf{t}_i and \mathbf{t}_j given that $\dot{s}_d^{(k)}$ is transmitted and that $\hat{\mathbf{s}}_{\bar{g}}$ is the estimate of the vector $\mathbf{s}_{\bar{g}}$. The union bound of (5.22) depends on the estimate $\hat{\mathbf{s}}_{\bar{g}}$. Any estimation errors in $\hat{\mathbf{s}}_{\bar{g}}$ result in interference and increase the error probability of a group-wise detector. However, if the estimate $\hat{\mathbf{s}}_{\bar{g}}$ is correct, then (5.22) and the JML union bound (5.13) provide the same result. The PEP $P_{\dot{s}_d^{(k)}, \hat{\mathbf{s}}_{\bar{g}}, ij}$ in (5.22) is obtained similarly to (5.16) and is given by

$$P_{\dot{s}_d^{(k)}, \hat{\mathbf{s}}_{\bar{g}}, ij} = \frac{1}{\left(1 + r_{\dot{s}_d^{(k)}, \hat{\mathbf{s}}_{\bar{g}}, ij}\right)^{2M-1}} \sum_{m=0}^{M-1} \binom{2M-1}{m} \left(r_{\dot{s}_d^{(k)}, \hat{\mathbf{s}}_{\bar{g}}, ij}\right)^m. \quad (5.23)$$

The difference between the two lies in the computation of $r_{\dot{s}_d^{(k)}, \hat{\mathbf{s}}_{\bar{g}}, ij}$ which here must consider the SINR instead of the SNR. Assuming perfect CSI at the receiver, $r_{\dot{s}_d^{(k)}, \hat{\mathbf{s}}_{\bar{g}}, ij}$ is computed as

$$r_{\dot{s}_d^{(k)}, \hat{\mathbf{s}}_{\bar{g}}, ij} = a_{\dot{s}_d^{(k)}, \hat{\mathbf{s}}_{\bar{g}}, ij} \Upsilon_{\dot{s}_d^{(k)}, \hat{\mathbf{s}}_{\bar{g}}} + \sqrt{\left(a_{\dot{s}_d^{(k)}, \hat{\mathbf{s}}_{\bar{g}}, ij} \Upsilon_{\dot{s}_d^{(k)}, \hat{\mathbf{s}}_{\bar{g}}}\right)^2 + 2\left(a_{\dot{s}_d^{(k)}, \hat{\mathbf{s}}_{\bar{g}}, ij} \Upsilon_{\dot{s}_d^{(k)}, \hat{\mathbf{s}}_{\bar{g}}}\right) + 1} \quad (5.24)$$

where

$$a_{\dot{s}_d^{(k)}, \hat{\mathbf{s}}_{\bar{g}}, ij} = \frac{\|\mathbf{t}_i - \mathbf{t}_j\|^2}{2E_s} \quad (5.25)$$

and $\Upsilon_{\dot{s}_d^{(k)}, \hat{\mathbf{s}}_{\bar{g}}}$ is the SINR for a given symbol $\dot{s}_d^{(k)}$ and estimate vector $\hat{\mathbf{s}}_{\bar{g}}$. It is defined as [53]

$$\begin{aligned} \Upsilon_{\dot{s}_d^{(k)}, \hat{\mathbf{s}}_{\bar{g}}} &= \frac{E_s}{I + N_0} \\ &= \frac{1}{\frac{I}{E_s} + \frac{N_0}{E_s}} = \frac{1}{\left(\Psi_{\hat{\mathbf{s}}_{\bar{g}}}\right)^{-1} + \left(\Gamma_{\dot{s}_d^{(k)}}\right)^{-1}}, \end{aligned} \quad (5.26)$$

where I denotes the interference energy due to symbol errors in $\hat{\mathbf{s}}_{\bar{g}}$, $\Psi_{\hat{\mathbf{s}}_{\bar{g}}}$ is the Signal to

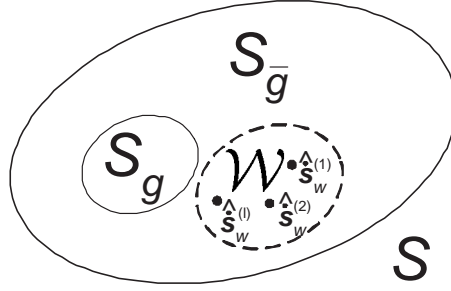


Figure 5.3 Search space of a list-based group-wise symbol detector.

Interference Ratio (SIR) and $\Gamma_{\hat{s}_d^{(k)}}$ is the SNR. If $\hat{s}_{\bar{g}}$ is error free, there is no interference ($I = 0$) and $\Upsilon_{\hat{s}_d^{(k)}, \hat{s}_{\bar{g}}} = \Gamma_{\hat{s}_d^{(k)}}$. In contrast, if the SINR is dominated by the interference the noise power can be neglected and $\Upsilon_{\hat{s}_d^{(k)}, \hat{s}_{\bar{g}}} \approx \Psi_{\hat{s}_{\bar{g}}}$. A practical estimation process will in general not be error free so that the interference must be taken into account.

5.2.3 Extension to List-based Group-wise Symbol Detectors

The union bound of (5.22) is now extended to list-based group-wise symbol detectors. This detector type considers a symbol list instead of a single vector for detecting the symbols $\hat{s}_{\bar{g}} \in \mathcal{S}_{\bar{g}}$.

Fig. 5.3 illustrates the search space \mathcal{S} for a list-based group-wise symbol detector. The space \mathcal{S} is divided into the two subspaces \mathcal{S}_g and $\mathcal{S}_{\bar{g}}$. Like all group-wise symbol detectors, a list-based group-wise detector will search only over the symbol space \mathcal{S}_g but it considers a subset of all $|\mathcal{A}|^{(D-G)}$ symbol vectors from the set $\mathcal{S}_{\bar{g}}$ instead of a single estimate. An example for this is the LGS detector of Chapter 4 where the global list optimization algorithm (cf. Table 4.2) performs group-wise detection in conjunction with a symbol list.

In Fig. 5.3, the subset of $\mathcal{S}_{\bar{g}}$ considered by the list-based group-wise detector is denoted \mathcal{W} . It is given as the L -member list of length $(D - G)$ symbol vectors $\hat{s}_w^{(l)} \in \mathcal{W}$, where $l = 1, 2, \dots, L$. While performing the group-wise symbol search, the detector combines each candidate vector $\hat{s}_g \in \mathcal{S}_g$ with each of the L symbol vectors $\hat{s}_w^{(l)} \in \mathcal{W}$. Fig. 5.4 illustrates an example of a list-based group-wise detector. There are $D = 9$ co-channel signals and the detector uses the list elements $\hat{s}_w^{(l)} \in \mathcal{W}$ as estimates of $\hat{s}_{\bar{g}}$.

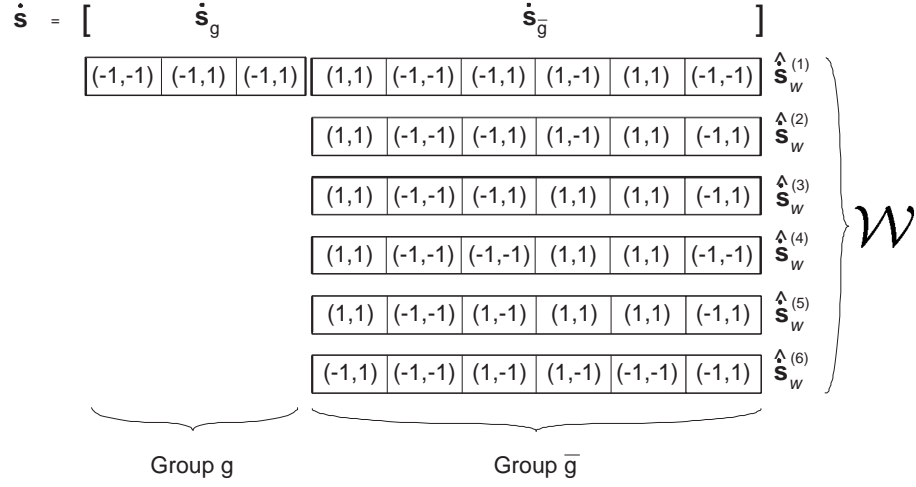


Figure 5.4 Example of a list-based group-wise symbol detector using a list \mathcal{W} with $L = 6$ elements $\hat{\mathbf{s}}_w^{(l)} \in \mathcal{W}$. Each symbol vector $\hat{\mathbf{s}}$ has $D = 9$ symbols and is further split into the two group vectors $\hat{\mathbf{s}}_g$ and $\hat{\mathbf{s}}_{\bar{g}}$. Estimates of $\hat{\mathbf{s}}_{\bar{g}}$ are represented by the list members $\hat{\mathbf{s}}_w^{(l)} \in \mathcal{W}$.

The vector $\hat{\mathbf{s}}_g$ consists of $G = 3$ symbols and each $\hat{\mathbf{s}}_w^{(l)} \in \mathcal{W}$ consists of the remaining $D - G = 6$ symbols. The list \mathcal{W} has size $L = 6$.

A list-based group-wise detector usually obtains the list \mathcal{W} through an estimation process. The resulting list contains the estimates of the symbol vector $\hat{\mathbf{s}}_{\bar{g}}$, denoted $\hat{\mathbf{s}}_w^{(l)} \in \mathcal{W}$. Moreover, the list elements $\hat{\mathbf{s}}_w^{(l)} \in \mathcal{W}$ are often ordered from most to least likely. This typically means that the elements are closely spaced. A union bound on the performance of a list-based group-wise detector is then computed by choosing

$$P_s(\mathcal{W}) = \min_l P_s(\hat{\mathbf{s}}_w^{(l)}), \quad l = 1, 2, \dots, L, \quad (5.27)$$

where $P_s(\hat{\mathbf{s}}_w^{(l)})$ is the group-wise union bound of (5.22) for a given vector $\hat{\mathbf{s}}_w^{(l)}$.

5.2.4 Bound Computation based on Mean SINR and Soft Information

The drawback of the bound of (5.22) is that it requires knowledge of the SINR for each individual estimate of the symbols $\hat{\mathbf{s}}_{\bar{g}}$. The resulting interference energy I is a non-Gaussian random variable and closed-form expressions for the exact SINR may be difficult to obtain. In practice, the SINR is often either measured or, under the assumption of sufficient independent interferers, a Gaussian approximation is used [53].

For the latter, the mean SINR is computed as

$$\Upsilon_{s_d^{(k)}} = \frac{\sigma_s^2}{\sigma_I^2 + \sigma_n^2}, \quad (5.28)$$

where σ_s^2 denotes the average received power per signal, σ_I^2 is the average interference power and σ_n^2 is the average noise power.

The SINR of a group-wise detector is determined by the estimate $\hat{\mathbf{s}}_{\bar{g}} \in \mathcal{S}_{\bar{g}}$. If the mean SINR is considered, then the union bound (5.22) must be computed for a symbol vector $\hat{\mathbf{s}}_{\bar{g}}$ that would result in that particular mean SINR. This can be done by assuming *soft values* for the bits of the symbols in $\hat{\mathbf{s}}_{\bar{g}}$. Instead of only the two values ± 1 , each “soft” bit can take values ranging from -1 to 1 . The symbol vector containing the “soft” bit values is denoted $\underline{\hat{\mathbf{s}}}_{\bar{g}}$. Hence, the symbol spaces \mathcal{S}_g and $\mathcal{S}_{\bar{g}}$ now contain the “soft” symbol vectors $\underline{\hat{\mathbf{s}}}_g \in \underline{\mathcal{S}}_g$ and $\underline{\hat{\mathbf{s}}}_{\bar{g}} \in \underline{\mathcal{S}}_{\bar{g}}$, respectively. Similarly, the sets $\mathcal{T}(\hat{\mathbf{s}}_{\bar{g}})$ and $\overline{\mathcal{T}}(\hat{\mathbf{s}}_{\bar{g}})$ will be denoted $\mathcal{T}(\underline{\hat{\mathbf{s}}}_{\bar{g}})$ and $\overline{\mathcal{T}}(\underline{\hat{\mathbf{s}}}_{\bar{g}})$, respectively. Computation of the union bound (5.22) requires evaluation of complementary bit values for the vectors $\underline{\hat{\mathbf{s}}}_{\bar{g}}$ considered in the two subsets $\mathcal{T}(\underline{\hat{\mathbf{s}}}_{\bar{g}})$ and $\overline{\mathcal{T}}(\underline{\hat{\mathbf{s}}}_{\bar{g}})$. This can be done in terms of a distance measure which is defined as

$$\delta_c = |\underline{b}_i - \underline{b}_j|, \quad (5.29)$$

where $\underline{b}_i = -\underline{b}_j$ are complementary “soft” bit values so that $\delta_c = 2|\underline{b}_i| = 2|\underline{b}_j|$.

Next, three scenarios for δ_c in group-wise and list-based group-wise symbol detectors are discussed. These are distinguished by different sizes of the list \mathcal{W} . The list \mathcal{W} contains the L vectors $\hat{\mathbf{s}}_w^{(l)} \in \mathcal{W}$ of length $(D - G)$ as the estimates of $\hat{\mathbf{s}}_{\bar{g}}$.

List size $L = 0$: This is the case of a group-wise symbol detector with no knowledge of the symbols $\hat{\mathbf{s}}_{\bar{g}} \in \mathcal{S}_{\bar{g}}$. Here, the detector uses only a single estimate $\hat{\mathbf{s}}_{\bar{g}} \in \mathcal{S}_{\bar{g}}$. The mean SINR results from different (unknown) vectors $\hat{\mathbf{s}}_{\bar{g}}$ and the SINR is averaged over multiple symbol periods. Each “soft” bit in $\underline{\hat{\mathbf{s}}}_{\bar{g}} \in \underline{\mathcal{S}}_{\bar{g}}$ has value ‘0’ indicating that the detector does not know its value. The distance between two complementary bit values is $\delta_c = 0$ so that $\underline{\hat{\mathbf{s}}}_{\bar{g}} = \mathbf{0}$. The union bound on the error

probability of a group-wise detector can now be obtained using the mean SINR of (5.28) together with $\hat{\underline{\mathbf{s}}}_{\overline{\mathcal{G}}} = \mathbf{0}$ in (5.22).

List size $L = |\mathcal{A}|^{D-G}$: A list-based group-wise detector which uses a list \mathcal{W} with $L = |\mathcal{A}|^{D-G}$ elements $\hat{\underline{\mathbf{s}}}_{\overline{\mathcal{G}}}^{(l)} \in \mathcal{W}$ effectively performs an exhaustive search over all possible values⁴ of $\underline{\mathbf{s}}_{\overline{\mathcal{G}}}$. As a result, since the correct vector $\underline{\mathbf{s}}_{\overline{\mathcal{G}}}$ is always considered, it follows that the interference energy $I = 0$ and $\Upsilon_{s_d^{(k)}} = \Gamma_{\hat{s}_d^{(k)}}$. The distance between two complementary bit values is $\delta_c = 2$. The union bound is given by (5.27). This is identical to computing (5.22) with the correct estimate $\hat{\underline{\mathbf{s}}}_{\overline{\mathcal{G}}} = \underline{\mathbf{s}}_{\overline{\mathcal{G}}}$. The resulting error probability is identical to the union bound of the optimum JML detector.

List size $0 < L < |\mathcal{A}|^{D-G}$: For a list-based group-wise detector, the list \mathcal{W} typically has size $0 < L < |\mathcal{A}|^{D-G}$. The detector considers a limited number⁵ of vectors $\hat{\underline{\mathbf{s}}}_w^{(l)} \in \mathcal{W}$ as the estimates of $\underline{\mathbf{s}}_{\overline{\mathcal{G}}}$. This causes interference if the correct vector $\underline{\mathbf{s}}_{\overline{\mathcal{G}}}$ is not included in \mathcal{W} . The mean SINR and the corresponding “soft” symbol vector $\underline{\hat{\mathbf{s}}}_{\overline{\mathcal{G}}}$ depend on the list size L . If L is large, the probability that the correct vector $\underline{\mathbf{s}}_{\overline{\mathcal{G}}}$ is included in \mathcal{W} is high. In contrast, for small values of L , this probability may be low. The result is a variable distance δ_c with $0 < \delta_c < 2$. The value δ_c can be determined by measuring the probability $Pr(\underline{\mathbf{s}}_{\overline{\mathcal{G}}} \in \mathcal{W})$ that the correct vector $\underline{\mathbf{s}}_{\overline{\mathcal{G}}}$ is included in \mathcal{W} . Hence, the distance is obtained by

$$\begin{aligned} \delta_c &= 2Pr(\underline{\mathbf{s}}_{\overline{\mathcal{G}}} \in \mathcal{W}) \\ &= 2 \frac{N(\underline{\mathbf{s}}_{\overline{\mathcal{G}}} \in \mathcal{W})}{k}, \end{aligned} \quad (5.30)$$

with $N(\underline{\mathbf{s}}_{\overline{\mathcal{G}}} \in \mathcal{W})$ denoting the number of events where $\underline{\mathbf{s}}_{\overline{\mathcal{G}}} \in \mathcal{W}$ and k is the number of symbol periods considered. The union bound is determined by computing (5.22) using the mean SINR of (5.28) together with an arbitrary vector $\hat{\underline{\mathbf{s}}}_{\overline{\mathcal{G}}}$.

⁴This requires that all possible symbol combinations are included in the list \mathcal{W} .

⁵The general group-wise detector that uses the estimate $\hat{\underline{\mathbf{s}}}_{\overline{\mathcal{G}}}$ is included here. In this case, the list size is $L = 1$.

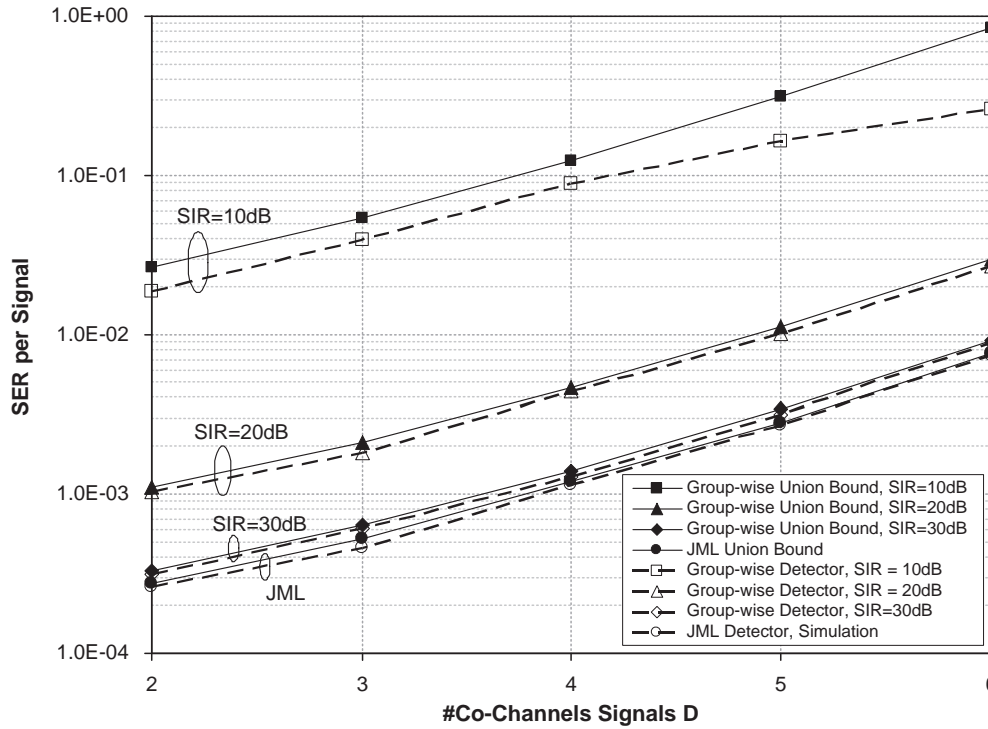


Figure 5.5 SER of a group-wise symbol detector versus the number of co-channel signals D for a $M = 2$ antenna receiver and various SIR. The SNR is set to $\Gamma = 20dB$. Union bounds are shown by a solid line and simulation by a dashed line.

5.3 RESULTS

This section provides calculated results for the proposed performance bounds in Section 5.2. Detector performance is evaluated in terms of the SER per transmitted signal. The signals considered are equal-energy QPSK signals which are transmitted through a frequency-flat Rayleigh fading channel. Results are obtained from (5.13) for JML, from (5.22) for group-wise and from (5.27) for list-based group-wise detectors. These are compared with the simulation results.

Fig. 5.5 depicts SER curves for a receiver with $M = 2$ antennas and different numbers of co-channel signals D . The SNR at each antenna is assumed to be $\Gamma = 20dB$ and the SIR is set to $\Psi = 10, 20$ and $30dB$. If desired, the SINR can be obtained from the SNR and SIR values using (5.26). Symbol detection is performed using either JML or group-wise detection. The simulation of the group-wise symbol detector first obtains

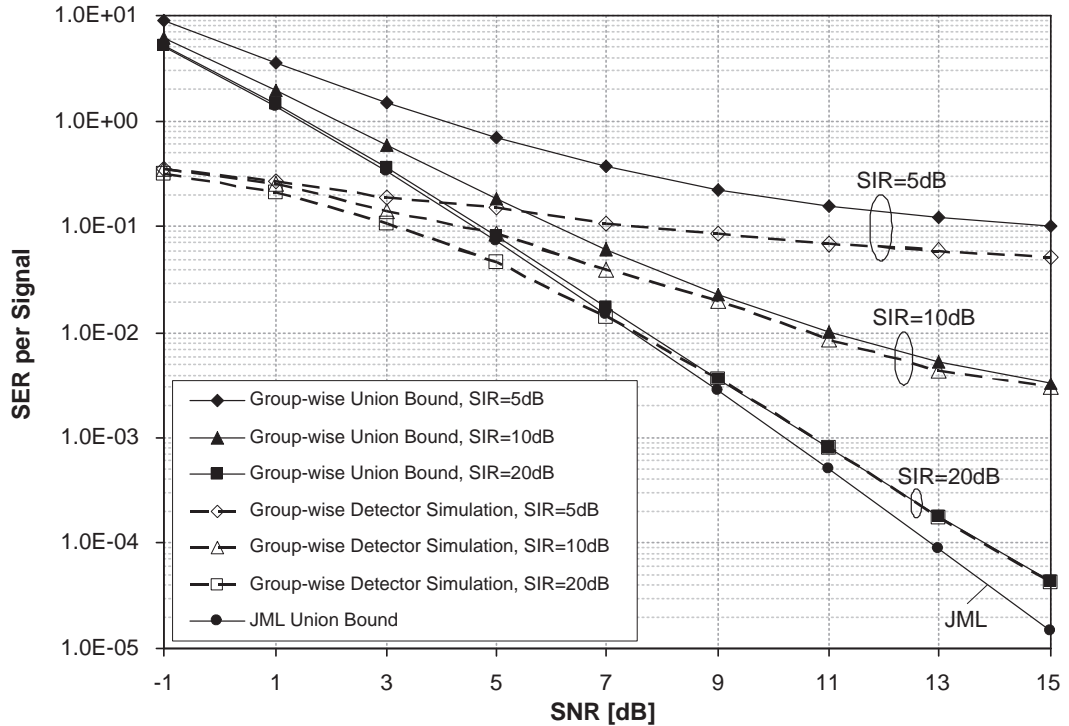


Figure 5.6 SER versus SNR for an $M = 4$ antenna receiver with $D = 6$ co-channel signals and various SIR values. Solid lines indicate bounds and dashed lines show simulation results.

the JML solution. This is used as the estimate⁶ for the symbols $\hat{\mathbf{s}}_{\bar{g}} \in \mathcal{S}_{\bar{g}}$ outside the detection group. The interference resulting from symbol errors in the estimate $\hat{\mathbf{s}}_{\bar{g}}$ is given in terms of the SIR value. It is added as additional AWGN. Using the resulting estimate $\hat{\mathbf{s}}_{\bar{g}} \in \mathcal{S}_{\bar{g}}$, the group-wise detector searches over the symbols in $\mathbf{s}_g \in \mathcal{S}_g$.

From Fig. 5.5 it is obvious that the JML detector achieves optimum performance. The SER almost linearly increases with the number of co-channel signals D . It is further obvious that the interference causes an upshift of the SER curves. The computed bounds are tight at high SINR but rather loose for low SINR values. This is expected because in [13], a similar dependency was observed for the JML union bound and different SNR values.

Fig. 5.6 illustrates the SER at different SNR for a receiver with an $M = 4$ antenna array and $D = 6$ equal-energy QPSK signals. Results are shown for different SIR values. Again, the computed performance bounds are tight in the high SNR region.

⁶The exhaustive search represents an ideal estimation process for the symbols $\mathbf{s}_{\bar{g}} \in \mathcal{S}_{\bar{g}}$.

Table 5.1 Simulation parameters for the group-wise LGS detector in Fig. 5.7.

SEAIR threshold	2	List size L (for \mathcal{S} and $\mathcal{S}_{br}[d]$)	1 (group-wise)
SSSER threshold	0.1	BLE group iterations Θ	3
Receive antennas M	4	BLE iterations Q_{BLE}	3
Co-channel signals D	6	GLO group iterations Φ	1
BLE group size $ \tau_j $	4	Overall iterations Q	1
GLO group size $ v_j $	3	Symbol errors	100

Table 5.2 Simulation parameters for the list-based group-wise LGS detector in Fig. 5.7.

SEAIR threshold	2	List size L (for \mathcal{S} and $\mathcal{S}_{br}[d]$)	24 and 64
SSSER threshold	0.1	BLE group iterations Θ	3
Receive antennas M	4	BLE iterations Q_{BLE}	3
Co-channel signals D	6	GLO group iterations Φ	1
BLE group size $ \tau_j $	3	Overall iterations Q	1
GLO group size $ v_j $	3	Symbol errors	100

It can further be seen that for constant SIR an error floor occurs. The error floor is higher for small SIR values. This means the overall performance is limited by the interference that is caused by symbol errors in the vector $\hat{\mathbf{s}}_{\bar{g}} \in \mathcal{S}_{\bar{g}}$. For example, if at SNR $\Gamma = 11dB$ the desired SER is $< 10^{-3}$, an approximate SIR of $\Psi \geq 20dB$ is required for the estimate $\hat{\mathbf{s}}_{\bar{g}}$.

In Fig. 5.7, union bounds on the error probability of the LGS detector of Chapter 4 are computed and compared with simulation. The LGS detector is used here as an example of group-wise and list-based group-wise symbol detectors. Tables 5.1 and 5.2 show the LGS simulation parameters. The union bounds are obtained from (5.22) using the mean SINR. This is measured by the detector by summing over

$$\begin{aligned}
\Upsilon_{s_d} &= \frac{\sigma_s^2}{\sigma_I^2 + \sigma_z^2} \\
&= \frac{\sum_k |\mathbf{h}[d]_{s_d}|^2}{\sum_k \|\mathbf{y} - \mathbf{H}\hat{\mathbf{s}}_{SINR}\|^2},
\end{aligned} \tag{5.31}$$

where k is the number of symbol periods considered. The numerator in (5.31) denotes the average energy of the d th signal and the denominator is the average interference

Table 5.3 Measured SINR values of the group-wise LGS detector of Table 5.1 (list size $L = 1$) and the list-based group-wise LGS detector of Table 5.2 (list sizes $L = 24$ and $L = 64$).

SINR Γ	-1	1	3	5	7	9	11	13	15	17
$L = 1, \delta_c$	0.80	0.91	1.08	1.15	1.20	1.22	1.23	1.30	1.36	1.41
$L = 1, \Upsilon_{s_d}$ [dB]	-4.3	-3.7	-3.0	-2.8	-2.6	-2.2	-1.7	-1.3	-0.7	0.0
$L = 24, \delta_c$	1.96	1.96	1.99	1.99	1.99	1.99	1.99	1.99	2.00	2.00
$L = 24, \Upsilon_{s_d}$ [dB]	-2.4	-1.0	1.4	3.2	5.2	6.8	8.1	9.1	9.8	10.1
$L = 64, \delta_c$	2.00	2.00	2.00	2.00	2.00	2.00	2.00	2.00	2.00	2.00
$L = 64, \Upsilon_{s_d}$ [dB]	-2.1	-0.4	1.6	3.8	6.1	8.1	9.7	11.1	12.4	13.3

plus noise energy. The symbol vector $\hat{\mathbf{s}}_{SINR}$ includes the “soft” symbols from the estimate $\hat{\mathbf{s}}_{\underline{g}} \in \underline{\mathcal{S}}_{\underline{g}}$ and the transmit symbols for $\mathbf{s}_{\underline{g}} \in \mathcal{S}_{\underline{g}}$. The SINR values for LGS detection are shown in Table 5.3.

From Fig. 5.7 it can be seen that for high SINR values the union bound approximates simulation results. The bound is loose in the low SINR region. This is clearly seen for group-wise LGS detection (list size $L = 1$). In contrast, for $L = 24$ and $L = 64$ an error floor occurs in the LGS results. The floor is lowered for larger list sizes until eventually optimum performance is achieved. This occurs when the list \mathcal{W} includes all possible $|\mathcal{A}|^{D-G}$ estimates for $\mathbf{s}_{\underline{g}} \in \mathcal{S}_{\underline{g}}$. The error probability is approximated by the union bound for sufficiently high SINR values.

5.4 CONCLUSIONS

In this chapter, a union bound on the error probability of suboptimum group-wise and list-based group-wise detectors was developed. The bound considers the interference caused by estimation errors of the symbols outside the detected group. It is used to determine the error floor resulting from the estimation errors, e.g. due to small list sizes. The computation requires knowledge of the SINR. Comparison of the bound with simulation shows that, if the exact SINR value is known, the bound is tight in the high SINR region. If the mean SINR is used the bound approximates the performance of practical detectors such as the LGS detector.

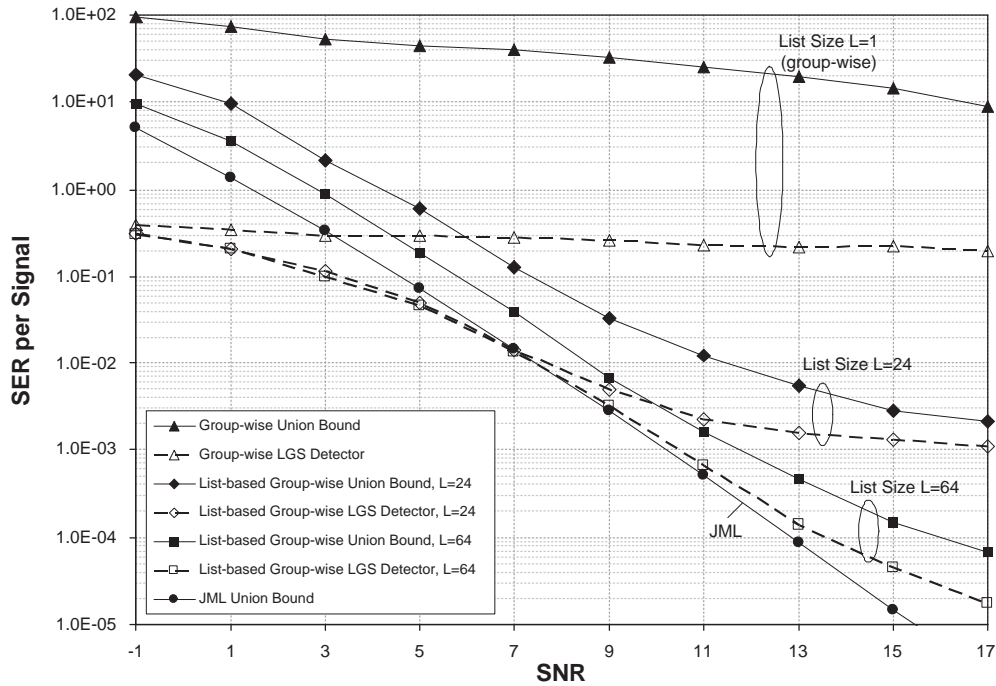


Figure 5.7 SER of the LGS detector versus SNR for an $M = 4$ antenna receiver with $D = 6$ co-channel signals. Union bounds are shown by a solid line and LGS simulation results by a dashed line.

The union bound provides a means of determining detection parameters such as group-size and required mean SINR in order to achieve a desired SER. This is important when specifying an interference estimation process for symbol detectors that work under overload. The results can be extended to the case of imperfect CSI at the receiver and to correlated receive antennas.

Chapter 6

CONCLUSIONS AND FUTURE WORK

THE THESIS develops a framework for the separation and detection of multiple co-channel signals in overloaded receivers having multiple antennas. It proposes novel receiver structures and symbol detection algorithms. In addition, it develops performance bounds. This chapter is organized as follows: Conclusions on the presented work are drawn in Section 6.1. In Section 6.2, areas for future research are described.

6.1 CONCLUSIONS

A unified algorithmic structure for the separation and detection of multiple co-channel signals in overloaded receivers is proposed in Chapter 3. The system model assumes an AWGN channel with LOS links between the multiple transmitters and the receive antenna array. Signal separation and symbol detection at the receiver are performed in two stages. First, a linear preprocessor employs either a beamformer or a diversity combiner to reduce CCI. Under overload significant amounts of residual CCI are still present in the preprocessed signal. The preprocessor is followed by a symbol detection stage. It estimates the residual CCI and performs nonlinear iterative list detection of the user symbols. This is done by the proposed Parallel Detection with Interference Estimation (PD-IE) algorithm. Simulation results show that PD-IE approximates optimum JML detection with significantly lower complexity and outperforms existing low-complexity algorithms. The joint detection of both data symbols and residual CCI estimation achieves better performance-complexity tradeoffs than explicit CCI estima-

tion and symbol detection. PD-IE has a parallel processing structure and is well-suited for practical implementation.

Chapter 4 addresses the problem of signal separation and symbol detection in a frequency-flat Rayleigh fading channel. This is also done using a two stage process. The receiver employs a diversity combiner at the preprocessor stage. This can only reduce the amount of CCI in the overloaded case but cannot cancel it. Since significant amounts of residual CCI are present in the preprocessed signal, it must be estimated by the symbol detector. The proposed List Group Search (LGS) detection algorithm performs nonlinear iterative group-wise symbol detection. It has a parallel processing structure and splits up the data symbols into several groups. The detector then searches over only the symbols of each group thereby reducing the overall complexity. Simulation results show that the LGS detector provides good complexity-performance tradeoffs at lower complexity than JML. The proposed receiver structure can outperform existing reduced-complexity detection techniques at the cost of higher complexity.

A union bound on the performance of group-wise and list-based group-wise symbol detectors is proposed in Chapter 5. The main idea is that detection errors of the symbols outside the current group cause additional CCI which degrades the performance of the detector. The exact SINR must be considered in the bound computation. If the exact SINR is not available, the mean SINR must be either measured or computed using approximation. In this case, soft information is assumed for the symbols outside the current group. The proposed bound is tight in the high SINR region. Its computation predicts the detector performance without the need for simulation. This is useful in order to find suitable detector parameters. In addition, the bound can be used to determine the detector error floor and thus, the required output SINR of the interference estimation process in an overloaded receiver.

6.2 FUTURE WORK

This section proposes further optimizations of the algorithms developed in this thesis and defines various possible future research projects.

6.2.1 Further Optimizations

Future work on the signal separation and symbol detection approaches in Chapters 3 and 4 of this thesis should focus on the optimization of both preprocessor and symbol detection stages. Some suggestions are presented below.

Derivation of the Sparsity Matrix

The linear preprocessors considered in Chapters 3 and 4 derive a so-called sparsity matrix from the channel matrix. It is based on differences in the channel energies, which allow the formation of symbol subsets with either high or low energy in the corresponding channel matrix. The PD-IE and LGS algorithms use these subsets to reduce the complexity by searching only over the subsets with high energy. Currently, it is not known how the performance and complexity are affected by the structure of the sparsity matrix. Moreover, it is not clear how an optimum sparsity matrix is derived. In this thesis an empirical approach is used based on the SSSER and SEAIR criteria. Future optimizations should investigate different derivations and their effects on detector design as well as resulting complexity-performance tradeoffs.

Design of the Feedback List

Both PD-IE and LGS algorithms compute a list of likely symbol estimates. This is fed back to the detector input to iteratively obtain an improved symbol list. The elements in the feedback list are ordered from most to least likely. Often the list elements are distinguished by only a few bit differences. This means that the symbol list contains redundant information. The detection performance could thus be improved by designing the feedback list differently, e.g. using the most likely symbols together with less likely symbol estimates. The complexity can be reduced by using soft information instead of symbol lists. This may however degrade the error performance because the joint probabilities of multiple symbols are often not available when soft information is used. The joint probabilities are implicitly contained in the symbol lists.

Message Passing between Groups in Group-wise Symbol Detectors

The proposed LGS symbol detector in Chapter 4 divides the symbol subsets into several symbol groups. It then independently searches over the symbols of each group. This effectively reduces the search complexity but can result in performance degradation. This is caused by the significantly reduced search space used for each subset. The performance of a group-wise symbol detector can be improved by linking or message passing between the different groups. Future work should concentrate on finding appropriate link metrics/ message passing information and on optimizing the performance-complexity tradeoffs.

6.2.2 Frequency-Selective Fading Channels

The thesis considers signal separation and symbol detection in AWGN and frequency-flat Rayleigh fading channels. It is possible to extend this work to frequency-selective fading channels. This channel is commonly modelled as the response of a FIR filter. It has multiple channel taps in which signal separation and symbol detection must be performed. This leads to significant complexity increases and may require further complexity reductions as well as novel low-complexity approaches to the signal separation and detection problem in overloaded receivers.

6.2.3 Joint Channel Estimation and Symbol Detection

Most wireless receivers require a channel estimation process to obtain estimates of the channel matrix. In this thesis it is assumed that the receiver has perfect CSI. The case of imperfect CSI is simply modelled by adding AWGN to the channel matrix. Channel estimation is often based on training symbols and may require a computationally complex algorithm. The joint design of a channel estimator and symbol detector that works under overload may provide lower overall complexity and better performance than the two individual processes. Moreover, such an approach would be well suited for practical application.

6.2.4 Error Control Coding

Practical wireless communication systems use error control coding to encode the transmit data. This significantly improves the detection performance. The performance of different error control codes in conjunction with the proposed signal separation and symbol detection algorithms should be investigated.

6.2.5 Multiuser MIMO Systems

The thesis assumes multiple independent co-channel signals incident on a receiver with an antenna array. It is possible to extend this work to wireless communication systems with multiple transmit nodes, each equipped with multiple transmit antennas. Such systems are referred to as multiuser MIMO systems. The transmit nodes are often assumed independent with sufficient spatial separation. This is in contrast to the multiple co-channel signals originating from the same transmit node. Their signals may be correlated, since the antennas of the same transmit node are normally spaced at a relatively close distance.

The signal separation and symbol detection algorithms proposed in Chapters 3 and 4 can be used in multiuser MIMO systems. However, it would be beneficial to adapt the algorithms to this scenario. For example, the preprocessor could be used to reduce CCI between interfering co-channel users. This would affect the resulting sparsity matrix and may require novel grouping strategies in the symbol detector. A multiuser MIMO system should also employ a space-time encoder at each transmit node to achieve additional coding and/or diversity gain. The result would be a further improvement of each user's error performance.

6.2.6 Space-Time Coding

It has been shown that space-time codes can increase the data rate and reliability of data transfer by exploiting the space and time domains [30]. For example, space-time trellis codes are known to provide both coding and diversity gains. The performance

of different space-time codes in overloaded communication systems needs to be investigated. This could lead to a new code design that is specifically suited to overloaded systems.

6.2.7 Performance Bounds

The performance bound in Chapter 5 provides results for group-wise and list-based group-wise detectors in a frequency-flat Rayleigh fading channel.

It is possible to extend the proposed bound to detectors that operate in an AWGN channel. This channel introduces correlation between the received signal replicas. The work of [51, 52] extends the JML union bound to AWGN channels. The extension of the proposed bound in Chapter 5 would be analogue. In addition, the case of imperfect CSI at the receiver should also be considered. In [13, 50], this was done for the JML union bound.

BIBLIOGRAPHY

- [1] J.-A. Tsai, R. M. Buehrer, and B. D. Woerner, "BER performance of a uniform circular array versus a uniform linear array in a mobile radio environment," *IEEE Trans. Wireless Commun.*, vol. 3, pp. 695-700, May 2004.
- [2] R. Monzingo and T. Miller, "Introduction to Adaptive Arrays," *New York: Wiley*, 1980.
- [3] M. J. Colella, J. N. Martin and F. Akyildiz, "The halo network", *IEEE Commun. Mag.*, vol. 38, pp. 142-148, June 2000.
- [4] J. Litva and T. K. Lo, "Digital Beamforming in Wireless Communications," *Boston, MA: Artech House*, 1996.
- [5] T. S. Rappaport, "Wireless Communications: Principles and Practice," *Prentice Hall*, 1996.
- [6] B. Sklar, "Rayleigh fading channels in mobile digital communication systems part I: characterization," *IEEE Communications Magazine*, July 1997.
- [7] B. Sklar, "Rayleigh fading channels in mobile digital communication systems part II: mitigation," *IEEE Communications Magazine*, July 1997.
- [8] H. Bölcskei, D. Gesbert, C. B. Papadias, and A.-J. van der Veen, "Space-Time Wireless Systems: From Array Processing to MIMO Communications," *Cambridge University Press*, 2006.
- [9] M. K. Simon and M.-S. Alouini, "Digital Communication over Fading Channels: A Unified Approach to Performance Analysis," *John Wiley & Sons*, 2000.

- [10] G. Forney, "Maximum-Likelihood sequence estimation of digital sequences in the presence of intersymbol interference", *IEEE Trans. Inform. Theory*, vol. 18, pp. 363-378, May 1972.
- [11] A. J. Viterbi, "Error bounds for convolutional codes and an asymptotically optimum decoding algorithm", *IEEE Trans. Inform. Theory*, vol. IT-13, pp. 260-269, Apr 1967.
- [12] B. M. Hochwald and S. ten Brink, "Achieving near-capacity on a multiple-antenna channel", *IEEE Trans. Commun.*, vol. 51, pp. 389-399, March 2003.
- [13] S. J. Grant and J. K. Cavers, "Performance enhancement through joint detection of cochannel signals using diversity arrays," *IEEE Trans. Commun.*, Vol. 46, Issue 8, pp. 1038 - 1049, Aug. 1998.
- [14] S. Talwar, M. Viberg and A. Paulraj, "Blind separation of synchronous co-channel digital signals using an antenna array—Part I: Algorithms," *IEEE Trans. Signal Processing*, vol. 44., pp. 1184-1197, May 1996.
- [15] S. Talwar and A. Paulraj, "Blind separation of synchronous co-channel digital signals using an antenna array—Part II: Performance Analysis," *IEEE Trans. Signal Processing*, vol. 45., pp. 706-718, Mar. 1997.
- [16] S. Bayram, J. Hicks, R. J. Boyle and J. H. Reed, "Overloaded array processing in wireless airborne communication systems," in *Proc. MILCOM*, pp. 24-29, Los Angeles, CA, Oct. 2000.
- [17] S. Bayram, J. Hicks, R. J. Boyle and J. H. Reed, "Joint ML approach in overloaded array processing," in *Proc. VTC*, Boston, MA, vol. 1., pp. 394-400, Sep. 2000.
- [18] J. Hagenauer, E. Offer, and L. Papke, "Iterative decoding of binary and block convolutional codes," *IEEE Trans. Inform. Theory*, vol. 42, pp. 429-445, Mar. 1996.
- [19] J. Hagenauer and C. Kuhn, "The list-sequential (LISS) algorithm and its application," *IEEE Trans. on Commun.*, vol. 55, pp. 918-928, May 2007.

- [20] J. R. Barry, E. A. Lee, D. G. Messerschmitt, "Digital Communication," *Springer*, 2004.
- [21] B. Hassibi and H. Vikalo, "Maximum-Likelihood decoding and integer least-squares: the expected complexity," in *Multiantenna Channels: Capacity, Coding and Signal Processing*, J. Foschini and S. Verdu, Eds., American Mathematical Society, 2003.
- [22] J. Hicks, S. Bayram, W. H. Tranter, R. J. Boyle and J. H. Reed, "Overloaded array processing with spatially reduced search joint detection," *IEEE J. Sel. Areas Commun.*, vol. 19, no. 8, pp. 1584-1593, Aug. 2001.
- [23] M. Grotscchel, L. Lovasz and A. Schriver, "Geometric Algorithms and Combinatorial Optimization," *Springer Verlag*, 2nd ed., 1993.
- [24] M. Ajtai, "The shortest vector problem in L_2 is NP-hard for randomized reductions," in *Proc. 30th Annual ACM Symposium on Theory of Computing*, pp. 10-19, 1998.
- [25] J. G. Proakis, "Digital Communications," *McGraw Hill*, 4th ed., NY, 2001.
- [26] S. S. Haykin, "Adaptive Filter Theory," *Prentice-Hall*, 4th ed., NJ, 2002.
- [27] G. H. Golub and C. F. Van Loan, "Matrix Computations," *John Hopkins University Press*, 3rd ed., Baltimore, MD, 1996.
- [28] S. Verdu, "Multiuser Detection," *Cambridge University Press*, Cambridge, UK, 1998.
- [29] H. Vikalo, "Sphere Decoding Algorithms for Digital Communications," *PhD Thesis*, Stanford University, 2003.
- [30] B. Vucetic and J. Yuan, "Space-Time Coding," *Wiley*, 2003.
- [31] J. Tsai, J. Hicks, and B. D. Woerner, "Joint MMSE beamforming with SIC for an overloaded array system," in *Proc. MILCOM*, pp. 1261-1265, Washington D.C, Oct. 2001.

- [32] J. E. Hicks, J. Tsai, J. H. Reed, W. H. Tranter, and B. D. Woerner, "Overloaded array processing with MMSE-SIC," in *Proc. VTC*, pp. 542-546, Birmingham, AL, May 2002.
- [33] X. Wang, H. V. Poor, "Wireless Communication Systems," *Prentice Hall*, 2004.
- [34] B. Pelletier and B. Champagne, "Multistage MMSE PIC space-time receiver with non-mutually exclusive grouping," *IEEE Trans. Veh. Techn.*, pp. 2070-2070, Jul. 2008.
- [35] W. M. Tam, F. C. M. Lau and C. K. Tse, "Digital Communications With Chaos: Multiple Access Techniques And Performance," *Elsevier*, 2007.
- [36] J. A. Tsai, J. Tsai and B. D. Woerner, "Performance of combined MMSE beamforming with parallel interference cancellation for overloaded OFDM-CDMA systems," in *in Proc. MILCOM*, vol. 1, pp. 748-752, Anaheim, Calif, USA, Oct. 2002.
- [37] A. Duel-Hallen, C. Heegard, "Delayed decision-feedback sequence estimation," *IEEE Trans. Commun.*, vol. 37, no. 5, pp. 428 - 436, May 1989.
- [38] B. W. Zarikoff, J. K. Cavers and S. Bavarian, "An iterative groupwise multiuser detector for overloaded MIMO applications," *IEEE Trans. Wireless Commun.*, vol. 6, pp. 443-447, Feb. 2007.
- [39] B. W. Zarikoff, "Investigation of an iterative groupwise soft input/ soft output multiuser detection algorithm," *Master of Science Thesis*, Simon Fraser University, Vancouver, Canada, Jun. 2004.
- [40] A. Paulraj and C. Papadias, "Space-Time processing for wireless communications," *IEEE Signal Processing Mag.*, vol. 14, pp. 49-83, Nov. 1997.
- [41] D. Brennan, "Linear diversity combining techniques," in *Proc. IRE*, vol. 47, no. 1, pp. 1075-1102, Jun. 1959.
- [42] F. Alam, "Space time processing for third generation CDMA systems," *PhD dissertation*, Virginia Tech, USA, Nov. 2002.

- [43] S. S. Haykin, "Communication Systems," *John Wiley & Sons*, 4th ed., New York, NY, USA, 2001.
- [44] W. L. Stutzmann and G. A. Thiele, *Antenna Theory and Design*, New York: John Wiley & Sons, 1981.
- [45] N. S. J. Pau, "Robust high throughput space-time block coded MIMO systems," *PhD Thesis*, University of Canterbury, 2007.
- [46] S. J. Grant and J. K. Cavers, "Multiuser channel estimation for detection of cochannel signals," *IEEE Trans. Commun.*, vol. 49, pp. 1845-1855, Oct. 2001.
- [47] W. C. Jakes, "Microwave Mobile Communications," *John Wiley*, New York, 1974.
- [48] E. W. Jang, J. Lee, H.-L. Lou and J. M. Cioffi, "Optimal combining schemes for MIMO systems with hybrid ARQ", in *Proc. ISIT*, pp. 2286-2290, Nice, France, Jun. 2007.
- [49] Y. Kim, T. Kim, C. Kang and D. Hong, "Union bound of maximum likelihood detection in downlink MIMO MC-CDMA systems," in *Proc. ICC*, vol. 6, 20-24 Jun. 2004.
- [50] X. Zhu and R. D. Murch, "Performance analysis of maximum likelihood detection in a MIMO antenna system," *IEEE Trans. Wireless Commun.*, vol. 50, pp. 187-191, Feb. 2002.
- [51] P. Kjellander and J. K. Cavers, "Corellated fading and antenna directionality in multiuser detection," in *Proc. VTC*, vol. 7, pp. 1909-1913, Sep. 2004.
- [52] P. Kjellander, "Multiuser detection and directional antennas," *Master of Science Thesis*, Royal Institute of Techn. (KTH), Stockholm, Sweden, Mar. 2004.
- [53] A. Goldsmith, "Wireless Communications," *Cambridge University Press*, 2005.

